UNIVERSITAT DE BARCELONA

New Fabrication Methodologies for the Development of Low Power Gas Sensors Based on Semiconducting Nanowires

Jordi Samà Monsonís

Aquesta tesi doctoral està subjecta a la llicència ***Reconeixement 3.0. Espanya de Creative Commons***.

Esta tesis doctoral está sujeta a la licencia ***Reconocimiento 3.0. España de Creative Commons***.

This doctoral thesis is licensed under the ***Creative Commons Attribution 3.0. Spain License***.

UNIVERSITAT DE BARCELONA

New Fabrication Methodologies for the Development of Low Power Gas Sensors Based on Semiconducting Nanowires

Jordi Samà Monsonís

Director de la Tesi:

Dr. Albert Romano Rodríguez

Programa de Doctorat en Nanociències

Departament d'Enginyeries: Secció Electrònica

Grup de Micro-Nanotecnologies i Nanoscòpies per

Dispositius Electrònics i Fotònics (MIND)

Institut de Nanociència i Nanotecnologia (IN^2UB)

Programa de Doctorat en Nanociència

New Fabrication Methodologies for the Development of Low Power Gas sensors based on Semiconducting Nanowires

Tesi que presenta Jordi Samà Monsonís

per optar al títol de Doctor per la Universitat de Barcelona

Director de la Tesi:

Albert Romano Rodríguez

Departament d'Enginyeria: Secció Electrònica

Grup de Micro-Nanotecnologies i Nanoscòpies per Dispositius

Electrònics i Fotònics (MIND)

Institut de Nanociència i Nanotecnologia (IN^{2}UB)

UNIVERSITAT DE BARCELONA

TABLE OF CONTENTS

1. INTRODUCTION 5
ABSTRACT 5
1.1. DEMAND OF GAS SENSORS 6
1.2. SOLID STATE GAS SENSORS 7
1.2.1. Semiconductor gas sensors 8
1.3. NANOSTRUCTURED MATERIALS 9
1.4. GAS-SOLID INTERACTION 12
1.4.1. Solid-gas interface 12
1.4.2. Statistical description of Langmuir isotherm 17
1.4.3. Chemiresistive sensors 21
1.5. OBJECTIVES 26
1.6. REFERENCES 27
2. FABRICATION AND CHARACTERIZATION TECHNIQUES 33
ABSTRACT 33
2.1. INTRODUCTION 34
2.2. SYNTHESIS OF NANOWIRES 35
2.2.1. Vapour-Liquid-Solid Mechanism 37
2.2.2.1 The role of metal nanoparticles 38
2.2.2.2 Details of VLS methods used in this thesis 40
2.3. FIBID AND FEBIP INSIDE A FIB-SEM DUAL BEAM 40
2.3.1. Electrical contact fabrication for the NWs 46
2.4. ELECTRON BEAM LITHOGRAPHY 48
2.4.1. Resist exposure: interactions and limitations 50
2.4.2. Contacting procedure for NWs 54
2.5. MICROMEMBRANES AND MICROHOTPLATES 55
2.6. ELECTRICAL AND GAS MEASUREMENTS 58
2.6.1. Electrical measurement setup 58
2.6.2.1 Macroscopic access to individual NWs 59
2.6.2. Gas measurement setup 60
2.7. REFERENCES 63
3. LOCALIZED GROWTH OF SNO_2 AND GE NWS 69

3.1. INTRODUCTION 70
3.2. EXPERIMENTAL DETAILS 72
3.2.1. Calibration of temperature versus heater power in vacuum conditions 72
3.2.2. Growth process 75
3.2.3. Experimental instrumentation 78
3.3. RESULTS AND DISCUSSION 78
3.3.1. Growth of SnO_2 nanowires 78
3.3.2. Growth of Ge nanowires 81
3.3.3. Raman spectroscopy characterization of SnO_2 NWs 83
3.4. CONCLUSIONS 87
3.5. REFERENCES 88

4. SITE-SELECTIVELY GROWN SNO_2 NWS NETWORKS FOR AMMONIA SENSING IN HUMID CONDITIONS 91

ABSTRACT 91
4.1. INTRODUCTION 92
4.2. EXPERIMENTAL SECTION 93
4.3. RESULTS AND DISCUSSION 93
4.3.1. Oxygen adsorption 93
4.3.2. Response to ammonia in dry synthetic air 96
4.3.3 SnO_2 NWs sensing mechanisms in humid conditions 101
4.3.3.1 SnO_2 NWs interaction towards H_2O 101
4.3.3.2 Ammonia sensing in humid conditions 104
4.3.4. Response towards other gases 107
4.3.4.1. Response towards CO 107
4.3.4.2. Response towards NO_2 108
4.4. SUMMARY OF THE DIFFERENT RESPONSES 109
4.4 CONCLUSIONS 111
4.5 REFERENCES 111

5. LOW TEMPERATURE SENSOR BASED ON GE NWS LOCALLY GROWN ON SUSPENDED MICROHOTPLATES 117

ABSTRACT 117
5.1. INTRODUCTION 118
5.2. EXPERIMENTAL DETAILS 119
5.3. RESULTS AND DISCUSSION 119
5.3.1. Structural characterization and conducting behaviour 119
5.3.2. Determination of the optimal sensing temperature 122
5.3.3. Response to oxidizing species 123
5.3.4. Response to reducing gases 126

5.3.5. Gas selectivity and sensing mechanisms *131*
5.4. CONCLUSIONS 132
5.5. REFERENCES 133

6. INDIVIDUAL SNO_2 NWS CONTACTED BY EBL 137

ABSTRACT 137
6.1 INTRODUCTION 138
6.2 EXPERIMENTAL DETAILS 140
6.2.1 Uniformity of PMMA coating on chips *140*
6.2.2 Optimization of the fabrication parameters *145*
6.3 RESULTS AND DISCUSSION 149
6.3.1 Electrical characterization *149*
6.3.2 Response towards NH_3 .... *152*
6.3.3 Response towards NO_2 .... *155*
6.4 CONCLUSIONS 156
6.5 REFERENCES 157

7. CONCLUSIONS AND FUTURE PERSPECTIVES 161

7.1. GENERAL CONCLUSIONS 162
7.1.1. On the fabrication process *162*
7.1.2. On the sensing performance *163*
7.2. FUTURE WORK 165

RESUM EN CATALÀ 167

INTRODUCCIÓ 168
Objectius de la tesi *169*
RESULTATS I DISCUSSIÓ 171
Creixement localitzat de nanofils de SnO_2 i Ge *171*
Creixement localitzat de nanofils de SnO_2 per sensat d'amoníac en aire humit *172*
Sensors de baixa temperatura basats en nanofils de Ge *172*
Nanofils individuals de SnO_2 contactats per litografia per feix d'electrons *174*
CONCLUSIONS 175
REFERÈNCIES 177

1. INTRODUCTION

Abstract

An introduction to the current measurement technology for the monitoring of gas sensors is explained in this chapter. A brief state of the art and the requirements that current gas sensors need to fulfil are explained, providing the framework at which this Doctoral Dissertation was developed. At the end of this chapter, the fundamentals of the sensing mechanisms of metal oxide sensors will be explained.

1.1. Demand of gas sensors

The air and environment quality is, nowadays, one of the main political concerns of the governmental institutions [1]. The presence of toxic gas species and pollutants is the first environmental cause of premature death in European Union [2], and 400000 premature deaths each year in Europe are estimated to be due to the effects of urban air pollution [3]. The poor air quality is a specific and challenging issue in large urbanized areas and industrial zones, where the road traffic and industry causes the main pollutant emissions. Furthermore, with rising population, which is expected to mainly grow in cities, the pressure on urban environments is increasing.

In this sense, European Commission adopted a directive in December of 2013 that determines the air quality objectives for the period up to 2030, with stricter allowed national emissions for six pollutants [4]. The main pollutants are particulate matter (PM), for which the health concerns are focused on particles of diameter below 10 µm, sulphur dioxide (SO_2), nitrogen oxides (NO_x), which covers NO and NO_2, ammonia (NH_3), volatile organic compounds (VOC) and ground-level ozone (O_3). The emission of the pollutants is induced mainly by industrial emissions and both maritime and road transport, the latter producing mainly NO_x and CO. Furthermore, nitrogen oxides and sulphur oxide are known to produce the acid rain [5].

The detection of toxic gases and pollutants is required in many different applications, either indoor, outdoor or in work places. As an example of outdoor applications, the short-response actions that public institutions implement against temporary pollution peaks are sustained on their detection by air quality monitoring networks. Real time detection is required, for instance, in parking garages, in order to activate the ventilation systems. Other applications are found in industrial facilities, where the leakage of flammable or hazardous gases, or processed chemical species can present a threat to safety and need to be detected immediately. These are just few examples of the necessity of monitoring and sensing the presence of gases in the day life. Therefore, suitable gas detection is nowadays an important requirement and the interest and applications are expected to grow since mobile phones are providing a portable platform that allows integrating sensors and identify harmful threads in personal environment. The necessity and requirements in the different fields of gas sensors may be described from an economical point of view: the global gas sensors

market was estimated to be $1780 million in 2013, with a compound annual growth rate of 5.1% from 2014 to 2020 [6].

1.2. Solid state gas sensors

A gas sensor is a device that detects the presence of a determined amount of a certain gas and that gives as output an electrical signal whose value depends on the specific concentration of the analyte. The principles on which the gas sensor is based can be chemical and/or physical. A chemical sensor is a device that transforms chemical information, ranging from the concentration of a specific sample component to total composition analysis, into an analytically useful signal [7]. This chemical information may originate from a chemical reaction of the analyte or from a physical property of the system investigated. A physical sensor is defined as a device that provides information about a physical property of a system. However, in some cases is not possible to decide whether the operational principle is based on chemical or physical process, for instance, when an adsorption process gives rise to the signal. This is the case of the majority of the currently suitable gas sensors, in which the chemical information of the surrounding gases is transformed in a process that is dependent on the physical properties of the gas: pressure and temperature.

The present thesis focuses on semiconductor gas sensors, which form part of the solid state gas sensors. The main applications of solid state resistive sensors are in safety, automotive, process control, household applications and environmental monitoring [8].

Solid electrolyte sensors have been introduced in the market more than one decade ago. This type of sensors are based on a material that allows the conduction of ions (electrolyte) but not of electrons, being both collected through different paths [9]. Yttria-stabilized zirconia (YSZ) is the most common material of electrochemical-based sensors, being widely employed as oxygen sensor for air-to-fuel inspection, also known as lambda sensor, in automobile exhaust systems. This type of sensor is also known as potentiometric sensor, since usually the potential difference between the electrodes at which the chemical reactions take place is measured. However, also amperometric, impedimetric or catalytic measurements have been employed to obtain the sensing signal [8].

Conducting polymer materials have been studied as gas sensors since the early 1980s [10]. Polypyrrole and polyaniline are the most common polymers, employed in conductometric and Field Effect Transistor (FET) sensors. Polymers can operate at room temperature, which represents a clear advantage when compared to other materials [11]. The sensing mechanism towards oxidizing gases takes places through the electron transfer from the aromatic rings of the polymer to the adsorbate [11]. However, the sensing mechanism against reducing gases is still not understood and the surface reactions between polymers and gas adsorbates still require a better understanding to achieve future commercial applications.

Catalytic sensors or pellistors, are used to detect explosive or flammable gases. The catalyst sensing part is heated up to a temperature that allows a rapid combustion of the gas. The sensor detects gas concentration changes through the variation in resistance of the heating element produced by the temperature increase due to the gas combustion. Typically pellistors are made of Pt embedded in a ceramic material and are used to detect methane, carbon monoxide or hydrogen. However, for inexpensive detection of flammable gases at lower concentrations, semiconductor gas sensors offer better capabilities.

1.2.1. Semiconductor gas sensors

The first semiconductor gas sensor was introduced by Taguchi in the 1960s decade based on ZnO films, a metal oxide (MOX) sensor [12]. Since then, the advances in the materials science and fabrication processes allowed to improve the sensitivity and reliability, while simultaneously reducing the productions costs [13]. MOX materials change their electrical resistance upon the exposure to different gases, proportionally to the amount of adsorbate [9].

Metal oxide semiconductors are the most common materials used as semiconducting gas sensors. They can be used with different type of operational mechanisms, like resistive, capacitive or optical based sensors, among others [14]. Conductometric sensors are the most common type for metal oxide sensors. Metal oxides have several advantages over other type of gas sensors, like the low fabrication cost and robustness of the fabricated sensor, and offer a high potential for applications where the use of analytical systems, such as gas chromatographs or optical detector is prohibitive due to

the high cost involved. On the other hand, the simplicity of the transduced chemical quantity, and the possibility of integration into Si technology, make the metal oxide one of the most promising technologies for future applications, especially due to their scalability and possibility of very low power operation.

In addition to metal oxide, other semiconductors are investigated for gas sensing applications. The most widely used semiconductor, Si, is a less common sensing material, which has been briefly studied as a gas sensor in porous form of an impedimetric or a resistive sensor [15,16]. On the other hand, the first gas sensor utilizing a field effect principle was based on Si technology for hydrogen detection [17].

Wide bandgap semiconductors, such as SiC, AlN or GaN, are also employed as FET devices towards hazardous gases at high temperatures [18]. Specifically, SiC plays an important role in this kind of devices due to the high chemical inertness and good thermal conductivity, which can be used in harsh environments [19].

On the other hand, carbon based materials are also used as chemiresistors in the low temperature regime in the form of films [20]. Recently, with the discovery of graphene, this material or its oxide form have generated interest for their gas sensing properties [21].

1.3. Nanostructured materials

The introduction of nanostructures as a new type of architectures with enhanced sensitivity and low response time represented a step forward in the gas sensing field. The first demonstration of enhancing the sensitivity by reducing the crystallite size of a metal oxide to the nanometer scale was demonstrated in 1991 by Yamazoe *et al.* [22]. In this nanostructured material, the reactions involving gas adsorbate take place at the surface of the material or at the grain boundaries, causing a change in the density of charge carriers. Since for the resistive measurements the volume of the material is contributing, the surface-to-volume ratio becomes extremely relevant and an increased sensitivity was expected for nanostructures, arising as promising candidates that exhibit many inspiring characteristics.

The first work demonstrating the gas sensing capabilities of a single one-dimensional structure arises in 2000 [23], where a single-walled carbon nanotube was

studied towards NH_3 and NO_2. Other carbon based nanostructures, such as nanofibers, have also shown their potential in detecting gas species [24,25]. On the other hand, single metal oxide nanowire-based gas sensors were demonstrated shortly after [26].

Since these works, nanowires, nanorods and nanotubes have generated enormous interest for detecting gas species with superior performance [27]. The synthesis methodologies of one-dimensional nanowires have pursued the control over the shape, aspect-ratio, the crystallinity and surface properties of the grown structures, which enhanced the fabrication of improved gas sensors, and promoted the discovery of new synthesis routes.

In general, two different configurations on functional resistive sensors using nanowires as sensing part are found: multiple or single nanowire-based sensors. Multiple nanowires offer the enhanced response time of one-dimensional nanostructures together with the improved sensitivity due to the large surface-to-volume ratio of the devices. The electron conduction take place through the nanowires in this configuration, being modulated by the conductive diameter and the nanowire-to-nanowire contacts. On the other hand, individual nanowires offer other advantages, since the electronic transport takes place in one dimension without the barrier effects between grains or nanowire contacts, which allows to study the sensing mechanisms on a system with a well-defined geometry that facilitates the study of basic interactions. Furthermore, the gas diffusion takes place in an even easier way than in a bundle of NWs, which leads to a reduction of the response time. Nevertheless, the fabrication process is, obviously, more time-consuming for single nanowire-based devices. Furthermore, the absence of a redundancy of the conduction paths makes the single nanowire-based devices less robust than their multiple nanowire counterpart.

Despite the research efforts to study theoretically and experimentally metal oxide sensors, there is still an important lack of basic understanding on sensing mechanisms of metal oxide nanowire sensors [18]. Further investigation are required in order to ensure reliability and reproducibility in the fabrication of gas sensors based on nanowires. Moreover, the research is focused on different requirements of metal oxide, which are also valid for gas sensors.

The selectivity towards a specific gas is one of the main challenges of metal oxide gas sensors, as sensitivity is relatively good for the devices. Several alternatives are

found to improve the selectivity. On one hand, surface modification by self-assembled monolayers (SAM) has been proven successfully towards NO_2 by adding amines [28] or metal nanocomposites in order to improve the selectivity [29]. In addition to the routes to functionalize the material's surfaces, which are being studied for more than 20 years with a modest result, electronic noses, which comprehend a set of multiple sensors, each of them with specific and different sensitivities to the gases of interest, have emerged as an efficient alternative to improve selectivity and to analyse complex gas mixtures with relatively unselective sensor [30]. This increase is promoted by the very low cost of electronic components, circuits and boards, that, combined with the reduced price of the sensors, gives rise to a relatively cheap sensing system.

Low power consumption of gas sensors is mandatory for a sustainable technology, and completely necessary for the development of autonomous devices with long term operational capabilities. Surface or bulk micromachining allows to fabricate micro-electromechanical systems (MEMS), that have been demonstrated as a successful approach in order to miniaturize and reduce the power consumption of the metal oxide gas sensors, for which the devices employ embedded microheaters [31].

On the other hand, previously non-explored semiconducting materials may offer new opportunities for gas sensing. A part of the present work, in this sense, deals with a quite known semiconductor as Ge, which has been briefly analyzed as a gas sensor, and tries to elucidate the behavior and the conditions that provide a sensing behavior that has not been previously reported before.

Furthermore, one of the main challenges for the introduction of nanowires in the commercial market resides in the integration of one dimensional nanostructures with the controlling electronics, which should further reduce the fabrication costs and the spread of this devices [18]. The fabrication methodology of nanowires usually involves different stages, like the growth of nanowires and their removal from the substrate where they were grown. The NWs are then transferred to the electronic platform and, in some cases; final electrical contacts have to additionally be fabricated. On the other hand, the NWs can be dispersed over substrates with pre-patterned electrodes that do not require any further contact procedure.

Consequently, the exploitation of nanowires with gas sensing purpose involves (sometimes highly) time-consuming processes with multiple and complex steps. This

important issue has been partially overcome in the work presented in this thesis, providing a simplified approach by eliminating several steps of the process without reducing the performance of the fabricated devices.

1.4. Gas-solid interaction

This section describes the basics of the physical and chemical processes that take place at the surface of a solid state gas sensor, and more concretely, of a metal oxide that leads to the gas sensing. These processes will be used in order to describe and justify, in the subsequent chapters, the mechanisms taking place at the fabricated and experimentally studied gas sensors based on nanowires.

The first part of this section presents the different types of gas adsorption processes taking place at the surface of a material and the involved interaction. Moving to a higher scale, a description of the surface coverage given by Langmuir isotherm is presented in terms of the thermodynamic properties of the gas adsorbate. Finally, the specific events that lead to the observation of a change in the resistance of a metal oxide, used as a chemiresistive sensor, are given in the last section.

1.4.1. Solid-gas interface

A basic step of the gas sensing mechanism and of any catalytic reaction is the adsorption process. Adsorption is an increase in the concentration of a dissolved substance at the interface of a condensed and a gaseous phases due to the effect of surface forces [7]. Our interest is focused on the sticking of gas molecules (adsorbate) at a solid surface (adsorbent).

In order to give a first description, we can describe the flux of molecules impinging a surface (ϕ_i), by the Hertz-Knudsen equation [32]:

$$\phi_i = \frac{p}{(2\pi m k_B T)^{\frac{1}{2}}} \tag{1.1}$$

where p denotes the pressure, m the mass of the molecule, k_B the Boltzmann constant and T the temperature. The molecules striking the surface may stay on the surface (adsorption) depending on several factors (temperature, binding energy with the surface, among other) and afterwards, they can be desorbed. A gas sensor requires

adsorbing and desorbing of the gas species in order to interact with the adsorbate and to recover the initial state, respectively.

All the gases tend to be adsorbed at the solid surface as a result of van der Waals interactions. This case is known as *physisorption* or *physical adsorption*, where the interaction takes place without involving charge transfer between the adsorbent (solid) and adsorbate (gas). The process is reversible, non-activated and non-dissociative, i.e., the gas specie remains unmodified, and takes place usually at temperatures close to the boiling point. At higher temperatures the physisorption can be neglected. Physical adsorption involves permanent dipole, induced dipole and quadrupole attraction between a molecule and a solid surface [33].

In more detail, physisorption is described as a binding of an atom or molecule to a solid surface consisting in the addition of the polarization potential and the Pauli repulsion of the electrons [34,35]:

$$V_{phys}(z) = V_{pol}(z) + Kn(r) \quad (1.2)$$

where $V_{pol}(z)$ is the long-range attractive polarization potential described as

$$V_{pol}(z) = -\frac{C_3}{z^3} - \frac{C_4}{z^4} - \frac{C_5}{z^5} - \cdots \quad (1.3)$$

and $Kn(r)$ is the repulsive force from Pauli repulsion at short distances, arising from the overlap of the electronic clouds of the adsorbate and the surface, and z stands for the distance from the surface.

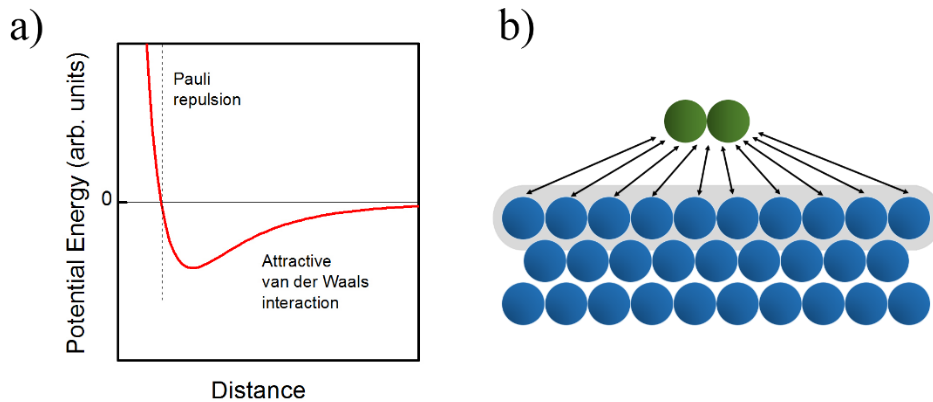

Figure 1.1. a) Physisorption potential energy between a particle and the surface of a solid represented as a function of the distance to the surface, which follows a Lennard-Jones potential; b) Diagram of Van der Waals interaction between the surface and molecule. Physisorption takes place with all gas adsorbate, i.e., is non-specific, and the forces are non-localized on concrete sites; the whole surface interacts with the gas molecules.

Lennard-Jones proposed a simple model to describe the combination of both interactions, the attractive and repulsive forces by a unique potential [36]. The potential is given by:

$$V_{phys}(r) = 4\varepsilon\left[\left(\frac{\sigma}{r}\right)^{12} - \left(\frac{\sigma}{r}\right)^{6}\right] \quad (1.4)$$

where ε is the depth of the potential well and σ is the distance at which the potential is zero. The attractive term has the inverse six-power term, and the repulsive one corresponds to the inverse twelve-power term. The potential is represented in Figure 1.1 a). Van der Waals forces induce a long-range interaction, which attracts the gas molecule in order to minimize its energy, typically up to an optimal adsorption distance of r>3 Å. The interaction involves a small adsorption energy, of less than few hundreds of meV [37]. Due to the low binding energy, the physisorbed particles are strongly mobile on the surface and are easily desorbed. In principle, it is supposed that the surface of the solid follows an unspecific interaction with the adsorbate, i.e., the interaction takes places on all surface sites with the molecule independently of the gas specie, attracting the molecule as long as the proper pressure and temperature conditions are kept [38], as shown in Figure 1.1 b). However, some molecules may only physisorbed to specific surface sites as a function of the polarity of the latter ones.

Another interaction regime takes place for higher adsorption energies, comparable to the energy of a chemical bond, where electrons are shared between the gas adsorbate and the surface of the solid, which gives rise to *chemisorption* or *chemical adsorption*. In this case, the adsorbate tends to be localized in specific sites, although some diffusion might occur in the process [38].

Chemisorption involves thus, the rearrangement of the electrons from the gas and of the solid, with the subsequent formation and breaking of chemical bonds. Furthermore, chemisorption has no restrictions on temperature, unlike physisorption, although the effectiveness of the chemisorption may be limited to a specific temperature range. At low temperatures, chemisorption may be slow and, therefore, the mechanism barely takes place, leading to the observation that the main adsorption phenomenon is physisorption. The energy of the interaction in the chemisorption of adsorbates can reach several eV, one order of magnitude above the typical values for physisorption.

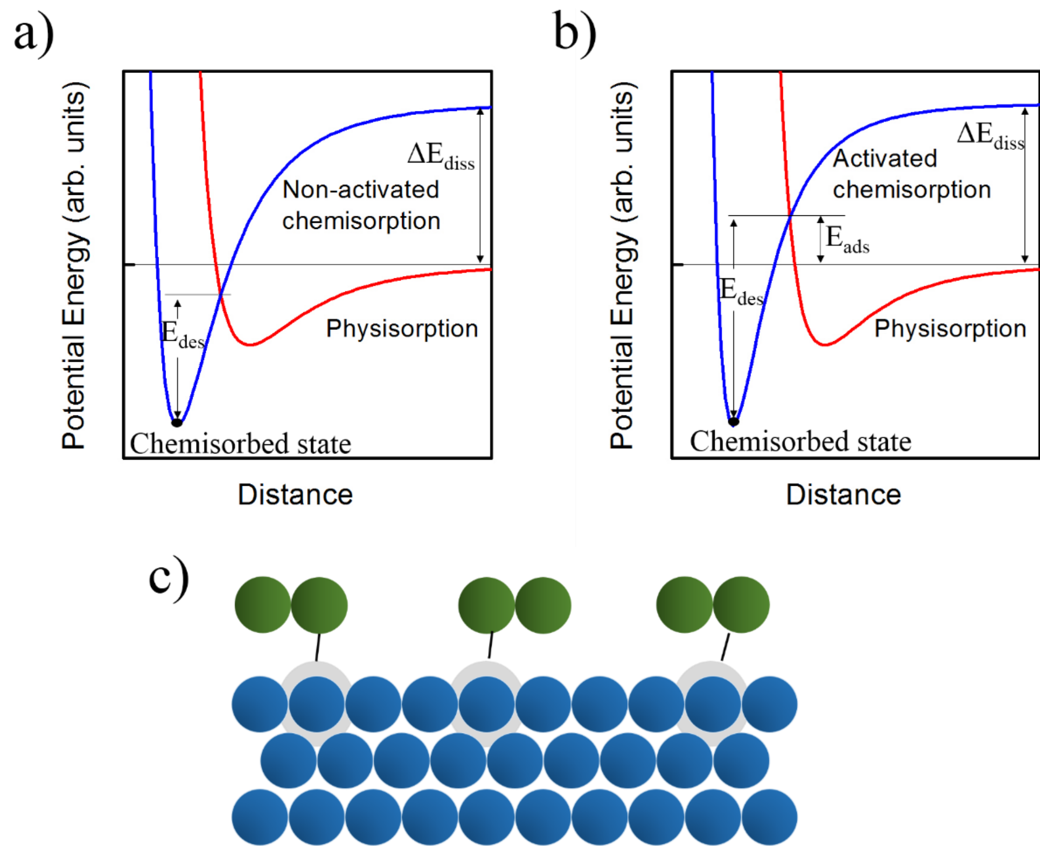

Figure 1.2 Potential energy during a a) non-activated chemisorption and b) activated chemisorption processes. The activated chemisorption requires additional energy in order to pass from physisorbed stated to the chemisorbed state; c) Diagram of chemisorbed molecules denoting the localization of the interaction on adsorption sites.

Other differences found between the two processes is that chemisorption is often dissociative, may be irreversible and can be localized at a specific site, as is shown in Figure 1.2 c). There is no abrupt change in pressure nor in temperature that separates the two adsorption regimes, but the adsorption regime in the extremes of these magnitudes are easy to distinguish.

The potential energy of chemisorption may be represented as a Lennard-Jones potential, Morse potential, or Buckingham potential, among others [33]. The Lennard-Jones potential in chemisorption process is represented in Figure 1.2 a) and b) as a function of the distance from the surface for non-activated and activated processes, respectively.

The gas molecule approaching the surface from a certain distance experiences the Van der Waals interaction, being initially bound to the surface at the physisorbed state. As the molecule further approaches the surface, it may also suffer the chemisorption potential. When the intersection between physisorption and chemisorption energy

potentials is found at negative energy values, the process is said non-activated and no activation energy must be overcome to reach the chemisorbed state (Figure 1.2 a). On the other hand, when the intersection occurs at positive energies, if the molecule has enough energy, it can overcome this barrier and will prefer to follow the chemisorption potential curve to reach the lower energy state (Figure 1.2 b). The equilibrium distance for chemisorption is usually found between 1 and 3 Å [33].

In a dissociative process, the activation energy may represent, for instance, the energy necessary for the dissociation of the molecule. Furthermore, desorption is also a process with an energy barrier E_{des} due to the fact that breaking the bond is necessary in order to escape from the potential well. This applies to both non-activated and activated processes (see Figure 1.2 a) and b)). Therefore, one can expect a temperature dependence of the processes to be Arrhenius-like [39]:

$$k_p = Ae^{-E_p/k_bT} \tag{1.5}$$

where k_p stands for the reaction rate constant, A is the pre-exponential factor, and E_p the activation energy of the process, that one may expect to be E_{ads} and E_{des} for adsorption and desorption processes, respectively. Once physisorption and chemisorption have been introduced, it is useful to describe the events that leads to the chemisorption of an impinging gas on a solid surface. Assuming a clean surface, the events that may happen as a result of the collision of the molecule are:

Table 1.1. Comparison of the main properties of physisorption and chemisorption

Physisorption	Chemisorption
Weak and long range bonding	Strong, short range bonding
Polarization	Electron exchange
Non-surface specific	Surface specific
No surface reactions	Surface reactions: dissociation, catalysis..

i) The gas molecule is scattered by the surface in an elastic process, without any loss of energy.

ii) The molecule loses some energy (translational energy, for instance), transferring it to the solid and reaching the physical adsorbed state, i.e., finally remaining in the minimum of the physisorption potential.

iii) The molecule passes, if the energy is high enough, directly to a chemisorbed state if this can be formed near the incidence site, without being trapped in the physically adsorbed state.

iv) The molecule may be physisorbed at the site of the incidence and then it may a) be chemisorbed, b) be inelastically scattered back to the gas phase or c) hop to a neighbouring site, where again, cases i) and ii) can take place again.

v) During the formation of the chemically adsorbed species, the molecule or its dissociated parts may a) lose chemical energy, released to the solid, and become localized at the original site or b) lose energy and hope diffusively until the excess of energy is dissipated.

Chemiresistive sensors are generally based on the chemisorption of the molecules. As explained, chemisorption requires higher energy of the molecule than the physisorption process. For this reason, the sensing material needs to be heated up, since chemisorption usually takes place at temperatures above 150 °C. The exposed properties of chemisorption and physisorption are compared in Table 1.1.

1.4.2. Statistical description of Langmuir isotherm

The adsorption of a monoatomic gas on a solid surface at constant temperature is a situation that may be approximated by different models, like Langmuir isotherm, based on the adsorption of a monolayer, or Brunauer, Emmett and Teller (BET) isotherm, which is used to describe the adsorption of several monolayers, among others. A statistical treatment of the Langmuir isotherm will be presented, which describes the equilibrium state of the adsorption, but do not provide information about the dynamics of the system.

The adsorption isotherm reveals information about the amount of adsorbate that is adsorbed given a set of state variables: pressure p and temperature T. Several magnitudes must be considered in order to develop the statistical description. Let us

consider N_o as the number of localized sites at which the gas, considered as being monoatomic, may adsorb, and N_{ads} as the number of adsorbates at the surface of the solid. The amount of adsorbed material is given in terms of surface coverage θ, which is the ratio of occupied sites related to the total available sites.

It is assumed that one specie of adsorbate, and at most one adsorbate, may be bound at each adsorption site. This implies that just, at the limit, when full coverage occurs, one monolayer of particles may be adsorbed. Additionally, it is considered that one adsorbate does not interact with the others, i.e., the binding energy is independent of the coverage. Thus, the binding energy ε of the atom is considered to be independent of the number of adsorbed atoms [38]. All this situation supposes that the temperature in the system is kept constant.

The energy of the system with N_{ads} adsorbed particles is, hence, $N_{ads}\ \varepsilon$, and the number of configurations that have this energy is the binomial coefficient $C_{N_o}^{N_{ads}}$. The canonical partition function is:

$$Q_{ads} = C_{N_o}^{N_{ads}} \exp\left(\frac{N_{ads}\varepsilon}{\mathrm{k_B}T}\right) \quad (1.6)$$

where k_B is the Boltzmann constant and T the temperature. The grand canonical partition function is described as:

$$\Theta = \sum_{N_{ads}}^{N_o} Q_{ads} \exp\left(\frac{N_{ads}\,\mu_{ads}}{\mathrm{k_B}T}\right) \quad (1.7)$$

where μ_{ads} is the chemical potential of the adsorbate. Introducing (1.6) into (1.7), we obtain:

$$\Theta = \left(1 + \exp\left(\frac{\varepsilon + \mu_{ads}}{\mathrm{k_B}T}\right)\right)^{N_o} \quad (1.8)$$

Thus, the probability that N_{ads} atoms are adsorbed at the surface of a solid, is given by:

$$P(N_{ads}) = \frac{Q_{ads}\exp\left(\frac{N_{ads}\mu_{ads}}{k_BT}\right)}{\Theta} \quad (1.9)$$

Consequently, the average number of adsorbed particles is:

$$\langle N_{ads}\rangle = \sum_{N_{ads}}^{N_o} N_{ads}P(N_{ads}) = k_BT\frac{\partial}{\partial\mu_{ads}}\ln(\Theta) \quad (1.10)$$

The surface coverage θ is the fractional part of the surface that is occupied by adsorbate. As a consequence, one can deduce that:

$$\theta = \frac{\langle N_{ads}\rangle}{N_o} = \frac{\exp\left(\frac{\varepsilon+\mu_{ads}}{k_B T}\right)}{1+\exp\left(\frac{\varepsilon+\mu_{ads}}{k_B T}\right)} \quad (1.11)$$

At equilibrium, the chemical potential of all phases must be equal and. thus, μ_{ads} can be calculated as the chemical potential of monoatomic ideal gas, according to:

$$\mu_{ads} = k_B T \ln\left[\frac{p}{k_b T}\left(\frac{h^2}{2\pi m k_B T}\right)^{\frac{3}{2}}\right] \quad (1.12)$$

where p is the equilibrium pressure of the gas, m the mass of the atom and h the Planck constant. Substituting (1.12) into (1.11) gives:

$$\theta = \frac{p}{p+p_o(T)} \quad (1.13)$$

being:

$$p_o(T) = \left(\frac{2\pi m k_B T}{h^2}\right)^{\frac{3}{2}} k_B T \exp\left(-\frac{\varepsilon}{k_B T}\right) \quad (1.14)$$

The so-called Langmuir adsorption corresponds to the equation (1.13). This relation shows that at low pressures, the partial coverage is proportional to p, and at high pressures θ tends asymptotically to 1. Furthermore, $p_o(T)$ may be understood as the pressure required to obtain an equilibrium coverage of θ=0.5 at a certain temperature T. From (1.14) it is inferred that for high binding energy ε, p_o decreases exponentially and thus, the coverage tends to 1 at low pressures. Thus, the coverage is determined, besides the state variables, by the binding energy.

The adsorption and desorption rates ($d\theta/dt$) of the adsorbate are related to the coverage. Here we will assume, as an extension of the Langmuir isotherm, that the molecules can follow a dissociative adsorption, which breaks the molecule into n fragments (n=1 for non-dissociative adsorption). Therefore, the adsorption and desorption rates are described as follows:

$$\frac{d\theta}{dt} = k_{ads} p[N_o(1-\theta)]^n \quad \text{(Adsorption)} \quad (1.15)$$

$$\frac{d\theta}{dt} = k_{des}(N_o\theta)^n \quad \text{(Desorption)} \quad (1.16)$$

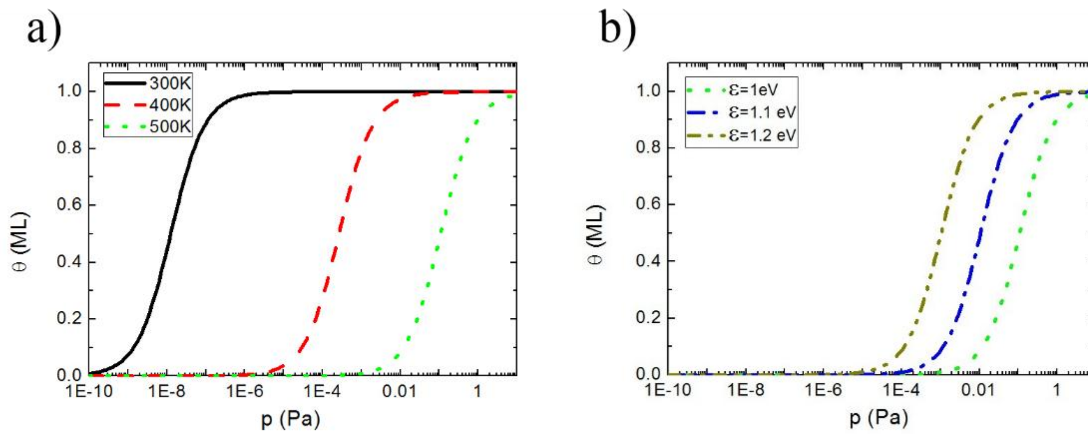

Figure 1.3 Langmuir isotherms as a function of the gas pressure, calculated for an atom of hydrogen: a) showing the dependence on temperature for a physisorbed process. The binding energy is assumed to be 1 eV; b) exhibiting the changes for increasing ε. The coverage is calculated at 500K.

Where k_{ads} and k_{des} are the temperature-dependent constants of adsorption and desorption, respectively. At the steady state, the adsorption and desorption rates are both equal to 0. From these considerations, and equalizing thus both equations, the expression for Langmuir isotherm is obtained, in terms of a dissociative adsorption from another treatment.

The dependence of the coverage on the gas pressure is represented in Figure 1.3 a) for different temperatures, assuming ε=1eV. The different coverages of the same system, obtained at 500K, and changing the binding energy are shown on Figure 1.3 b). The isotherms have been obtained assuming that a hydrogen atom is adsorbed at a certain pressure.

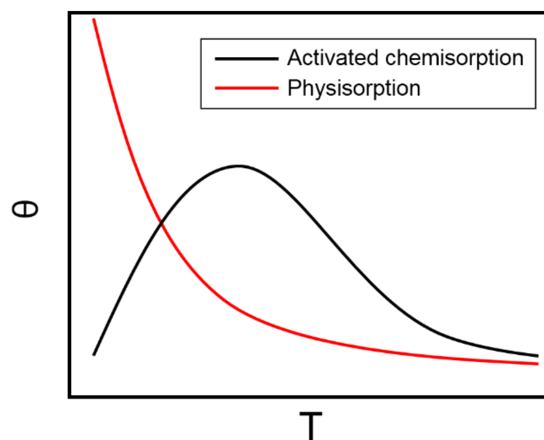

Figure 1.4. Temperature dependence of coverage at isobaric conditions for physisorption and activated chemisorption processes.

The figures indicate a decreasing coverage for increasing temperatures and decreasing ε, at a constant pressure, which is valid for physisorption. The figures show, additionally, that any variation of the binding energy and temperature leads to an important change of the coverage because of the existence of the exponential dependence.

At isobaric conditions, and looking at the temperature dependence of the coverage, activated chemisorption and physisorption processes show different behaviors (see Figure 1.4). The coverage diminishes as the temperature increases, for the physisorption isobar, in which since the adsorption should decrease with rise in temperature, according with Le-Chatelier's principle. Nevertheless, in the case of an activated chemisorption, the coverage increases initially with rising in temperature due to the presence of an energy barrier.

Langmuir isotherm equation is not expected to be valid in all cases, because the binding energy or the heat of adsorption often decrease with increasing surface coverage. Hence, the treatment is only valid for low surface coverages, since the binding energy is considered constant in these conditions. Furthermore, in the model a perfect surface without surface diffusion is assumed. More realistic calculations of isotherms can be performed using Monte-Carlo techniques [40]. However, Langmuir isotherm is a useful model to introduce the solid-gas interaction and to analyse to a first approximation how the adsorption of a gas is affected by the thermodynamic state variables.

It must be noted, that the approach here presented assumes a unique adsorbate in the gas phase, although in general more than one gas specie interacts with the surface and competition among them exist to be chemisorbed at specific adsorption sites.

1.4.3. Chemiresistive sensors

Once the different types of adsorption of a gas on a solid surface have been discussed and the parameters that influences the coverage of a solid surface have been described, the mechanisms that give rise to the sensitivity to the resistive gas sensors will be presented, with a special focus on semiconducting metal oxides.

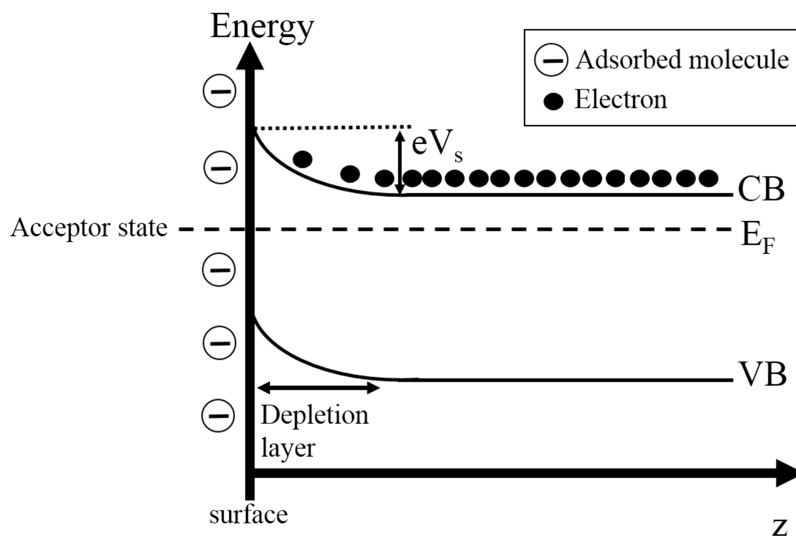

Figure 1.5. Energy band diagram at the surface of an n-type metal oxide semiconductor, where an adsorbate on the surface creates an acceptor level, which produces an upward band bending.

The first step in the sensing mechanism of metal oxide is based on the physisorption or the chemisorption of the gas on adsorption sites of the metal oxide surface [9,41,42]. The metal oxide materials employed for gas sensing purposes are considered and treated as wide bandgap semiconductors, as for instance, ZnO or SnO_2, whose energy bandgap is in the range of 3.6 eV.

This section will consider the chemisorption of the gas molecules, which produces a charge transfer with the solid. When a molecule is adsorbed at its surface, electrons are donated to this molecule if the lowest unoccupied molecular orbital of the molecule is found below the Fermi level of the solid (acceptor levels) [9]. At the same time, electrons are transferred to the solid if the highest occupied orbital from the adsorbate is above the Fermi level of the solid (donor levels). Therefore, a net charge will be fixed at the surface of the solid, giving rise to an electric field, which causes a subsequent band bending of the energy bands of the material.

The adsorption of a molecule that gives rise to a *surface acceptor state*, i.e., an electron from the semiconductor is donated to the electron, causes the accumulation of negative charge, situation represented in Figure 1.5, which induces the upward bending of band diagram at the surface. If an n-type semiconducting material is assumed, as shown in the diagram, whose Fermi level is within the bandgap but close to the conduction band, the band bending at the surface gives rise to a reduction of the majority charge carriers density (electrons) at the surface and thus, produces a depletion

layer in this area. The depletion layer is characterized by a positive charge that compensates the negative surface charge.

The charge density in the depletion zone can be determined by solving Poisson's equation. Here we assume a one dimensional problem, following:

$$\rho = e[p(z) - n(z) + D^{+}(z) - A^{-}(z)] = \varepsilon_r \varepsilon_0 \frac{d^2V}{d^2z} \quad (1.17)$$

where e is the elementary charge, p and n denote the hole and electrons densities, respectively, and D^+ and A^- are the density of ionized donors and acceptors. ε_r and ε_0 are the dielectric constant of the material and vacuum.

For simplicity, it is assumed that the semiconductor is n-type and, therefore, the acceptor and hole concentrations are negligible in front of the electron density. Besides, the donor species in the semiconductors bulk are considered to be all ionized, i.e., $D^+(z)=D^+=n_b$, which are, at the same time, equal to the bulk electron density. Thus, we rewrite equation 1.17 as:

$$e[-n(z) + D^{+}] = \varepsilon_r \varepsilon_0 \frac{d^2V}{d^2z} \quad (1.18)$$

To analytically solve the previous equation, a discontinuous abrupt transition of the electron density is considered, being $n(z)=D^+=n_b$ in the bulk and $n(z)=0$ in the space charge region, whereby the space charge region is delimited by the Debye length (λ_D). Therefore, the electric field ($E=dV/dz$) may be obtained integrating (1.18):

$$E(z) = \frac{e n_b (z - \lambda_D)}{\varepsilon_r \varepsilon_0} \quad (1.19)$$

The potential is obtained integrating the electric field as function of z:

$$V(z) = \frac{e n_b (z - \lambda_D)^2}{2 \varepsilon_r \varepsilon_0} \quad (1.20)$$

Imposing charge neutrality conditions of the whole system allows to deduce that the space charge must be equal to the surface charge:

$$n_b \lambda_D = N_s = \theta [S_t] \quad (1.21)$$

where N_s denotes the number of the surface charges per unit area, θ being the coverage, already presented in the previous section, and $[S_t]$ is the density of adsorption sites in the surface, occupied and unoccupied. We may define the potential to be 0 in the bulk: $V(z> \lambda_D)=0$, and thus, using (1.21) the surface potential is obtained as follows:

$$V_s = \frac{en_b{\lambda_D}^2}{2\varepsilon_r\varepsilon_0} = \frac{eN_s^2}{2\varepsilon_r\varepsilon_0 D^+} \tag{1.22}$$

Consequently, the change in charge carrier density at the depletion layer due to the surface charges, described by N_s, gives rise to a variation of the conductivity of the semiconductor, which causes a resistance change that can be measured in the gas sensing devices, described by:

$$\Delta\sigma = e\left[\mu_n \int n(z) - n_{bulk} dz + \mu_p \int p(z) - p_{bulk} dz\right] \tag{1.23}$$

where μ_n and μ_p denotes the electron and hole mobility. Therefore, even though the surface conductivity is the only parameter which is altered in the semiconductor by the gas adsorption, the experimental measurements of the resistance of the sensor contains both the surface and bulk conductivities, the former depending on the thickness of the depletion layer. From this result, it is evident that the surface-to-volume ratio of the adsorbent becomes an important parameter.

The geometry of the sensing part, thus, acquires special relevance, since, theoretically, for thickness below the depth of the space charge region full depletion of the material is reached, which is expected to enhance the change in conductivity and, consequently, the response of the sensor. Additionally, the crystalline quality of the material must be taken into account.

In a polycrystalline material not only the surface is exposed to the adsorbate, but also the grain boundaries, which are also depleted of carriers at their surfaces due to the grain-grain barriers. In the case of a polycrystalline material, its surface increases compared to a monocrystalline material, and the multiple space charge regions between the individual grains strongly contribute to the change in the total resistance of the material by amplifying the effect of the presence of chemisorbed gas molecules, because the Schottky barriers that are formed between the grain, according to the previous reasoning (see Figure 1.6).

The gas diffusion through the grain boundaries, however, requires longer times than the diffusion at the surface of the semiconductor and, thus, would give rise to a longer response time. Schottky contacts may be found, also, at the junction of semiconducting materials and metal electrodes, whose associated height barriers may be altered due to the adsorption of gases, modifying consequently the resistance measured on the operative gas sensor device.

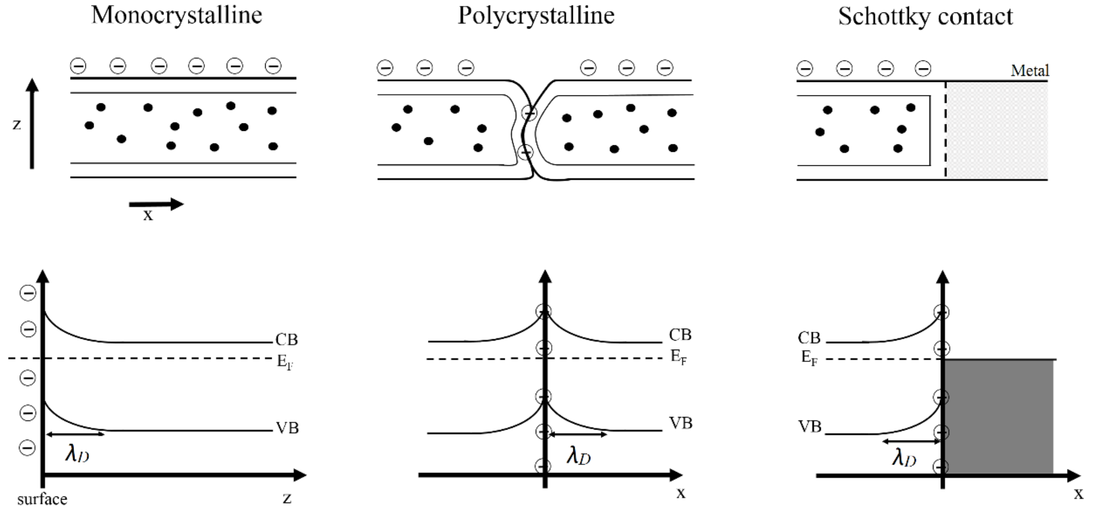

Figure 1.6. Energy band diagrams of three different scenarios where the adsorption of gas leads to band bending, affecting the conductivity of the semiconductor material: monocrystalline material, polycrystalline material, which is represented by a grain boundary, and a Schottky contact, formed by the junction of a metal and a semiconductor.

Note that, for an n-type semiconductor, the upward band bending caused by the presence of negative charges (oxidizing species) at the surface reduces the density of charge carriers (electrons) and thus, reduces the conduction of the semiconductor. This is exemplified by the chemisorption of molecular oxygen (O_2) in SnO_2:

$$O_{2(g)} + e^- + S \leftrightharpoons O^-_{2(s)} \tag{1.24}$$

where S is an unoccupied chemisorption site for oxygen, e^- a free electron from the semiconductor, and O_2^- a chemisorbed oxygen. The terms *(g)* and *(s)* denote the form in which the adsorbate is found, namely as gas in the surrounding atmosphere or chemisorbed at the surface. This equation describes the first step of the sensing mechanism, which is followed by the band bending in the semiconductor.

In this latter situation, the removal of negative charges at the surface reduces the upward band bending, which leads to an increase in the majority charge carrier density and thus, the conduction increases. This process occurs during the adsorption of reducing gas species heated at the appropriate operating temperature. As an example, CO, reacts with oxygen according to:

$$2CO_{(g)} + O^-_{2(s)} \rightarrow 2CO_{2(g)} + e^- + S \tag{1.25}$$

From this explanation one concludes that, for an n-type semiconductor, reducing species lead to the increase of the conduction (decrease of the resistance) in the semiconductor , as illustrated by the incorporation of a free electron in the solid.

The opposite behaviour is found when an oxidizing specie is adsorbed on a p-type semiconductor surface. The adsorption of negative charges also shifts upwards the energy bands at the surface compared to the situation before the adsorption. Consequently, a more conductive layer is located at the surface. In a similar approach, reducing species induce the diminishment of the conductivity of the semiconductor, due to the reaction with pre-adsorbed oxygen.

1.5. Objectives

The main objective of this dissertation is to contribute towards the improvement of gas sensors based on semiconducting nanowires. The easy integration of nanowires in low consumption devices is the fundamental idea that guides this dissertation, and the subsequent characterization of the sensors. Furthermore, the low power consumption of the device is a constant condition of the presented procedures, implemented by means of MEMS substrate that has been used as platform for all the fabricated sensors.

The main objectives for the innovation and optimization of fabrication methodology are summarized in the following strategy:

1. Easy integration of nanowire-based devices by using localized growth on top of sensing platforms.

The site-specific growth of SnO_2 and Ge nanowires is performed on top of micromembranes and microhotplates, which are the sensing area of the gas sensors. The fabrication procedure allows in single process the growth of NW networks on top of the electronic platforms that will be used for the gas sensing, an important step forward towards the integration of nanowires on electronic devices.

The details of the procedure and the structural characterization of the grown nanostructures are detailed in the chapter 3 of this dissertation.

2. Characterization of the fabricated sensors

On the other hand, the fabricated devices can be used as gas sensors readily after the growth. The gas sensing behaviour of SnO_2 networks have been characterized towards different gases; specifically, the kinetics of ammonia response in dry and humid air has been analysed in detail. In addition, the influence of water vapour is analysed, and thus, the chemical paths of the interaction with ammonia have been related to the operating temperature. The study related to the gas sensing properties of network of tin dioxide nanowires is explained in chapter 4.

Furthermore, the synthesized meshes of Ge NWs have been for the first time, at the best of our knowledge, studied as a gas sensor. The chemical interactions towards oxidizing and reducing gases are analysed, paying important attention on the structural characterization, which results primordial for the analysis of sensing behaviour. Additionally, a sensing mechanism is proposed concerning the different experimental results obtained. The study of Ge NWs as a gas sensor is described in chapter 5.

3. New fabrication route towards single nanowire based gas sensors.

A procedure based on electron beam lithography is explored in order to fabricate individual nanowire-based devices on top of microhotplates and micromembranes. The experimental procedure for that is detailed in the different steps. The study of the substrate utilized is highlighted as an important step, which leads to the successful fabrication of the devices.

The individual nanowires have also studied as a gas sensor, whose results are discussed and compared to their mesh counterpart. The experimental observations and discussion of the single nanowire-based devices are explained in chapter 6 of this thesis.

1.6. References

[1] N. Yamazoe, Toward innovations of gas sensor technology, Sensors Actuators, B Chem. 108 (2005) 2–14. doi:10.1016/j.snb.2004.12.075.

[2] M.A. Danzon, R. Van Leeuwen, M. Krzyzanowski, Air Quality Guidelines for Europe, World Health Organization, 2nd ed., Copenhagen, 2000.

[3] Cleaner air for all, European comission for the Environment, (n.d.). http://ec.europa.eu/environment/pubs/pdf/factsheets/air/.

[4] Directive 2001/81/EC, European Parliament and the Council on National Emission Celings for certain pollutants, 2001. http://ec.europa.eu/environment/air/pollutants/ceilings.htm.

[5] World Health Organization, WHO Air quality guidelines for particulate matter, ozone, nitrogen dioxide and sulfur dioxide: global update 2005: summary of risk assessment, Geneva World Heal. Organ. (2006) 1–22. http://whqlibdoc.who.int/hq/2006/WHO_SDE_PHE_OEH_06.02_eng.pdf?ua=1.

[6] Gas sensors market by product, by technology, by end-use and by segment forecasts to 2020. Grand View research, 2014.

[7] IUPAC Compendium of Chemical Terminology (Gold Book), 2014. doi:doi:10.1351/goldbook.A00155.

[8] R. Moos, K. Sahner, M. Fleischer, U. Guth, N. Barsan, U. Weimar, Solid State Gas Sensor Research in Germany – a Status Report, Sensors. 9 (2009) 4323. doi:10.3390/s90604323.

[9] P.T. Moseley, Solid state gas sensors, Meas. Sci. Technol. 8 (1997) 223–237. http://stacks.iop.org/0957-0233/8/i=3/a=003.

[10] C. Nylabder, M. Armgrath, I. Kundstrom, An ammonia detector based on a conducting polymer, in: Proc. Int. Meet. Chem. Sensors, 1983: pp. 203–207.

[11] H. Bai, G. Shi, Gas Sensors Based on Conducting Polymers, Sensors (Basel). 7 (2007) 267–307. http://www.ncbi.nlm.nih.gov/pmc/articles/PMC3756721/.

[12] N. Taguchi, Patent, 45–38200, 1962.

[13] G.F. Fine, L.M. Cavanagh, A. Afonja, R. Binions, Metal Oxide Semi-Conductor Gas Sensors in Environmental Monitoring, Sensors. 10 (2010) 5469. doi:10.3390/s100605469.

[14] G. Korotcenkov, Metal oxides for solid-state gas sensors: What determines our choice?, Mater. Sci. Eng. B. 139 (2007) 1–23. doi:http://dx.doi.org/10.1016/j.mseb.2007.01.044.

[15] L. Seals, J.L. Gole, L.A. Tse, P.J. Hesketh, Rapid, reversible, sensitive porous silicon gas sensor, J. Appl. Phys. 91 (2002).

[16] S. Ozdemir, J.L. Gole, The potential of porous silicon gas sensors, Curr. Opin. Solid State Mater. Sci. 11 (2007) 92–100. doi:http://dx.doi.org/10.1016/j.cossms.2008.06.003.

[17] I. Lundström, S. Shivaraman, C. Svensson, L. Lundkvist, A hydrogen−sensitive MOS field−effect transistor, Appl. Phys. Lett. 26 (1975).

[18] M. Fleischer, M. Lehmann, Solid state gas sensors - Industrial applications. The power of nanomaterial approaches in gas sensors, Springer-Verlag Berlin Heidelberg, 2012.

[19] O. Casals, T. Becker, P. Godignon, A. Romano-Rodriguez, SiC-based MIS gas sensor for high water vapor environments, Sensors Actuators B Chem. 175 (2012) 60–66. doi:http://dx.doi.org/10.1016/j.snb.2011.12.032.

[20] T.D. Burchell, Carbon Materials for Avanced Technologies, Elseview Science Ltd., Oxford, 1999.

[21] W. Yuan, G. Shi, Graphene-based gas sensors, J. Mater. Chem. A. 1 (2013) 10078–10091. doi:10.1039/C3TA11774J.

[22] N. Yamazoe, New approaches for improving semiconductor gas sensors, Sensors Actuators B Chem. 5 (1991) 7–19. doi:10.1016/0925-4005(91)80213-4.

[23] J. Kong, N.R. Franklin, C. Zhou, M.G. Chapline, S. Peng, K. Cho, et al., Nanotube Molecular Wires as Chemical Sensors, Science (80-.). 287 (2000) 622–625. doi:10.1126/science.287.5453.622.

[24] O. Monereo, J.D. Prades, A. Cirera, Self-heating effects in large arrangements of randomly oriented carbon nanofibers: Application to gas sensors, Sensors Actuators B Chem. 211 (2015) 489–497. doi:http://dx.doi.org/10.1016/j.snb.2015.01.095.

[25] O. Monereo, S. Illera, A. Varea, M. Schmidt, T. Sauerwald, A. Schutze, et al., Localized self-heating in large arrays of 1D nanostructures, Nanoscale. 8 (2016) 5082–5088. doi:10.1039/C5NR07158E.

[26] E. Comini, G. Faglia, G. Sberveglieri, Z. Pan, Z.L. Wang, Stable and highly sensitive gas sensors based on semiconducting oxide nanobelts, Appl. Phys. Lett. 81 (2002).

[27] S. Barth, F. Hernandez-Ramirez, J.D. Holmes, A. Romano-Rodriguez, Synthesis and applications of one-dimensional semiconductors, Prog. Mater. Sci. 55 (2010) 563–627. doi:10.1016/j.pmatsci.2010.02.001.

[28] M.W.G. Hoffmann, J.D. Prades, L. Mayrhofer, F. Hernandez-Ramirez, T.T. Järvi, M. Moseler, et al., Highly Selective SAM–Nanowire Hybrid NO2 Sensor: Insight into Charge Transfer Dynamics and Alignment of Frontier Molecular Orbitals, Adv. Funct. Mater. 24 (2014) 595–602. doi:10.1002/adfm.201301478.

[29] P. Ivanov, M. Stankova, E. Llobet, X. Vilanova, J. Brezmes, I. Gràcia, et al., Nanoparticle Metal – Oxide Films for Micro-Hotplate-Based Gas Sensor Systems, October. 5 (2005) 798–809.

[30] L. Fernandez, S. Marco, A. Gutierrez-Galvez, Robustness to sensor damage of a highly redundant gas sensor array, Sensors Actuators B Chem. 218 (2015) 296–302. doi:http://dx.doi.org/10.1016/j.snb.2015.04.096.

[31] S. Roy, K.S. Chandan, MEMS and Nanotechnology for Gas Sensors, CRC Press, 2015.

[32] K.W. Kolasinski, Surface science, Foundations of catalysis and nanoscience, John Wiley & Sons, Chichester, 2012.

[33] J.M. Thomas, W.J. Thomas, Principles and Practice of Heterogeneous Catalysis, Wiley-VCH Verlag GmbH & Co, Weinheim, 2015.

[34] E. Zaremba, W. Kohn, Van der Waals interaction between an atom and a solid surface, Phys. Rev. B. 13 (1976) 2270–2285. doi:10.1103/PhysRevB.13.2270.

[35] J. Tao, A.M. Rappe, Physical adsorption: Theory of van der Waals interactions between particles and clean surfaces, Phys. Rev. Lett. 112 (2014) 1–5. doi:10.1103/PhysRevLett.112.106101.

[36] J.E. Lennard-Jones, Processes of adsorption and diffusion on solid surfaces, Trans. Faraday Soc. 28 (1932) 333–359. doi:10.1039/TF9322800333.

[37] V. Bortolani, N.H. March, M.P. Tosi, Interaction of atoms and molecules with solid surfaces, Springer Science+Business Media New York, New York, 1990.

[38] M.C. Desjonequeres, D. Spanjaard, Concepts in surface physics, Springer-Verlag Berlin Heidelberg, Heidelberg, 1993.

[39] A.W. Adamson, A.P. Gast, Physical Chemistry of Surfaces, Joh Wiley & Sons, New York, 1997.

[40] H. Lüth, Solid Surfaces, Interfaces and Thin Films, Springer-Verlag Berlin Heidelberg, 2010.

[41] W. Göpel, K.D. Schierbaum, SnO2 sensors: current status and future prospects, Sensors Actuators B Chem. 26 (1995) 1–12. doi:10.1016/0925-4005(94)01546-T.

[42] N. Barsan, U. Weimar, Conduction model of metal oxide gas sensors, J. Electroceramics. 7 (2001) 143–167. doi:10.1023/A:1014405811371.

[43] Z. Zhang, J.T. Yates, Band Bending in Semiconductors: Chemical and Physical Consequences at Surfaces and Interfaces, Chem. Rev. 112 (2012) 5520–5551. doi:10.1021/cr3000626.

2. FABRICATION AND CHARACTERIZATION TECHNIQUES

Abstract

This chapter describes the growth techniques used for the synthesis of NWs, which are the fundamental part of the gas sensors studied in this thesis. The fabrication methods for contacting the nanowires used for the study of the materials and gas sensors employed in this thesis will be detailed, with the most important procedures and aspects of the technologies. Specifically, Focus Electron- (FEBID) and Focus Ion-Beam Induced Deposition (FIBID), as well as Electron Beam Lithography (EBL) techniques will be presented and discussed. Furthermore, the electrical characterization, gas mixing and testing systems will be described.

2.1. Introduction

The research on nanostructures, as nanotubes, nanowires, nanorods or nanopillars, among others, has been intensively developed during the last years to study their enhanced physical and chemical properties, focusing on the achievement of reliable devices that could exploit these properties. This field, nanotechnology, has gained a huge interest in last three decades since the discovery of the buckminsterfullerene in 1985 [1] and the carbon nanotubes (CNT) in 1991[2].

Since then, huge efforts have been made in the search for new materials which, at the same time, has been supported by the development of new tools and equipment that allow to study the physical and chemical properties of the materials at nanometre scale. The invention of the Scanning Tunnelling Microscope by Binnig and Rohrer in 1981, the Atomic Force Microscopy in 1986, enhanced the field by providing new tools for the study and fabrication at a scale that was not possible before. Scanning and Transmission Electron Microscopies, which were developed decades before, were the initial pillars for advancing in the study of these new materials.

Within the nanotechnology, huge amount of works are centred on the fabrication of reliable devices based on nanosized structures, where nanofabrication develops a fundamental role. Nanofabrication is defined as the field that involves the processes and methods of constructing engineered nanostructures and devices having minimum dimensions lower than 100 nm [3]. The development of a variety of nanofabrication techniques facilitated the increase of knowledge and understanding of the characteristics of nanostructures, and also the integration into multitude of different functional devices. Nevertheless, nanofabrication approaches are still challenging and complex, due to the difficulties to integrate nanostructures in the macro and micro technologies. Usually, these processes are highly time consuming and require multiple steps, which difficult their implementation into a commercial product due to the impact in the final costs. Furthermore, reproducibility and repeatability of the finished devices is an important issue that must be overcome in the nanofabrication field.

Electron Beam Lithography and Focused Ion Beam are two of the most important tools for nanofabrication and nanolithography due to their functionality and precision. In the present work they have been employed for the fabrication of gas nanosensors based on single nanowire devices, which is a consolidated research line at the

Departament d'Electrònica. Both techniques will be described in this chapter. The equipment used to characterize the fabricated devices electrically and also for the gas sensing measurements will be detailed in this chapter too, as well as the advanced substrates employed for the contacting procedure of the nanowires.

2.2. Synthesis of nanowires

One dimensional semiconducting nanostructures have been investigated since the late 1990 for different applications, due to their novel electronic, thermal and mechanical properties, among others. Nanotubes, nanorods or nanowires fall within this classification. The first semiconducting nanowires (Ge and Si) with a diameter below 100 nm were synthesized few years after the discovery of the carbon nanotubes, namely in 1998 [4]. Since then, huge progress has been made in finding new synthesis methods of nanostructures.

The growth of inorganic and organic one-dimensional structures may be classified as metal-nanoparticle mediated or non-seeded methods. Among others, Vapour-Liquid-Solid (VLS) [5], Solution Liquid Solid (SLS) [6] and Supercritical Fluid-Liquid-Solid (SFLS) [7] use a metal catalyst for the growth. These techniques have in common that the nanoparticles that are used as seed for the growth are molten. Briefly, these methods are based on the eutectic alloy of the chemical precursor with the molten nanoparticle, independently of the phase at which the precursor is found, reaching the precursor supersaturation in the alloy, situation at which the nanowire growth initiates. The phase at which the precursor is found differentiates the mentioned methods and, consequently, the temperature, pressure and other key process parameters during the growth. Each method is suitable for some specific materials, and may allow to tune important parameters of the nanowire, as the diameter, length or growth direction.

SLS is based on the rapid injection of the precursor into a hot solvent and requires low-melting point metal catalysts, which demand relatively low growth temperature. SLS allows growing single crystalline colloidal nanowires. It offers a systematic control of the diameter of the NW, but does not allow to control the crystal structure and growth orientation. Using a pressurized supercritical fluid, instead of a solution, allows to increase the growth temperature, which is the basis of the so-called SFLS. The process is carried out at high pressures in the range of 200-300 bar, using solvents as hexane or

CO_2. SLS and SFLS allow the growth of small diameter NWs, below 10 nm. VLS is probably, the main growth method used for synthesizing semiconductor nanowires using metal catalyst due to the ability to produce a wide variety of materials. This process, which is the approach used in this thesis, will be detailed in the next subsection.

Template-Directed methods generate the nanowires by filling a template structure or covering its sidewalls with a film, e.g. using atomic layer deposition (ALD) or inducing the growth of the material by means of electrodeposition, followed by a subsequent removal of the template.

One of the most common templates is anodized aluminium oxide (AAO) that contains cylindrical nanochannels created by anodisation of aluminium. AAO template allows to grow nanowires of a huge variety of materials. This procedure that was first reported in 1996 [8] and is versatile in terms of materials available for the synthesis, either organic or inorganic. Its main drawback, however, is that the predominant synthesized structures are either amorphous or polycrystalline.

Many other synthesis methods are found for the elaboration of one dimensional nanostructure, like electrospinning, which allows to fabricate polymer and metal oxide nanofibers [9], or chemical etching, a top-down process where pre-defined shapes are produced with the use of masks [10]. A full description of these methods can be found in [11].

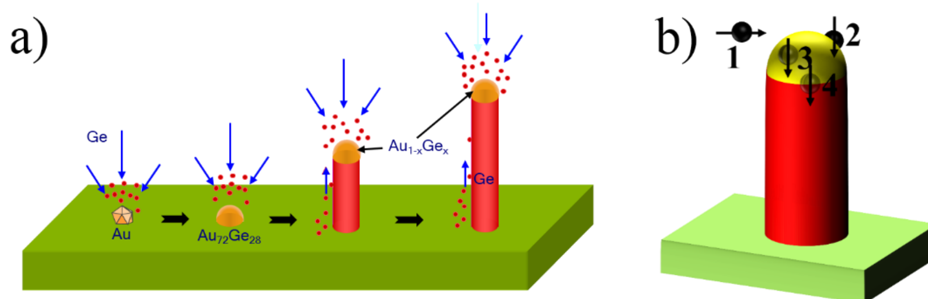

Figure 2.1 a) VLS mechanism of growth of Ge NW using diphenyl germane ($C_2H_{14}Ge$) as a gas precursor. The precursor is decomposed on the gold nanoparticle and a eutectic alloy is formed. Once the superstation of the alloy is reached, Ge precipitates and the NW growth is initiated; b) TEM image of Ge NW with the Au nanoparticle on the tip; c) Kinetic steps in VLS mechanism: (1) mass transport in the gas phase, (2) chemical reaction on the vapour-liquid interface, (3) diffusion in the liquid phase, (4) incorporation of atoms in a crystal lattice. Adapted from [13].

2.2.1. Vapour-Liquid-Solid Mechanism

The VLS growth process employs a gas precursor and molten metal nanoparticles to define and initiate the nucleation and to promote the activation or the decomposition of the molecular reactants. The metal nanoparticles are heated above the eutectic temperature of the alloy formed by the decomposed precursor and the metal. The precursor in the gas phase is continuously added to the eutectic alloy until supersaturation of the adsorbate is reached, which will result in its precipitation, creating a liquid/solid interface between the eutectic alloy and the precipitated material.

A representation of the VLS process is found in Figure 2.1 a), where the example of Ge NW growth using diphenyl germane as a precursor is represented. The metal catalyst remains at the tip of the nanowire, and the precipitation of the material takes place at the liquid/solid interface. The eutectic temperature, the minimum temperature at which the alloy is found in liquid phase for both components, is lower than the melting temperature of Au or Ge [12]. It should be noted that the eutectic temperature of an eutectic alloy at the nanoscale differs of those of a bulk system, and is dependent on the size of the alloy, as reported for Ge-Au system [12].

The VLS mechanism comprises 4 different steps: (1) mass transport in the gas phase, (2) chemical reaction at the vapour-liquid interface, (3) diffusion in the liquid phase and (4) precipitation and incorporation of atoms in a crystal lattice, which are represented in Figure 2.1 b). These steps define the kinetics of the overall process, which depends strongly on each specific nanowire and nanoparticle material.

VLS is carried out in combination with different precursor producing techniques, each of them giving rise to diverse crystalline yields, such as chemical vapour deposition (CVD), laser ablation (LA) or molecular beam epitaxy (MBE).

CVD is the most used approach, where the precursor material is introduced in gas phase or evaporates from a solid powder or liquid solution, decomposing at a controlled temperature and pressure. This technique provides the highest variability of deposition parameters, since pressures from 10^{-3} Torr to atmospheric pressure may be kept during the deposition process, and also wide ranges of gas partial pressures or temperatures. LA uses a solid material which is sublimated as a result of a local heating provided by a pulsed laser radiation. This approach was used in the first demonstration of the growth of NWs in 1998 [4]. MBE, on the other hand, evaporates the phase-forming elements

under high-vacuum conditions, and condensates them on a heated substrate surface. The transport of the precursor takes place without any carrier gas in MBE, which gives rise to structures with a higher crystalline quality, but on the expenses of a much lower deposition rate. Monocrystalline nanostructures may be obtained by any of the three mentioned methods.

2.2.2.1 The role of metal nanoparticles

The size of the liquid metal nanoparticles determines, in most cases, the diameter of the nanowires, as it was demonstrated in [14], where the diameter of Si NWs grown by CVD were controlled by the diameter of the nanoparticles used for the nucleation. In fact, the NW diameter is generally slightly larger than the nanoparticle size, observed at the tip of the NW, as a result of the supersaturation of Si in Au that leads to an expansion of the eutectic alloy. Of course, this depends on each particular material system. The presence of the nanoparticle at the tip, is also a proof of the involvement of VLS process in the growth.

Generally, noble and transition metals are used as a catalyst of the VLS mechanism. Several requirements must meet the metal nanoparticles in order to promote the VLS mechanism [13]:

i) The metal must form a liquid alloy with the compound that has to precipitate in the solid phase.
ii) The solubility limit of the catalyst must be much higher in liquid than in the solid phase. Thus, the solid catalyst should remain at the tip of the NW, which has an additional benefit as it reduces the catalyst contamination in the final grown material.
iii) The vapour pressure of the catalyst should be small in order to avoid the evaporation of the catalyst.

Instead of using metal nanoparticles, the growth may be self-catalytically promoted, by using seeds from the material that is proposed to be grown. The benefit would be that self-catalysed growth avoids the incorporation of the metal catalyst into the NW, which may alter some of its physical properties. As an example, ZnO NWs are self-catalytically grown depositing a ZnO seed layer, and heating the substrate above the melting point of Zn [15]. In the referenced work, the zinc oxide layer was deposited by

decomposition of a zinc acetate precursor, and the NW growth was performed at 500°C while flowing the zinc acetate precursor. The presence of reducing organic solvents during the NW growth reduces ZnO to Zn, which is molten and alloyed with solid ZnO. Zn acetate vapour decomposes at the solid/liquid interface, and the NW growth is then started. The oxygen supply is provided by the oxidized ZnO film below the droplets, which was confirmed by the absence of NW growth when ZnO buffer layer was avoided [15]. In order to obtain a self-catalytically promoted VLS method, a binary, ternary or more complex compound must be employed.

The enhanced growth of the NWs due to the lowering of the activation energy by the metal nanoparticle is observed in the majority of the cases. However, for the NWs grown by MBE, the nanoparticles play a different role because the reaction is not catalysed since the vapour-phase precursor is evaporated/sublimated from a pure target, and no gas decomposition takes place [16]. However, as in the other VLS methods, the metal nanoparticle in MBE promotes the absorption of the vapour phase molecules, because the chemical potential is lowered for a molecule dissolving into a liquid phase material.

In the VLS method, the process is thermodynamically driven, and thus, the growth mode (the growth direction) is the one that minimizes the free energy, which is a situation observed typically analysing the grown structures. The bulk energy of the nanowire, the energy of the liquid/solid (metal/nanowire) interface, and the vapour/solid (gas precursor/nanowire) energy form part of the free energy of the growth.

As an example, in [17] Ge NWs have been observed to vertically grow predominately along the <111> direction on clean monocrystalline Si, on different substrate orientations, namely (111), (110), and (100) substrates, which did not have any silicon dioxide on the top [17]. The epitaxial growth of Ge was obtained independently of the crystal orientation of the silicon substrate, showing a tilted growth of the Ge NWs when Si (100) and (110) substrates were used. Additionally, a certain orientation of the nanowires may be deterministically achieved by selecting a substrate with a lattice structure matching and similar symmetry to that of the nanowire crystalline material [18]. For nanowires, the lattice mismatch at which the epitaxial growth occurs, compared to thin films, may be unusually high, due to the higher ability to relax the induced strain during the growth [19].

The epitaxial growth is hindered by the presence of an interface oxide layer, avoiding the promotion of a deterministic direction growth. The growth is therefore anisotropic, i.e., nanowires may grow along all directions, but a preferential direction of the nanowires is found in front of others.

2.2.2.2 Details of VLS methods used in this thesis

The NWs grown in this thesis have been synthesized by means of a CVD process. CVD techniques involve the thermolysis, hydrolysis, oxidation or reduction of the solid material or gas precursor during the process. The precursor is dissociated by thermolysis when it reaches the nanoparticle surface as, for instance, in the case of SnO_2 NWs growth, $Sn(OtBu)_4$ [20].

Several particular methods have been used to achieve the growth of NWs in this thesis. They all share that they follow the VLS process using a CVD methodology. The differences among them are linked to particular ways of obtaining the gas precursor or to achieve the required temperature for the thermolysis of the precursor and the growth of the nanowires.

The SnO_2 NWs contacted by EBL are grown by a CVD process in a cold-wall quartz reactor in which a high-frequency field is used to inductively heat the substrates (Si or Al_2O_3) by placing them on a graphite susceptor. The temperature is kept at around 700°C, and the process is catalysed by a Au layer of 3-5 nm thickness that forms nanoclusters when temperature is raised. The precursor used is $Sn(OtBu)_4$, which is decomposed on the Au nanoclusters.

The SnO_2 and Ge NWs locally grown on micromembranes or microhotplates are synthesized by a procedure detailed in chapter 3. A specific chapter is dedicated to the growth process due to the innovative and novel features of the procedure, which offers several advantages from the standard CVD growth of NWs.

2.3. FIBID and FEBIP inside a FIB-SEM Dual Beam

Focused Ion Beam (FIB) is a technique that uses a focalised beam of highly energetic ions to scan a surface, using electrostatic and magnetic lenses for focusing and deflecting purposes that was developed in the 70s for localised material removal by sputtering. The technique was further developed for its use as a mask-less

nanolithography system that allows to define nanopatterned features, but due to the associated low throughput and relatively high damage and modification of the ion bombarded materials, the methodology has almost disappeared.

FIB systems, nowadays, are made in combination with a Scanning Electron Microscope (SEM), giving rise to the so-called Dual-Beam, Cross-Beam or FIB-SEM systems, which allow to combine the benefits of both techniques. From the resolution point of view, it competes, to some extent, with electron beam lithography (EBL). An advantage of FIB in combination of vapour precursors introduced into the working chamber is that it allows gas decomposition that can be used for local maskless deposition (FIBID) [21] or enhanced chemical etching [22], which converts the FIB into a nanofabrication laboratory.

The work developed by the MIND Group of the Departament d'Electrònica, started 13 years ago, was pioneer in the field of the use of Dual Beam systems for fabrication of reliable nanosized contacts to individual nanomaterials (nanowires, nanotubes and nanoparticles) to form nanodevices and that allowed their electrical characterization, by using a combination of both electron and ion beams. The dual-beam system allows to acquire electron images instead of the damaging ion-based images, and also to perform focused electron-beam induced depositions of different materials by dissociating metalorganic gas compounds, which allows to overcome the problems related to FIB technology, i.e., implantation, milling and damage.

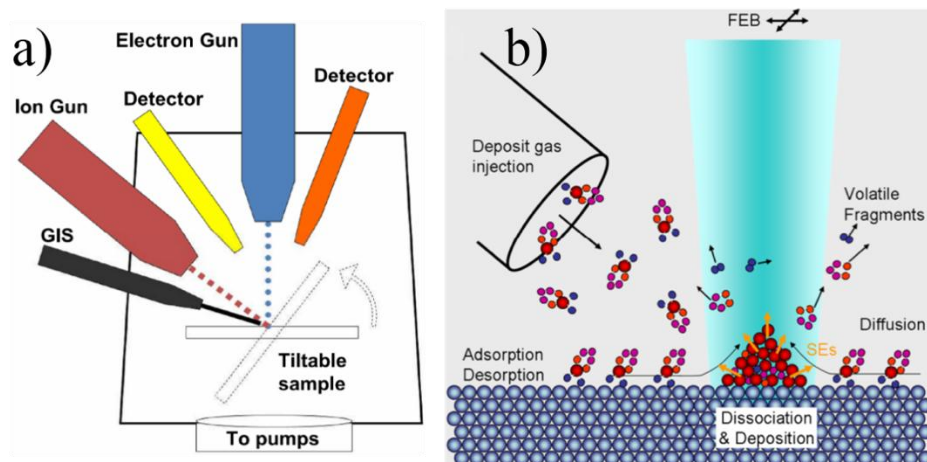

Figure 2.2 a) Scheme of SEM-FIB machine, showing the disposition of the electron and ion guns (whose beams intersect at an angle of 52º), the respective detectors and the gas injection system (GIS). b) Decomposition mechanism of the precursor at the sample surface induced by the electron beam, where deposition of fragments of the decomposed precursor can be seen. The mechanism also works for the ion beam. Images obtained from [23].

A FIB-SEM system is basically, a SEM in which an ion column, consisting of an ion gun and ion optics, is introduced and where both beams can be focused on the same point. The samples are placed in the SEM chamber. The equipment allows to perform with nanometre sized precision and *in situ*: i) ablation of material (milling) via sputtering of the ion beam; ii) deposition of the material through the decomposition of a gas precursor by means of ion or electron beam, which is named Focused Ion Beam Induced Deposition (FIBID) or Focused Electron Beam Induced Deposition (FEBID), respectively.

A Focused Ion Beam (FIB) – Scanning Electron Microscope (SEM) Dual Beam system (FIB), FEI Dual Beam Strata 235 or FEI Helios Nanolab, has been used for the fabrication of platinum contacts at a nanometre scale. The electron column allows the acceleration of the electrons from 0.5 to 30 kV, which is equipped with a Field Emission Gun (Schottky emitter). The ion column (Ga^+) accelerates the ions at 5, 10 and 30 kV and, with the use of different apertures, allows an ion current range from 1 pA to 20 nA. The microscope is equipped with an EvertHart-Thornley secondary electrons detector (SED) for electron imaging. The beams of both columns intersect at an angle of 52º (see Figure 2.2 a) for details). A sample holder with 6 degrees of freedom allows to move the sample in the three directions x, y, z, rotate it in the plane of the sample holder (along z axis), and tilt it through a parallel axis of the holder (x, y axes). The sample is located and may be oriented in different planes at the so-called eucentric height, the height at which the ion and electron beam are designed to intersect.

The instrument is equipped with a gas injection system (GIS) with 4 gas injectors, each consisting in a cylindrical tube nozzle that is used for gas-assisted deposition or etching with FEB or FIB. GIS supplies a high and localized molecular flux into the chamber, near the electron- or ion-beam impact area, while the overall chamber pressure is kept low enough for electron and ion beam operation. The metalorganic precursor trimetyl-methylcyclopentadienylplatinum $[(CH_3)_3(CH_3C_5H_4)Pt]$, the standard precursor for platinum deposits in the FEI machines, has been used for contacting individual NWs. Platinum structures can be deposited by mean of FEBID and FIBID processes. Scanning the sample by either electron or ion beam while keeping the metalorganic flow leads to the dissociation of the precursor molecules once it is previously adsorbed at the sample's surface. A scheme of the process is represented in

Figure 2.2 b), where it is observed that the heavier part of the molecule remains attached to the surface, and the lighter part is taken away by the vacuum pumping system.

The probability that an electron induces the decomposition of the precursor molecule depends on the electron energy, and is expressed as a cross-section (cm^2). The electrons that are able to produce the scission are those with an energy of a few eV [24]. Thus, the main contribution to the dissociation of the gas precursor molecules is due to the secondary electrons (SE), which are produced through the ionization of the specimen by the primary electrons and whose energy is smaller than 50 eV [25,26]. However, backscattered electrons (BSE), and forward scattered electrons (FSE) also play a role. The maximum depth of the secondary electrons that can reach the surface is 1 nm for metals and 10 nm for dielectric materials [26].

The backscattered electrons (BSE) are produced by the elastic interaction of primary electrons with the nuclei of atoms from the substrate. The BSE have energies above 50 eV [26]; despite to be considered as an elastic scattered products, they lose some energy as a result of some inelastic scattering with the substrate. They reach a scattering angle up to 180°, and the fraction of the BSE depends strongly on the atomic number (Z) of the interacting nuclei. Therefore, the higher the Z, the higher the probability to produce BSE, which is the fundamental mechanism of the BSE detectors, which allow high resolution compositional maps. The electrons used in BSE detector have approximately the 80% of the energy of the primary beam [25].

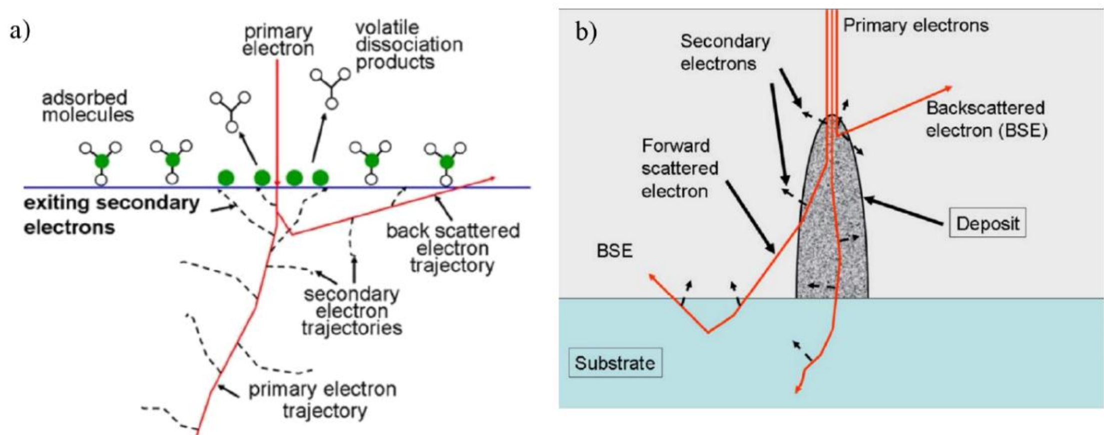

Figure 2.3 Diagram of the scattering of primary electrons impinging on a substrate. a) Primary electrons are back scattered and go out of the surface at a certain distance from the primary beam. During the loss energy of the electrons, secondary electrons are produced in the substrate and a part exits the surface; b) once a 3-D structure has been deposited, the forward scattered electrons reach the surface and also generate secondary electrons as depicted in the picture. This image illustrates the process of a continuous vertical structure fabrication. Images taken from [27].

Forward scattered electrons are those electrons that experience small angle scattering events, which broaden the primary electron beam. This effect is caused by electron-electron interactions, and their contribution is minimum in the initial stages of the decomposition of the gas precursor, because they do not reach the surface, i.e., do not interact directly with the gas molecules.

Notwithstanding the electron beam has a diameter typically of 1-3 nm, the lateral dimension of the smallest platinum deposits is about 15-20 nm, since the scattered secondary electrons exit from a wider area than where the electron beam is focused in. The confinement of the electrons to the area defined by the primary electrons (PE) is compromised by elastic and inelastic scattering processes with the specimen.

The scattering events involved during the FEBIP deposition are represented in Figure 2.3 a). A part of the primary electrons is backscattered and exits the surface at a distance from the PE that depends on the scattering angle and the electron energy. The PE and backscattered electrons may lose energy during the interactions with the substrate due to inelastic, ionizing processes that generate the SE. The secondary electrons generated at a depth close to the surface are able to induce the fragmentation of the adsorbed precursor molecules.

On the other hand, once the three dimensional deposit is started the forward scattered electrons play a role in the process. FSE reach the surfaces of the substrate and generate SE on the sides of the initial structure, which finally results in a broadening of the structure. The farthest SE generated from the position of the PE lead to the Pt halo, which is a very thin non-desired deposit of Pt around the fabricated structure.

Other authors were able to reduce the lateral dimensions until few nanometres by using high acceleration voltages (100 or 200 kV), that mainly produces secondary electrons of low energy (2-10 eV). The broadening caused by the SE is reduced due to the reduced mean free path associated, between 1-5 nm [28,29].

Concerning the Focused Ion Beam Induced Deposition, the process is based on the electronic and nuclear collision of the incoming ions with the substrate. Gallium ions lose a significant fraction of the energy in nuclear collisions, which results in a reduced depth that the ions penetrate into the substrate. Secondary electrons are produced during the collisions of the primary ions, which gives rise to the scission of precursor molecules. They also may dislocate atoms from the substrate that in a cascade effect

may collide with closer atoms, which results in sputtering of excited surface atoms around the primary ion beam [30]. This effect may be prevented by lowering the ion current and adjusting some parameters of the deposition, as it will be explained later.

The deposition rate is favoured for FIBID in front of FEBID, as a result of the higher ability to produce secondary electrons in the subsurface region. Furthermore, the deposition rate has a low dependence on the incident energy of the ions; oppositely, this is increased by a factor of eight for platinum deposited by FEBID, when the electron beam energy is lowered from 30 to 5 keV, due to the larger number of generated secondary electrons within the escape depth [31]. This is explained by several reasons; first, gallium ions are implanted at about 30 nm below the sample surface, even at the higher energy, allowing the secondary electrons to reach the surface more easily than those produced by FEB, which are stopped at a depth of several micrometres from the surface [23,24]. It is important to note that secondary electrons generated at depths of 10-30 nm or above cannot reach the surface with enough energy to overcome the surface barrier, which depends slightly on the material [23]. Thus, the higher the beam energy of the electrons, the higher the fraction of secondary electrons that cannot reach the surface, and, therefore, the FEBID yield decreases.

Moreover, other input parameters for the depositions are the dwell time and overlapping of the focused electron (or ion) beam. Dwell time is the time that the electron (or ion) beam stays at a certain position. Overlap is defined as the area overlapped when the beam moves from one position to the next and, in the FEI machines, is calculated in terms of percentage of area. A high overlap leads to a smaller pitch, i.e., a smaller distance between one position and the subsequent at which the beam is focused at a time equal to the dwell time. The pitch is a function of the beam magnification at which the deposit is done and the spot size, which is, at the same time, depending on the beam current. Some studies related to the effect of dwell time or overlapping on the deposition yield in FEBID differ in the obtained results, consequently, deeper studies must be performed for a better understanding [26] but are not addressed in this thesis.

For the deposition using FIBID, low ion current, very short dwell times and negative overlapping need to be used in order to minimize the milling of the material that occurs during ion bombardment and to enhance the platinum deposition. It is important to

notice that FIBID involves the ion implantation on the sample's surface, which may dope the material and change the conduction properties.

The electron or ion beam assisted platinum resulting deposition is basically platinum nanoparticles embedded in a carbon matrix [31], with sizes between 3 and 8 nm, being the Pt nanoparticles larger for the FIBID case. Furthermore, Gallium is also implanted in the deposited matrix but only when performing FIBID. In both cases, the deposited platinum has a high carbon content, although platinum content is higher in FIBID process, since the gas dissociation process is more effective with ions. Initially, on the first layers, FIBID of Pt have high carbon content that is reduced as the thickness increases [32]. The high carbon content of the deposits leads to resistivity values several orders of magnitude above those of bulk Pt. Resistivity of electron and ion beam assisted platinum deposits are in the range of 10^6 μΩ·cm and 10^3 μΩ·cm respectively, much higher than bulk Pt, which is around 11 μΩ·cm [24].

2.3.1. Electrical contact fabrication for the NWs

The grown nanowires are placed on top of microhotplates and electrically contacted. Microhotplates are suspended microplatforms with a buried microheater and interdigitated electrodes on the top. The details of the microhotplates are described in section 2.5. Since the ion beam assisted deposition may damage or dope with gallium ions the NW, electron beam is always used to assist the deposition of platinum nanocontacts on the region closer to the NW. The extension towards the outer contacts are carried out by FIBID because of the higher conductivity of the resulting structures and the higher deposition rate.

An important issue in all this process is that the contribution of Pt contacts to the total resistance of the fabricated nanostructure is not negligible, since both electron and ion beam induced contributions are quite resistive, the former being the most important. Additionally, the contact resistance between the NW and the nanocontact, due to the differences in electron affinity and work function of the materials, plays a major role. In order to minimise the resistance contribution of the contacts, fabrication and electrical measurement in 4 contacts configuration is required.

The whole process is performed as follows. Firstly, the nanowires are removed from the substrate were they were grown, typically alumina or silicon, by sonicating the

substrate while it is immersed in a solvent. The most common used solvents are ethanol, isopropanol or toluene. Afterwards, a droplet of the solvent with the removed NWs, of about 20 µl, is put on the microhotplate using an automated micropipette. As a consequence, the NWs are randomly oriented on the surface of the microhotplate, and prepared then for the contacting step. An appropriate amount of solvent for a given density of nanowire on the substrate must be used, in order to reach a compromise between a reasonable quantity of nanowires at the surface and avoiding a heap of NWs.

The electrical contacts are fabricated *ad hoc* for each nanowire. Once the sample is introduced in the FIB-SEM chamber, the microhotplates are imaged by SEM to find a suitable nanowire for contacting. The process starts with the fabrication of FEBID contacts close to the NW, with dimensions (length x width x thick) typically of 10 x 0.3 x 0.3 μm^3 and extending them to the microfabricated electrodes of the sample by using FIBID.

Sample stage must always be perpendicular to the beam that induces the platinum deposition, therefore, the stage is kept at 0º for FEBID and tilted to 52º for FIBID, holding it at the eucentric height. The deposition parameters used during the Pt deposition are summarized in Table 2.1.

Table 2.1. Deposition parameters of electron and ion beam induced Pt structures

Parameter	FEBID	FIBID
Acceleration Voltage (kV)	5	30
Sample Current (pA)	100	50
Spot size	3	5
Dwell Time (us)	0.2	0.2
Overlap (%)	90	-200
Width (nm)	250	500
Height (nm)	300	500

Following the described procedure, a single NW is contacted in a total time of 1-2 hours in two probes configuration, and between 2-4 h in four probes configuration.

2.4. Electron Beam Lithography

Electron Beam Lithography (EBL) is one of the most important techniques in nanofabrication, together with FIB-SEM. The EBL technique is based on the exposure of a thin polymer resist by a focused electron beam to modify the solubility of the polymer in a subsequent development [33]. EBL allows to define patterned structures with a size below 20 nm, a dimension that strongly depends on the machine [34].

The technique derives from the early Scanning Electron microscopes, and can work with a wide variety of materials. The first EBL systems were developed in the 60's decade [35], and the discovery of poylmethyl methacrylate (PMMA) as an excellent electron resist followed shortly after [36]. PMMA resist is still the most popular positive-tone resist used, but strong advances have been done in the last decades with the advent of a new series of specific resist for EBL, both positive- and negative tone.

The main application of EBL nowadays is the supporting of the integrated circuit industry. EBL is used to produce the masks for the fabrication of integrated circuits by optical steppers or x-ray lithography.

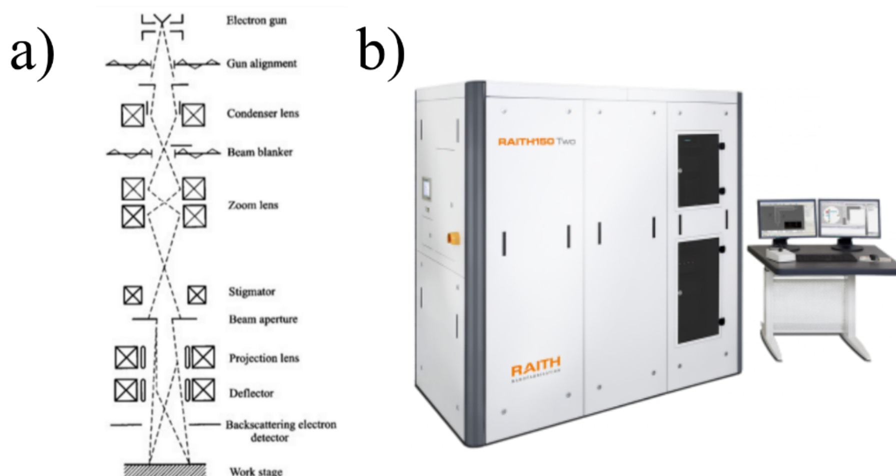

Figure 2.4 a) Scheme of the electron column of EBL system, where the electromagnetic lenses are represented by a X inside of a square; b) EBL system Raith150-Two, the equipment used in this thesis.

Advanced EBL systems are also dedicated for patterning, and employ high brightness systems for higher throughput. The most common EBL systems are equipped with an electron source that accelerates the electron with a tension of 10-30 kV, but equipments with energies up to 100kV are among the most advanced actual systems.

The EBL system is composed by several parts. The SEM column, which contains the electron source, the objective lenses and the beam deflection unit, is represented in Figure 2.4 a). The electron gun is generally a field emission source (Schottky or thermal field type) because it combines a good and stable emission intensity and a reduced energetic dispersion of the electrons, which gives low chromatic aberrations. Magnetic lenses are generally used as an objective lens for focusing the electrons because of their lower aberrations, while electrostatic lenses form the condenser part. The beam deflection unit deviates the beam to position it at different points of the surface of the sample. Other elements found in the electron columns are the apertures, stigmators and beam blanker [35]. The apertures limit the beam current, which has a strong influence in the final resolution. The beam blanker, which is also an aperture, is one of the most important requirement to avoid the electron exposure during the movement of the beam in not-to-be-exposed regions and works by switching off the beam as a result of changing the angle of incidence of the electron beam and leading it to impact outside the aperture [33].

Laser interferometric stages are mainly used in the more advanced systems due to the ability to measure low resolution displacements in a stable way and to allow the projection of a certain pattern in a neighbouring area of an exposed one with an almost perfect matching, which is the so-called stitching. Briefly, a laser line is split by Zeeman effect, where the split-frequency laser is reflected on a mirror at the stage, and the beat frequency from both lines is measured [35]. The beat frequency is the frequency of the resulting wave and changes according to the Doppler effect. Integrating the beat count, the position of the stage is obtained.

The equipment used in the experimental procedure is a Raith 150-TWO, equipped with an electron source that accelerates the electron beam from 10 to 30 kV (see Figure 2.4 b)). Three different apertures may be chosen: 10, 20 and 30 μm, where the higher the aperture, the higher the current that reaches the sample. The system contains a

Secondary Electron Detector (SED) and in-lens detector. The working distance is 10 mm and the vacuum level inside the chamber is similar to FIB systems, i.e., 10^{-6} mbar.

2.4.1. Resist exposure: interactions and limitations

The scission of the positive-tone resists takes place through physico-chemical changes induced by the collisions of the electrons [33]. The smaller fragments remaining on the exposed area are removed when immersed in the specific solvent for the resist, leaving the previously electron exposed patterns as opened windows in the resist layer. Negative-tone resists, on the other hand, are low solubility resists that are converted to high solubility by the cross-linking of their parts, whose exposure and development procedures are more complicated and may be affected severally by the external conditions. Negative resists have not been used in this work.

Concerning the resist-electron interaction, secondary electrons are considered to cause the bulk of the scission of the polymer layer [35]. As explained before, secondary electrons are produced by ionization, resulting from inelastic collisions of the primary beam electrons or other higher energy electrons, and generated in cascade while the electrons interact with the resist.

Primary electrons may suffer low angle scattering due to the interaction with the resist, producing as a result the broadening of the primary beam. The broadening increases with depth, an effect which is known as forward scattering effect. Furthermore, this effect is accentuated at low incident energies, as it is shown in Figure 2.5 [33]. The effective increase in the beam diameter d_f is empirically described by the relationship $d_f = 0.9\ (R_t\ /\ V_b)^{1.5}$ where R_t is the resist thickness and V_b the beam voltage [35]. As shown, the effect is minimized using high acceleration voltages and thin resist films [37].

The beam voltage affects, additionally, the applicable electron dose necessary for the resist scission. The electron dose must be kept within a certain range in order to break the resist into short fragments that must be soluble to the developer, and achieve the subsequent removal of the resist on the exposed patterns. The required dose is influenced by the probability of inelastic collision of the electrons with the resist, from which the secondary electrons are generated. The probability is defined by a cross-section, which is a function of the energy of the incoming electrons, decreasing roughly

in proportion to an increase in electron energy and thus, giving rise to a reduction of the generated secondary electrons. This results in less chain scission per electron for positive resists, which decreases the throughput [33]. Consequently, the applicable electron dose gets wider, as the maximum and minimum doses increases with the acceleration voltage. Since the throughput is reduced, this effect is considered as unwanted as it requires larger times for the exposure, even though the dose constraint is relaxed.

The major part of the electrons passes through the resist, but some of them suffer large angle collisions with the specimen, the so-called back-scattered electrons. BSE may emerge at the incident surface of the resist but at some distance from the incidence point, even some micrometers away. Consequently, BSE give rise to an increased exposure of the resist as a result of the secondary electrons generated in cascade during the followed path, causing a pattern distortion [33].

Thus, the dose that a pattern feature receives is affected by the scattered electrons from other features nearby. This effect is the so-called proximity effect, representing a non-confinement of the delivered electron dose to the shapes defined by the tool.

In general, to avoid the proximity effect when uniform density and linewidth patterns are exposed, the well-adjusting of dose is enough. Another approach for more complicated patterns is based on working with low acceleration voltages, at which the electron mean free path is short. However, just very thin resists may be exposed, limiting considerably the final process.

The resolution of EBL is determined, besides the dispersion of the secondary electrons in the resist layer, by the molecular structure of the resist and the dynamics of the development process. As an example, other approaches that lead to resolution below 20 nm, which is not possible using PMMA resist, is based on hydrogen silsequioxane (HSQ) resist, a negative-tone resist that requires significant higher doses than PMMA [34].

This fact reflects that the resist becomes an important issue for fabricating smaller structures, whose sensitivity, contrast and molecular size influences on the final resolution. The contrast is related to the verticality of the wall defined on the edge of the exposed resist.

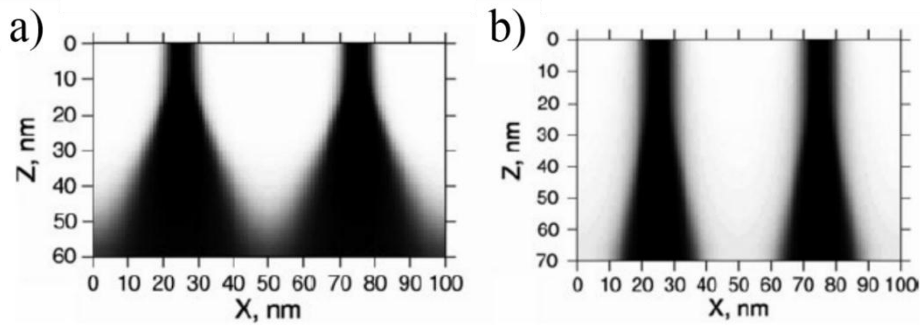

Figure 2.5 Broadening of the electron beam due to the forward scattering in the resist at a) 3 kV and b) 10kV. The dark part simulates the path followed by the electrons, and the results are obtained by the exposure for two parallel beams [33].

Another important parameter to control in EBL, already presented, is the electron dose, which is a function on the specific resist employed. In positive-tone resists, the dose affects the distribution of the fragment sizes in a way that the higher the dose at a certain voltage, the higher the scission of the resist into shorter polymers.

However, a limit of about 10 times the maximum recommended dose must be respected in order to avoid the posterior cross-linking of the fragments that turns the resist insoluble to the developer. Furthermore, a high dose increases, in general, the final dimensions of the pattern, due to the enhanced generation of forward and back scattered electrons.

The electron dose leads to the breaking of the polymer backbone bonds, leaving fragments of lower molecular weight. Once the resist is exposed by the electron beam, the sample is immersed in a liquid developer to dissolve the broken fragments (positive tone resist) or the non-crosslinked molecules (negative tone resist). The developer penetrates the polymer matrix during the development, detaching the fragments from the matrix, which diffuse into the solvent. The longer fragments have lower mobility, and require longer time to be dissolved [33].

The duration of this process is strongly dependent on the employed resist and might be critical: an overdevelopment may lead to a distorted profile of the resist, because of the degradation of the resist-substrate bonds, causing, for instance, the collapse of the pattern for vertical structures [33]. Typically, the development process is stopped by introducing the sample into an inert solvent, like isopropanol, so that the developer is diluted very fast, stopping its action.

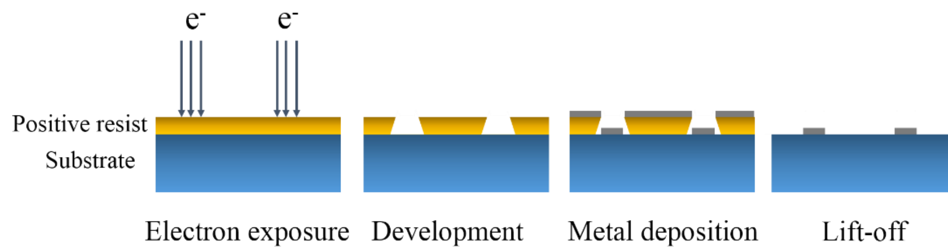

Figure 2.6 Schematic representation of the different steps performed for the fabrication of metal structures by means of EBL. The development of the resist, metal deposition and removal of the resist (lift-off) are represented.

The development may be performed by immersing the substrate in the developer while gently agitating it, or using a spray to spread the developer continuously on the substrate while it is spinning on a spin chuck. A drying in nitrogen procedure follows the previous step. A post-bake of the samples may be performed after the development to remove some developer residues.

The procedure followed in this thesis and its different steps for the fabrication of metal nanostructures are represented in Figure 2.6. In this procedure, the resist is used as a sacrificial layer. As shown in the figure, the electron exposure and the development opens the desired windows in the resist. The metal layer is deposited afterwards over the whole sample, but remains in contact to the substrate only at the exposed areas. Afterwards, the non-exposed resist is removed by an aggressive solvent during the so-called lift-off process, taking away the metal that was on top with it, and leaving only the metal in direct contact with the substrate. A critical issue during lift-off is the profile of the resist after the electron exposure and development.

The undercut resist profile shown in Figure 2.6 is the desired profile for the lift-off procedure, because after the metal deposition the sidewalls of the resist are not covered by the metal, allowing the resist remover to reach the resist layer, and thus, facilitating the lift-off process.

The resist profile may be achieved due to the forward scattering effect at low voltages, for instance, that broadens the beam with the depth, or with a combination of two layers of PMMA resist with different molecular weight.

2.4.2. Contacting procedure for NWs

EBL system has been used to fabricate the electrical contacts to the NWs in order to employ a different technique that could replace the FIB with higher throughput, being less-time consuming and providing more reproducible results.

The method for depositing the NWs on top of the suspended micromembranes is the same as detailed in the previous section for combined FEBID and FIBID procedure. The process to fabricate the contacts once the nanowires are on the top of microembranes, is divided in several steps.

The chips are introduced in the EBL chamber without the resist. First of all, the acceleration tension and aperture must be chosen, together with the writing field size and the magnifications used during the design and fabrication of the contacts.

The microhotplates used are especially designed for the EBL procedure thanks to the incorporation of 4 alignment marks on the membrane which are used to align the electron beam one the sample when, next, the resist is deposited on top, and thus, avoiding the undesired exposure of the resist in the areas of interest. The patterns that will be transferred to the resist are defined on top of the SEM picture of the NW, drawing directly the shape of the electrical contacts on top of the NWs. Each pattern covers a specific position over the NW, located close to the edges, and extends to the microelectrode of the microhotplate.

The procedure has been developed using PMMA solved in anisole, provided by MicroChem. PMMA is a resist composed by a long chain polymer, with a molecular weight between 490 kDa and 950 kDa.

After the design drawing, the chips are spin-coated with PMMA (usually at 1500-5000 rpm range) and prebaked at 180ºC for 1 minute. The sample is introduced back in the EBL chamber. First, the stage is driven to the Faraday cage, where the beam is positioned in order to measure the electron current. Then, the dose exposure and step size is indicated, and the dwell time is calculated as a function of them following *Dwell Time=Dose*·(*Step size*)^2/*Beam current*. The contacts here fabricated are not critical in size, i.e., are far above the resolution limit of PMMA resist using the Raith 150-TWO. However, due to the roughness of the membranes that is defined by the buried heater,

the uniformity of the resist thickness is an important issue for a complete resist exposure.

At that point, the beam is blanked and the stage is moved to the coordinates of the first pattern. Thus, the manual marks are automatically exposed and recognized, correcting any misalignment due to the mechanical hysteresis of the stage, if necessary. All the defined patterns for contacting the NWs are exposed according to the required dose. This procedure is repeated for as much NWs have been selected in the chip and for the different chips.

The samples are then removed from the EBL chamber and developed by immersing them in a solution of methyl-isopropyl-ketone (MIBK) and Isopropyl alcohol (IPA) (1:3) for 30 s and, next, in IPA for additional 30 s, which stops the development process. The samples are immediately nitrogen dried, as a last step of the EBL process.

The fabrication of the contacts to the NWs follows with the deposition of metal layer on top of the resist. The metal layers used in this work are Ti/Pt, fabricated by evaporation or magnetron sputtering, and deposited on the whole sample. Afterwards, the lift-off process is performed by immersing the samples in acetone at room temperature to dissolve the remaining polymer layer. Once the resist and metal layer on top of it are removed, the samples are immersed again in isopropanol to clean the device of the remaining acetone. Thus, the metal film remains in the areas where it was deposited directly on top of the substrate, i.e., the area irradiated with electrons.

2.5. Micromembranes and microhotplates

Micromembranes and microhotplates are the substrates where the nanowires have been contacted individually by either FEBID/FIBIP or EBL procedures, or where they have been locally grown. The fabrication steps of these substrates are detailed in this section.

Micromembranes and microhotplates are micro-sized thin structures that contain both a buried heater and electrodes on the top that have been fabricated on silicon wafers. The use of this kind of structures is interesting due to the small dimensions that allow to provide locally temperatures of several hundreds of °C on the membrane with a

low power consumption, in the range of mW. Furthermore, the reduced mass of the membranes provides a fast thermal response during both heating and cooling ramps.

The main difference between them is that microhotplates are free-standing structures and micromembranes are closed microstructures, i.e., the whole perimeter of the membrane is attached to the thicker substrate. The substrates used in this thesis have been fabricated in collaboration of the IMB-CNM (CSIC), using their Clean Room micro and nanofabrication facility.

The most employed materials for the fabrication of microhotplates or micromembranes are Si_3N_4 and SiO_2, because they have a low thermal conductivity and they minimize the mechanical stress caused by the temperature provided by the heater. Combining the opposite effect of compressive stress of SiO_2 and tensile stress of Si_3N_4 [38], the films give a robust and durable structure. Both materials have been used for the fabrication of both micromembranes and microhotplates.

Micromembranes are bulk micromachined substrates fabricated on double side polished p-type Si substrates, 300 µm thick. The whole thickness of the micromembranes is about 1.1 µm. A layer of 0.3 µm of LPCVD Si_3N_4, deposited on top of the silicon wafer, will be used as a dielectric membrane. The spiral-shaped micro-heater is made from doped polysilicon embedded in the silicon nitride layer. A layer of deposited SiO_2, 0.8 µm thick, acts as electrical isolation to the top. On top of it, Ti/Pt electrodes (25/150 nm nominally thick) are deposited, which provide electrical contact to the structures to be measured.

Two different sizes of micromembranes have been used in this thesis:

i) The larger one provides an active area of 400×400 µm^2 at the center of a membrane of 1×1 mm^2, and the distance between the Ti/Pt electrodes is either 50 or 100 µm. The latter is represented in Figure 2.7 a). These micromembranes have been used as a substrate for the local growth of SnO_2 nanowires, because they achieve higher temperatures than the free-standing membranes, without suffering an irreversible damage.

ii) The smaller micromembrane has an active area of 100x100 µm^2, and the distance between the electrodes is 10 µm, as shown in the Figure 2.7 b). In this substrate, individual SnO_2 nanowires have been contacted by means of EBL.

Concerning microhotplates, the free-standing structures, two different designs of microhotplates have been employed in this thesis, both fabricated by surface micromachining.

i) The microhotplate on top of which Ge NWs have been locally grown is shown in Figure 2.7 c). The membrane consists of a Si_3N_4 layer (700 nm thick), in which the platinum heating element is embedded. SiO_2 layers are found on top (400 nm) and below (50 nm) the Si_3N_4 layer. The total thickness of the membrane is, therefore, 1150 nm. Ti/Pt top electrodes are fabricated using photolithography and subsequent lift-off process on the upper SiO_2 layer, with a thickness of 5/80nm respectively.

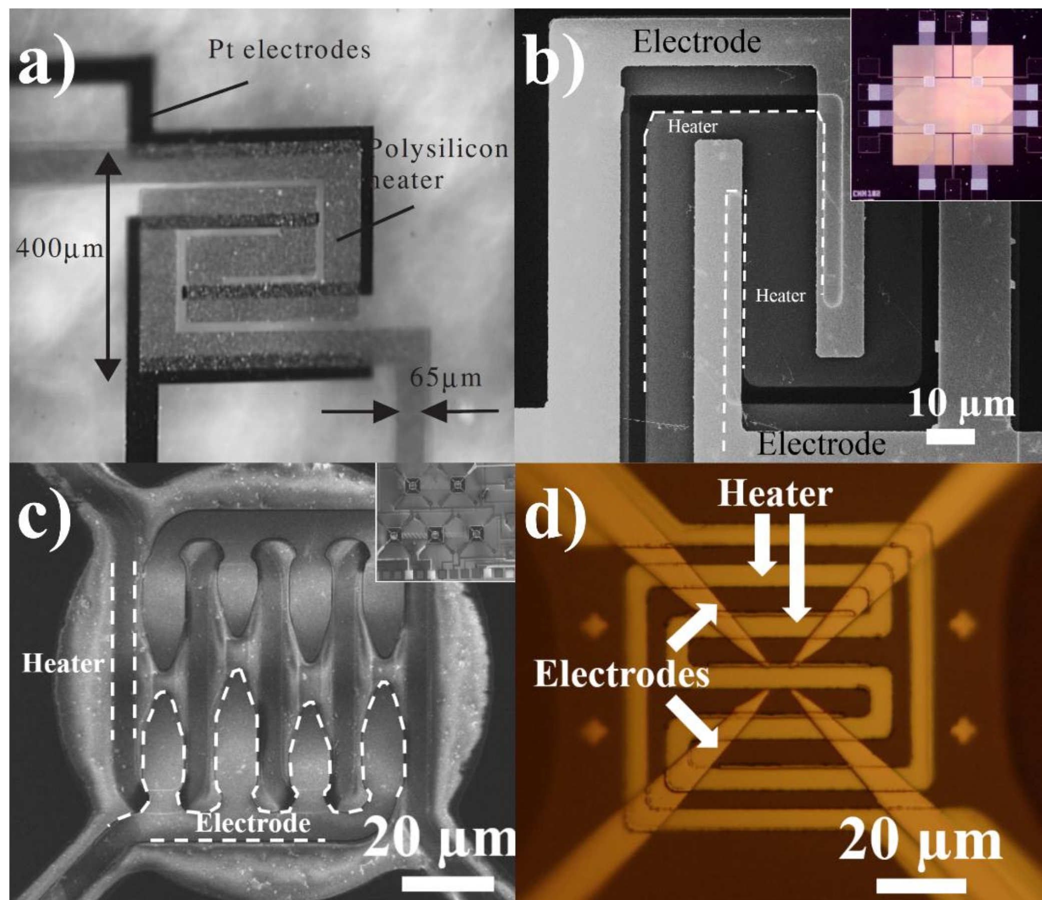

Figure 2.7 a) Closed micromembranes used as a substrate for local growth of SnO_2 NWs. The space between the electrodes is 100 µm; b) Closed micromembranes for contacting individual SnO_2 NWs by means of EBL procedure; c) Free-standing microhotplates employed for local growth of Ge NWs; d) Free-standing microhotplates employed for contacting individual NWs by EBL procedure.

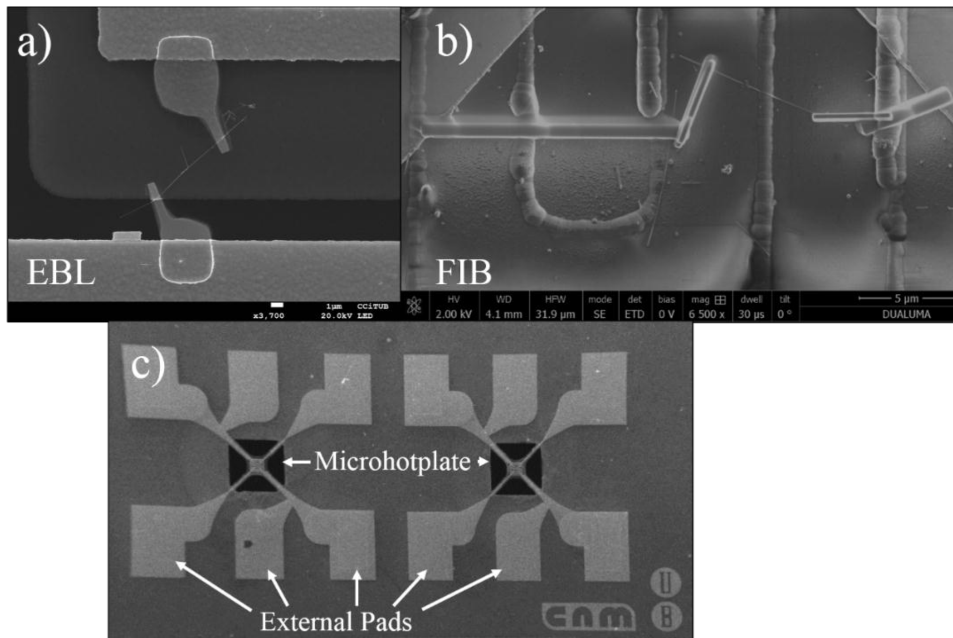

Figure 2.8 SEM picture of a microhotplate with a) NW contacted by EBL; b) NW contacted by FIB-SEM; c) General view of the suspended microhotplate where the external pads for wire-bonding are visible.

ii) EBL processes have been employed for contacting individual nanowires on a different design of microhotplates, shown in Figure 2.7 d). This substrate, like the previous one, contains a Pt heater embedded on PECVD Si_3N_4 layer, whose thickness is 300 nm. On top of it has been deposited SiO_2 800 nm thick with isolation purpose. Afterwards, Ti/Pt electrodes with a thickness of 25/250 nm are deposited. The heating area (100x100 μm^2) is located only in the microhotplate, reaching temperatures up to 350ºC with a consumption of 5 mW.

2.6. Electrical and gas measurements

2.6.1. Electrical measurement setup

The electrical measurement setup is prepared for measuring single and network of NWs devices. The gas sensors with individual nanowires require high accuracy for obtaining the electrical characterization, due to the exceptional reduced dimensions, which require very low current to acquire the electrical response during the gas sensing without damaging the NW, typically in the nA range. Networks of NWs have lower requirements in terms of electrical measurements, due to the allowed multiple paths formed by the different nanowires, supporting higher currents.

Low measuring currents for individual nanowires must be kept in order to avoid also the self-heating of the nanowire, an effect produced due to the reduced mass and the relatively high resistivity of the metal oxide nanowires [40,41]. Self-heating is based on the Joule effect provided by the electrical current employed during the electrical measurement. In order to avoid it, the measurement current must be kept at low values, below about 10-50 nA, but varying from one NW to another due to their different diameters.

Therefore, currents from 100 pA up to 50 nA have been used, depending on the resistance of the measured NWs. Furthermore, a good stability of the electrical output is mandatory in order to avoid any harmful fluctuation. For this reason, Source Measurement Units (SMU) from Keithley have been chosen, which accomplish with the specific requirements. Keithley 2602-A instrument equipped with two SMU, and Keithley 4200 SCS, equipped with three SMU and a ground unit, have been used with this purpose. The equipments provide DC voltage source and measurement values in the range between 1 μV and 40.4 V and DC current from 1 pA to 3.03 A. The required stability and source/measurements ranges for the electrical measurements are delivered satisfactorily by the SMU from Keithley.

2.6.2.1 Macroscopic access to individual NWs

The electrical path for the electrical measurements of single nanowires is formed by several parts. At the smaller level, the contacts are extended from the pre-patterned electrodes to the NW, fabricated by either EBL or FIB. Two SEM images of a NW with the fabricated contacts are shown in Figure 2.8 a) using EBL and b) FEBID and FIBID. The electrodes are accessible from external pads that allow to electrically contact and measure the NW (see Figure 2.8 c)), to which the external equipment is connected.

The electrical measurements are obtained by two different methods:

i) The chips are introduced in a 4-probe station, Karl Suss PM 5 Probe Station with four PH100 Micropositioner Probeheads. The probes connected to the micropositioners allow to contact the electrical pads, and, at the same time, the micropositioners are connected to the Keithley 4200 SCS system.

This approach is useful to measure the first fabricated prototypes in order to study exclusively their electrical behavior, and to check the reliability of the fabrication technique.

ii) In order to intensively study the fabricated devices, the pre-patterned pads are ball-bonded to a TO-8 package with 12 pins, which gives a more robust and gas compatible setup. This procedure is useful for resistance-temperature measurements, for instance, and fits perfectly into the gas testing chamber that is specifically designed with a socket configuration for two TO-8 package, as shown in Figure 2.9. This is the method followed for the electrical measurements during dynamic gas experiments. Two electrical parameters are used during a gas measurement: the heater voltage/current in order to provide the desired temperature for the sensor, and the sensor voltage/current. For this reason, two different SMU units have to be used.

2.6.2. Gas measurement setup

The fabricated sensors must be characterized in controlled atmosphere, gas flow and temperature conditions. In these terms, an accurate, reliable and safe control of the gas flow is required in order to study the sensor's response. The gas chamber must allow the mixing of different gases: the gas used as a background (synthetic air, nitrogen) and the gas or gases whose concentration are changed, the target gases, and must be hermetic, in order to avoid the leakage to the surrounding environment.

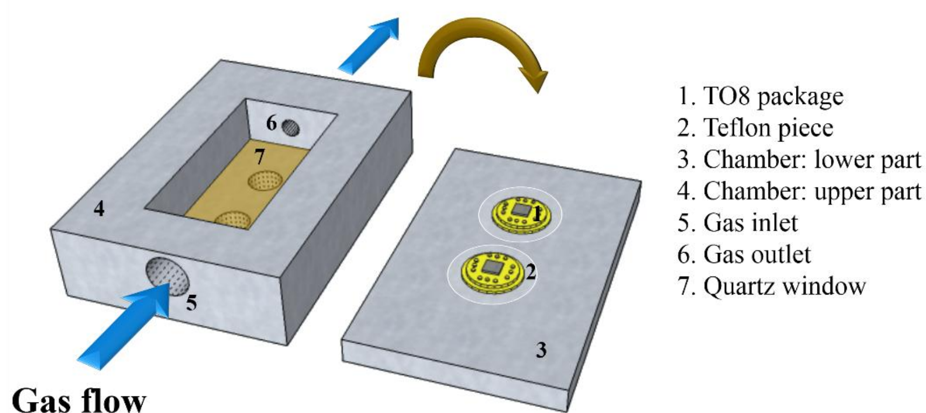

Figure 2.9 Scheme of the two parts of the gas chamber. The stainless steel gas chamber includes a Teflon O-ring seal for a hermetic closure (not shown), and a PCB soldered to the 24 sockets where the two TO-8 packages are inserted.

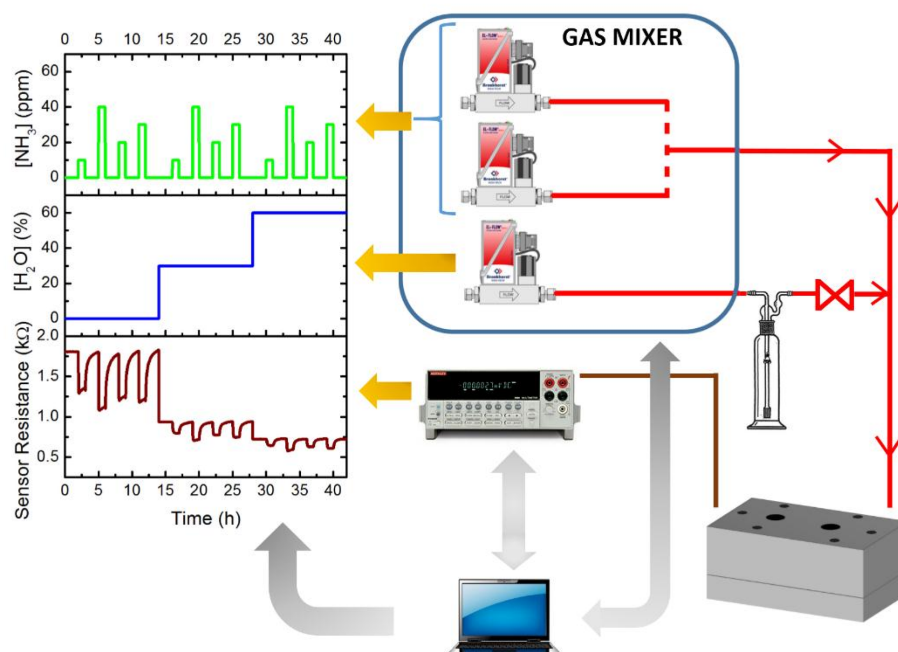

Figure 2.10 Diagram of the setup of the gas station, composed of the gas mixer, bubbler, gas chamber and Keithley SMU unit. A gas line is derived from the gas mixer to add humidity to the final mix by bypassing the background gas through a bubbler. The computer communicates in both directions with the gas mixer and the Keithley instrument to send the orders and to acquire the lecture provided by both instruments.

The stainless steel chamber used for the gas measurements is represented in Figure 2.9, which accomplishes with the mentioned requirements. On the right side of the figure, the lower part of the chamber is represented, on which the TO8 holders containing the chips are mounted. Two TO-8 can be mounted at its inside and accessed at the same time for measurement purposes.

The lower part of the chamber part includes two teflon cylinders with gas-tight feedthrough contacts on which the sockets can be plugged. On the upper part of the chamber (left side) two holes are visible, whose purpose is to allow introducing UV light for light-activated gas measurements, not used in this work. A quartz window is located in the inner part, to seal properly the chamber allowing at the same time the transmission of UV light.

The design of the gas chamber minimizes its internal volume, which is as small as 8.6 ml, and thus, it reduces the time required to renew the gas in the chamber and tubing. A small volume chamber is convenient because the response time of the sensor

is convoluted by the time the chamber needs to be filled up and, thus, it might difficult the extraction of low response times of the sensor [42].

Another important requirement for the gas setup is the control of the temperature and the electrical measurement of the chemiresistive sensors. The electrical measurements are obtained through a printed circuit board (PCB) that is connected below the chamber and soldered to the sockets at which the TO-8 packages are connected to.

The experimental setup used for the gas measurements is represented in Figure 2.10. A Gometrics MGP2 gas mixer with 5 Brooks Mass-Flow Controllers (MFC) has been used to control the gas flow for the sensing measurements. The gas mixer has a specific gas outlet to generate the required relative humidity, which is a different outlet from the other mixing gases. The lecture of the delivered flow is acquired and the setpoint flow is indicated remotely. From this, the different gas concentrations are obtained, and related then to the resistance change of the sensor.

The main part of the gas sensor tests performed in this thesis, have been performed by introducing different pulses of gas that are not ordered by concentration, since an ordered sequence of pulses may hinder a poisoning of the sensor or an abnormal behaviour.

The humidity is added to the chamber by bypassing air through a bubbler that contains deionized water at a well-controlled temperature and delivering back to the gas mixture a controlled proportion of flow saturated with water. The humidity is previously calibrated by mixing different proportion of humidity-added air to the gas flow (keeping a constant total flow), and monitored using a commercial humidity sensor [43].

Finally, a customized Labview software controls the flows provided by the gas mixer together with the electrical measurements, allowing to program a time sequence for the gas measurements in which the change of the electrical parameters can be performed simultaneously.

2.7. References

[1] H.W. Kroto, J.R. Heath, S.C. O'Brien, R.F. Curl, R.E. Smalley, C60: Buckminsterfullerene, Nature. 318 (1985) 162–163. http://dx.doi.org/10.1038/318162a0.

[2] S. Iijima, Helical microtubules of graphitic carbon, Nature. 354 (1991) 56–58. http://dx.doi.org/10.1038/354056a0.

[3] A. Biswas, I.S. Bayer, A.S. Biris, T. Wang, E. Dervishi, F. Faupel, Advances in top-down and bottom-up surface nanofabrication: Techniques, applications & future prospects, Adv. Colloid Interface Sci. 170 (2012) 2–27. doi:10.1016/j.cis.2011.11.001.

[4] A.M. Morales, C.M. Lieber, A Laser Ablation Method for the Synthesis of Crystalline Semiconductor Nanowires, Science (80-.). 279 (1998) 208–211. doi:10.1126/science.279.5348.208.

[5] R.S. Wagner, W.C. Ellis, Vapor-liquid-solid mechanism of single crystal growth, Appl. Phys. Lett. 4 (1964) 89. doi:10.1063/1.1753975.

[6] R. Laocharoensuk, K. Palaniappan, N. a Smith, R.M. Dickerson, D.J. Werder, J.K. Baldwin, et al., Flow-based solution-liquid-solid nanowire synthesis., Nat. Nanotechnol. 8 (2013) 660–666. doi:10.1038/nnano.2013.149.

[7] T. Hanrath, B.A. Korgel, Nucleation and growth of germanium nanowires seeded by organic monolayer-coated gold nanocrystals, J. Am. Chem. Soc. 124 (2002) 1424–1429. doi:10.1021/ja016788i.

[8] D. Routkevitch, T. Bigioni, M. Moskovits, J.M. Xu, Electrochemical Fabrication of CdS Nanowire Arrays in Porous Anodic Aluminum Oxide Templates, J. Phys. Chem. 100 (1996) 14037–14047. doi:10.1021/jp952910m.

[9] D. Li, Y. Wang, Y. Xia, Electrospinning of polymeric and ceramic nanofibers as uniaxially aligned arrays, Nano Lett. 3 (2003) 1167–1171. doi:10.1021/nl0344256.

[10] N.A. Melosh, A. Boukai, F. Diana, B. Gerardot, A. Badolato, P.M. Petroff, et al., Ultrahigh-Density Nanowire Lattices and Circuits, Science (80-.). 300 (2003) 112–115. doi:10.1126/science.1081940.

[11] S. Barth, F. Hernandez-Ramirez, J.D. Holmes, A. Romano-Rodriguez, Synthesis and applications of one-dimensional semiconductors, Prog. Mater. Sci. 55 (2010) 563–627. doi:10.1016/j.pmatsci.2010.02.001.

[12] H. Adhikari, A.F. Marshall, I.A. Goldthorpe, C.E.D. Chidsey, P.C. McIntyre, Metastability of Au−Ge Liquid Nanocatalysts: Ge Vapor–Liquid–Solid Nanowire Growth Far below the Bulk Eutectic Temperature, ACS Nano. 1 (2007) 415–422. doi:10.1021/nn7001486.

[13] H.-J. Choi, Vapor-Liquid-Solid Growth of Semiconductor Nanowires, in: G.-C. Yi (Ed.), Semicond. Nanostructures Optoelectron. Devices Process. Charact. Appl., Springer Berlin Heidelberg, Berlin, Heidelberg, 2012: pp. 1–36. doi:10.1007/978-3-642-22480-5_1.

[14] Y. Wu, Y. Cui, L. Huynh, C.J. Barrelet, D.C. Bell, C.M. Lieber, Controlled Growth and Structure of Molecular-Scale Silicon Nanowires, Nano Lett. 4 (2004) 433–436.

[15] M. Wei, D. Zhi, J.L. MacManus-Driscoll, Self-catalysed growth of zinc oxide nanowires, Nanotechnology. 16 (2005) 1364–1368. doi:10.1088/0957-4484/16/8/064.

[16] L. Schubert, P. Werner, N.D. Zakharov, G. Gerth, F.M. Kolb, L. Long, et al., Silicon nanowhiskers grown on (111) Si substrates by molecular-beam epitaxy, Appl. Phys. Lett. 84 (2004) 4968–4970. doi:10.1063/1.1762701.

[17] H. Jagannathan, M. Deal, Y. Nishi, J. Woodruff, C. Chidsey, P.C. McIntyre, Nature of germanium nanowire heteroepitaxy on silicon substrates, J. Appl. Phys. 100 (2006). doi:http://dx.doi.org/10.1063/1.2219007.

[18] M.S. Dresselhaus, Y.-M. Lin, O. Rabin, M.R. Black, J. Kong, G. Dresselhaus, Nanowires, in: B. Bhushan (Ed.), Springer Handb. Nanotechnol., Springer Berlin Heidelberg, Berlin, Heidelberg, 2010: pp. 119–167. doi:10.1007/978-3-642-02525-9_4.

[19] J.K. Hyun, S. Zhang, L.J. Lauhon, Nanowire Heterostructures, Annu. Rev. Mater. Res. 43 (2013) 451. doi:10.1146/annurev-matsci-071312-121659.

[20] S. Mathur, S. Barth, H. Shen, J.-C. Pyun, U. Werner, Size-Dependent Photoconductance in SnO2 Nanowires, Small. 1 (2005) 713–717. doi:10.1002/smll.200400168.

[21] D.K. Stewart, A.F. Doyle, J.D. Casey Jr., Focused ion beam deposition of new materials: dielectric films for device modification and mask repair, and tantalum films for x-ray mask repair, Proc. SPIE. 2437 (1995) 276–283. doi:10.1117/12.209163.

[22] S. Okayama, M. Komuro, W. Mizutani, H. Tokumoto, M. Okano, K. Shimizu, et al., Observation of microfabricated patterns by scanning tunneling microscopy, J. Vac. Sci. Technol. A. 6 (1988).

[23] I. Utke, S. Moshkalev, P. Russell, Nanofabrication using focused ion and electron beams, Oxford University Press, New York, 2012.

[24] J.M. De Teresa, R. Córdoba, A. Fernández-Pacheco, O. Montero, P. Strichovanec, M.R. Ibarra, Origin of the difference in the resistivity of as-grown focused-ion- and focused-electron-beam-induced Pt nanodeposits, J. Nanomater. 2009 (2009). doi:10.1155/2009/936863.

[25] H. Seiler, Secondary electron emission in the scanning electron microscope, J. Appl. Phys. 54 (1983).

[26] W.F. Van Dorp, C.W. Hagen, A critical literature review of focused electron beam induced deposition, J. Appl. Phys. 104 (2008) 1–42. doi:10.1063/1.2977587.

[27] R.M. Thorman, T.P. Ragesh Kumar, D. Howard Fairbrother, O. Ingólfsson, The role of low-energy electrons in focused electron beam induced deposition: Four case studies of representative precursors, Beilstein J. Nanotechnol. 6 (2015) 1904–1926. doi:10.3762/bjnano.6.194.

[28] P.A. Crozier, J. Tolle, J. Kouvetakis, C. Ritter, Synthesis of uniform GaN quantum dot arrays via electron nanolithography of D 2GaN 3, Appl. Phys. Lett. 84 (2004) 3441–3443. doi:10.1063/1.1736314.

[29] K. Mitsuishi, M. Shimojo, M. Han, K. Furuya, Electron-beam-induced deposition using a subnanometer-sized probe of high-energy electrons, Appl. Phys. Lett. 83 (2003) 2064–2066. doi:10.1063/1.1611274.

[30] I. Utke, P. Hoffmann, J. Melngailis, Gas-assisted focused electron beam and ion beam processing and fabrication, J. Vac. Sci. Technol. B. 26 (2008).

[31] R.M. Langford, T.X. Wang, D. Ozkaya, Reducing the resistivity of electron and ion beam assisted deposited Pt, Microelectron. Eng. 84 (2007) 784–788. doi:10.1016/j.mee.2007.01.055.

[32] A. Fernández-Pacheco, J. De Teresa, R. Córdoba, M. Ibarra, Metal-insulator transition in Pt-C nanowires grown by focused-ion-beam-induced deposition, Phys. Rev. B. 79 (2009) 1–12. doi:10.1103/PhysRevB.79.174204.

[33] M.A. Mohammad, M. Muhammad, S.K. Dew, M. Stpanova, Nanofabrication, Techniques and principles. Chapter 2: Fundamentals of Electron Beam Exposure and Development, Springer-Verlag/Wien, 2012. doi:10.1007/978-3-7091-0424-8.

[34] A.E. Grigorescu, C.W. Hagen, Resists for sub-20-nm electron beam lithography with a focus on HSQ: state of the art, Nanotechnology. 20 (2009) 31. doi:10.1088/0957-4484/20/29/292001.

[35] P. Rai-Choudhury, M.A. McCord, M.J. Rooks, Handbook of microlithography, micromachining, and microfabrication. Chapter 2 E. beam lithography, 1997.

[36] M. Hatzakis, Electron Resists for Microcircuit and Mask Production, J. Electrochem. Soc. . 116 (1969) 1033–1037. doi:10.1149/1.2412145.

[37] T. Takigawa, K. Kawabuchi, M. Yoshimi, Y. Kato, High voltage electron beam lithography, Microelectron. Eng. 1 (1983) 121–142. http://www.sciencedirect.com/science/article/pii/0167931783900254.

[38] S. Roy, K.S. Chandan, MEMS and Nanotechnology for Gas Sensors, CRC Press, 2015.

[39] F. Hernandez-Ramirez, a. Tarancon, O. Casals, E. Pellicer, J. Rodriguez, a. Romano-Rodriguez, et al., Electrical properties of individual tin oxide nanowires contacted to platinum electrodes, Phys. Rev. B. 76 (2007) 85429. doi:10.1103/PhysRevB.76.085429.

[40] J.D. Prades, R. Jimenez-Diaz, F. Hernandez-Ramirez, J. Pan, A. Romano-Rodriguez, S. Mathur, et al., Direct observation of the gas-surface interaction

kinetics in nanowires through pulsed self-heating assisted conductometric measurements, Appl. Phys. Lett. 95 (2009). doi:10.1063/1.3192358.

[41] J.D. Prades, R. Jimenez-Diaz, F. Hernandez-Ramirez, S. Barth, A. Cirera, A. Romano-Rodriguez, et al., Ultralow power consumption gas sensors based on self-heated individual nanowires, Appl. Phys. Lett. 93 (2008). doi:10.1063/1.2988265.

[42] I. Weiss, Y. Mizrahi, E. Raveh, Chamber response time: A neglected issue in gas exchange measurements, Photosynthetica. 47 (2009) 121–124. doi:10.1007/s11099-009-0018-3.

[43] Honeywell HIH-4010 Humidty Sensor, (n.d.).

3. LOCALIZED GROWTH OF SnO_2 AND GE NWS

Abstract

In this chapter, an innovative methodology for the simultaneous localized growth and device integration of inorganic nanostructures on heated micromembranes and microhotplates is demonstrated both for single crystalline tin oxide and germanium nanowires. With this simple CMOS compatible technique, it has been possible to address satisfactory the issues of assembly, transfer and contact formation on the final substrate. The nanowires have been studied by TEM and Raman, showing the same features than those grown using standard CVD methodology.

3.1. Introduction

In the previous chapter, the benefits of 1D nanostructures have been justified for gas sensing applications and some of the growth methods have been briefly reviewed. Vapour Liquid Solid approach, and specifically CVD have been remarked as a versatile technique, due to the variety of the external parameters at which the growth may be performed and the diversity of materials that are synthesized.

Furthermore, one of the issues which has not been addressed is the integration of such highly promising nanostructures to form operative semiconductor devices, which is a challenging issue due to the highly time consuming and non systematic processes. For instance, the preparation of nanostructure-based devices usually includes a post-growth deposition/transfer of the materials from the growth substrates to the appropriate surface for device fabrication. The transfer is typically followed by a contact fabrication procedure, which usually involves several steps and adds complexity to the overall fabrication process.

When using gas sensors, the crystalline structure of the NWs is an important feature for studying the interaction of a well-defined surface with the surrounding molecules and the repeatability of the surface reactions. In this sense, single-crystalline materials allow better control and reproducibility for studying the interactions, which is more difficult when using polycrystalline materials. Single-crystalline nanowires may be grown by different methods, as explained in the previous section. The most common techniques are CVD and, to a lesser extent, MBE processes, which are highly time consuming because of the need of ultra-high vacuum in the case of MBE, and the long time required to heat up the furnace tube, due to the large volume of the growth chamber for CVD. Another important aspect of these techniques is that they have a power consumption in the order of kW in order to reach the growth temperature [1]. The benefits of the CVD approach are that the high vacuum is not required, which reduces the time for pumping, and that it does not require of complex geometries and materials sources. For that reasons, CVD has been the selected method of growth used in this chapter.

Both techniques, CVD and MBE allow the growth at a high scale, for substrates up to 12 inch. Nevertheless, when using nanostructures for sensor applications, which are generally in the micron-scale, a more efficient growth may be achieved by limiting the

growth to the dimensions of the sensing area. The reduction of the heated area for the growth improves significantly three important aspects of the process: the power consumption, the involved time and the consumption of precursor. This is one of the main ideas that motivated the here presented localized growth of nanowires.

Several strategies pointing in the same direction are found in literature, using different approaches and techniques to achieve the site-specific growth, as plasmon-induced local heating [2], resistive-type heating of microhotplates [3,4] or micro-cantilevers [5,6]. The aforementioned procedures overcome the limitations to grow inorganic coatings compatible with CMOS techniques, but the formed device configuration is less desirable in terms of thick interface layers, and interference between growth and characterization circuits. The templated growth of tin dioxide nanowires using pre-grown carbon nanotubes on micro-hotplates is presented in [7], however polycrystalline structures are obtained. An integration of SnO_2 nanowire bundles in gas sensors was also demonstrated by Vomiero *et al.*, which includes post-growth removal of a SiO_2 template and contact deposition [8], thus, being a much more complicated process than the here presented. Another approach deals with the growth of ZnO nanowires from solution on top of micro-membranes [9], but in contrast to our strategy the heating element was only used for functional operation of the device but not for the growth of NWs, as the growth process is carried out at low temperatures, about 90ºC, in a liquid solution where the convection losses are considerably high.

Furthermore, the control of length and the density of the nanowires is not successfully obtained in any of the mentioned works. Such issues have significant influence on the performance of the devices for applications such as gas sensors, although the direct growth on an electronic platform reduces the complexity of the process.

Here we present a novel method based on the site-selective direct growth of inorganic nanowires, illustrated by germanium and tin oxide, on top of CMOS compatible micro-heaters, that resolves the mentioned issues. This innovative approach has not been attempted before, to the best of our knowledge, and is a first step towards fabricating integrated single crystal nanowire-based devices without the need of nanowire transfer or heating of an entire substrate to facilitate 1D nanostructure growth.

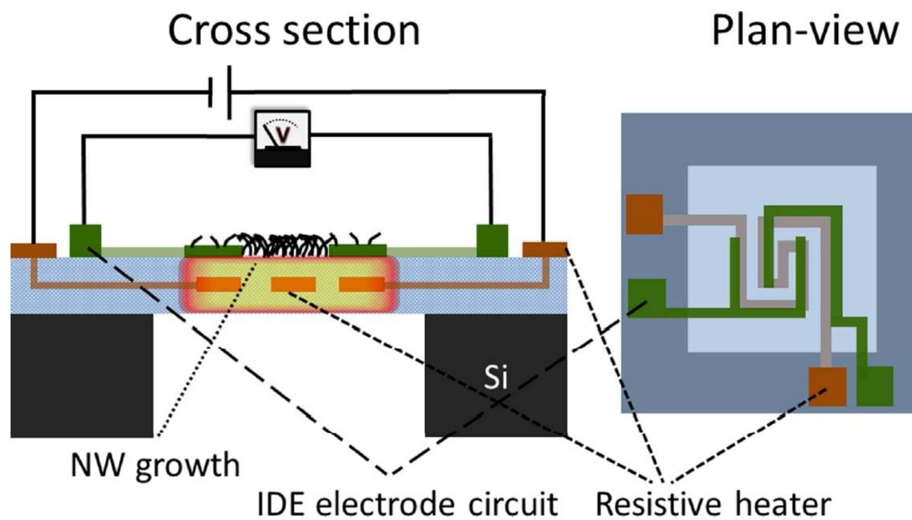

Figure 3.1.Schematic drawing of the micromembrane with integrated buried heater and external circuit containing interdigitated electrodes (IDE). This separate circuit is used to electrically characterize the nanostructure bundle deposited in the illustrated heated area

3.2. Experimental details

Micromembranes and microhotplates with integrated heaters and surface interdigitated electrodes (IDE), operating at low power (<100 mW) were fabricated in combination with IMB-CNM-CSIC, to allow the in-situ growth of NWs. All devices, as explained in chapter 2, had a thin isolating layer about one micrometre thickness (silicon oxide and/or silicon nitride) that contains the buried heating elements and exposed interdigitated Pt electrodes (IDE) on top, which can be used to fabricate electrical contacts that allow to access the inorganic structures. The electrodes from microhotplates allow *in situ* the formation of contacts to the growing nanowire bundles without electrical interference with the heater circuit and, thus, allowing heating and measuring operations to be performed independently (see Figure 3.1). The details of the innovative in-situ growth of nanowires will be described in the following sections.

3.2.1.Calibration of temperature versus heater power in vacuum conditions

The temperature required for the growth of the nanowires is locally provided by the micro-heaters from the micromembranes or the suspended microhotplates. The temperature is dependent on the electrical power dissipated by the heater. On large

heaters, the temperature may be obtained by using a thermocouple or other temperature sensors; nevertheless, when using micro-sized heaters, the temperature measurement becomes more difficult, due to the difficulties in introducing a temperature sensor into the chamber on top of the microstructure because of size and fragility of the micro-devices.

Furthermore, the temperature calibration of the microhotplates is typically carried out at atmospheric pressure and differs from vacuum conditions due to the reduced heat exchange by convection with the surrounding atmosphere and, thus, cannot be directly used for the here-proposed growth method.

A first estimation of the temperature rise provided by the electrical power delivered to the heater when operating at low vacuum conditions, simulating the real growth conditions, was carried out employing a commercial microhotplate with an integrated temperature sensor.

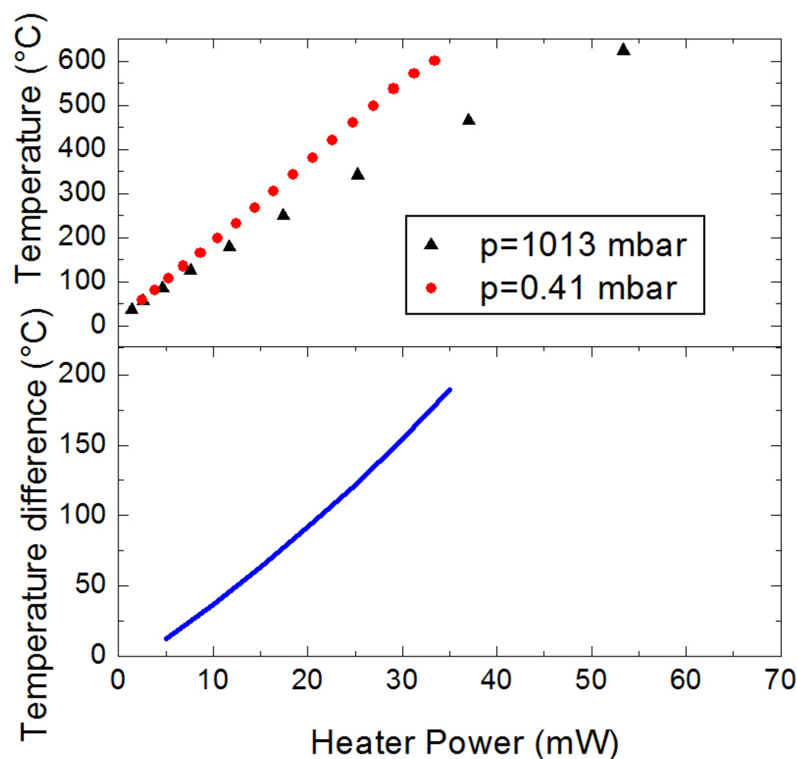

Figure 3.2. (Top) Temperature as a function of the power supplied to the heater of CCMOS microhotplate at atmospheric pressure and in low vacuum conditions (0.41 mbar). (Bottom) Difference between the temperature in atmospheric conditions referenced to vacuum conditions as a function of the electric power consumption of the heater.

CSS4_16A chips from Cambridge CMOS Sensors (CCMOS) [10] were used for this purpose, because a buried diode temperature sensor is incorporated in the microhotplate. A constant pressure of 0.4 mbar was kept by connecting a mechanical vacuum pump to the same gas chamber employed for the gas measurements.

The temperature provided by the heater as a function of the power supplied is represented in Figure 3.2 a). As expected, for the same supplied electrical power, higher temperatures are achieved in vacuum conditions, with a maximum absolute difference of 190°C compared to atmospheric conditions, as shown in Figure 3.2 b). One has to bear in mind that the maximum temperature measured by the diode is 600ºC, therefore above this value the temperature of the device can only be estimated.

The mentioned experiments allow to estimate the change in electrical power needed to heat the membranes up to the right temperature for the growth of the NWs in vacuum conditions. The pressure during this calibration is one order of magnitude higher than the one used for the growth procedure. For a first estimate, a similar curve as before was supposed as initial calibration, assuming that the difference in pressure from 10^{-1} to 10^{-2} mbar weakly affects the heat dissipated by convection. For practical purposes and, especially, for the higher temperature regimes, above 600 ºC, for which no microhotplates with temperature sensor were available, the temperature was estimated from the resistance value of the Pt or polysilicon heater.

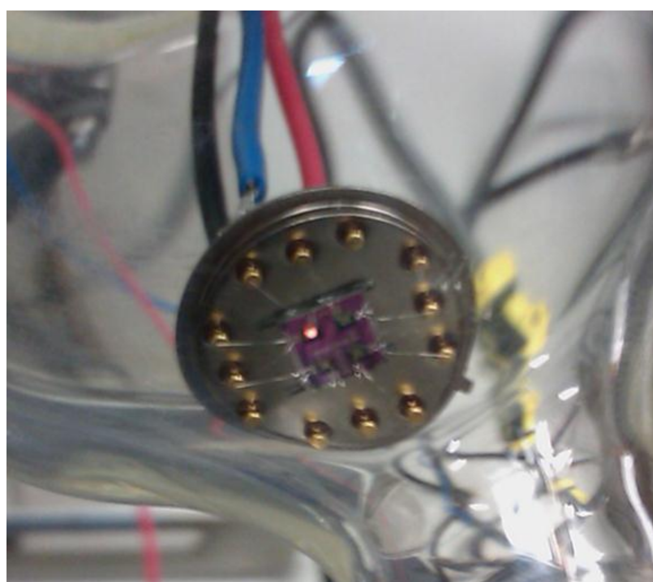

Figure 3.3. Optical image of the micromembranes on the TO-8 holder within the quartz chamber during the growth of the SnO_2 NWs. The red radiation emitted of the micromembrane is observed, due to the high operating temperature (750 °C).

It has to be mentioned that at temperatures above 600-700 °C the heaters start to dissipate an important amount of heat by radiation, which is visible through the red colour that the microstructure acquires in this regime, during the growth of SnO_2 NWs (see Figure 3.3). The increase in emission of thermal radiation at these temperatures takes place independently of the surrounding gas pressure, as known from the Stefan-Boltzmann equation.

3.2.2.Growth process

The fabrication process is based on the VLS method, using a CVD-like technique on a localized area on micromembranes and microhotplates. On this initial approach, a thin non-continuous Au film (nominal thickness 1-1.5 nm) is sputter-deposited over the entire chip and, consequently, does not give rise to electrical conduction through it. The Au layer, when heated to the appropriate temperature, will act as a catalyst and nucleation site of the stimulated growth. The chip is mounted on a TO-8 holder, at which the pads are bond to, and introduced into a glass reactor. In the glass chamber electrical feedthroughs have been fabricated, which allow the pins of the TO-8 holder to be electrically accessed.

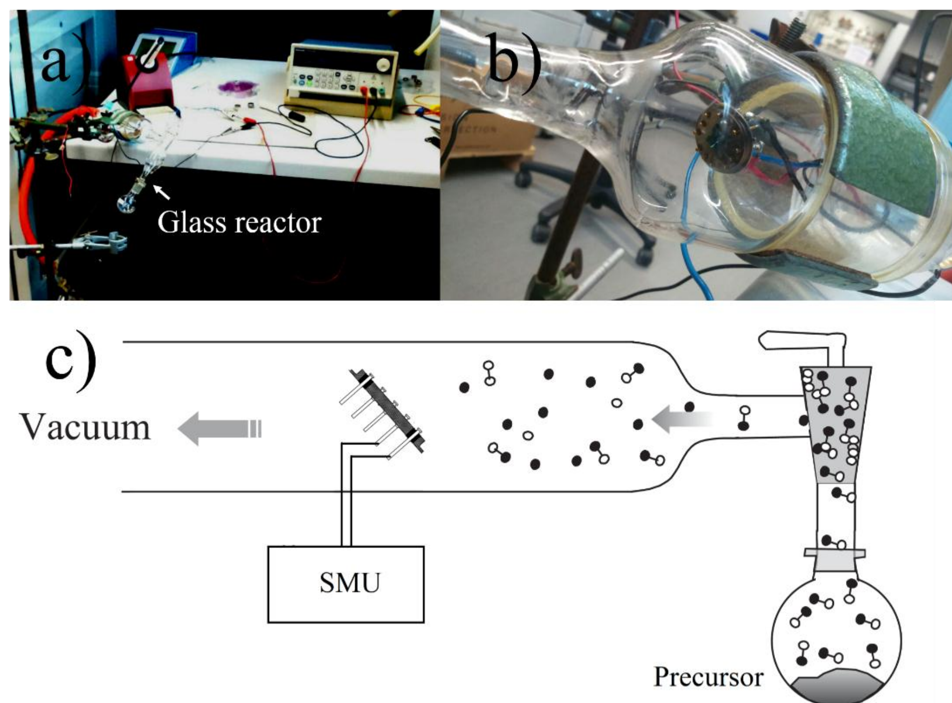

Figure 3.4. Experimental setup used for the localized growth of the nanowires on top of micromembranes and microhotplates.

A picture of the experimental setup for the localized growth is observed in Figure 3.4 a), where the glass reactor and electrical source can be observed. Figure 3.4 b) shows the TO-8 holder with the electrical connections once it is prepared for the growth.

The glass chamber, a cold-wall low pressure glass CVD reactor, with a volume of 25 ml is connected to a vacuum pump and once the right vacuum level is reached, the substrate is heated up to the appropriate temperature for the growth of nanowires by adequately biasing the micro-heater, giving rise to the formation of the liquid Au nanoclusters. Next the valve that separates the growing chamber and the glass flask that contains the liquid or solid precursor which already started to evaporate, is opened and the vapour flows on top of the micro-device, what initiates and catalyses the decomposition of gas precursor on the Au droplets, since the process is more favourable energetically in presence of the metal liquid phase. The complete diagram of the setup, where all the parts are illustrated is found in Figure 3.4 c). As it may be observed, the TO-8 is faced towards the inlet of the gas precursor.

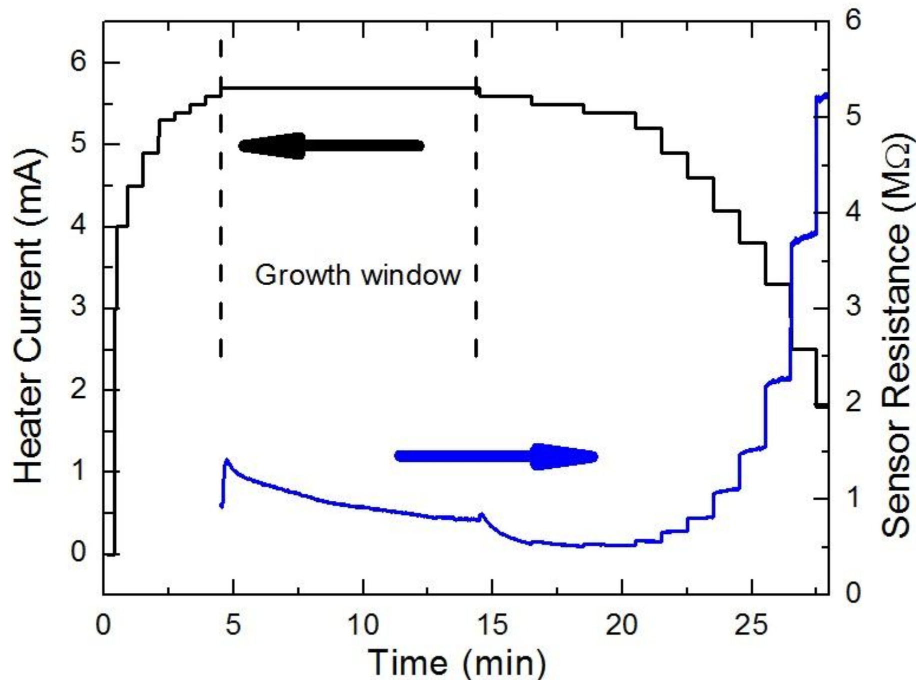

Figure 3.5. Representation of the electrical measurements performed during the localized growth of SnO_2 NWs. The heater current (black line) is increased quickly and then decreased. The resistance of the NWs is measured once the growth temperature is achieved (blue line).

The molecular sources for the Ge or SnO_2 nanowire growth are liquid Diphenylgermane ($H_2Ge(C_6H_5)$) (50 mg) or solid $Sn(OtBu)_4$ (50 mg) respectively, which were kept at room temperature (25 °C) during the process. Nanowire growth was achieved by employing a vacuum of around $4 \cdot 10^{-2}$ mbar that allows the sublimation or evaporation of the molecular source for SnO_2 and Ge NWs, respectively.

The respective micro-devices were heated to the appropriate temperature (400-420 °C for Ge; 700-750 °C for SnO_2). As mentioned before, thermal decomposition of the vaporized precursor species allows the growth of nanowires only at the heated micromembranes or microhotplates. The growth duration was in the range for 2-10 minutes depending on the desired length of the nanowires.

An additional advantage of the here-presented set-up is the possibility to use the top electrodes to follow the growth process by monitoring the electrical resistance between them. The electrical measurements obtained during a standard experiment for the localized growth of SnO_2 NWs are represented in Figure 3.5. A constant current operation mode was employed to carry out the heating experiments, while the voltage drop was measured continuously. The process starts with a heating up ramp that lasts 5 min, which is used to reach the right growth temperature. Next, the power is kept constant for 10 minutes to allow the gas precursor to enter the chamber and the growth to take place, and finally the cooling down process takes 13 minutes. The black line in the figure represents the applied current of the heater, which is rapidly increased until the growth temperature is reached. The cooling down ramp is considerably longer in order to avoid the damaging of the heater, as the first experiments showed that many heaters were broken due to the thermal stresses induced by fast temperature changes.

The blue line, on the other hand, represents the resistance measured during the NWs growth, starting to be measured when the growth temperature is reached. Once the growth is finished, the temperature is reduced, and the resistance of the NWs follow the typical semiconducting temperature behavior, i.e., the resistance increases when temperature is reduced, which is more visible at the last part.

An advantage of this approach is the ability to check if the growth process is adequately performed and to stop the growth at a well-defined resistance value. During the growth experiments, the heaters were controlled by a Keithley 2602 Source-Measuring Unit connected to a computer operating with Labview software. The

electrical power was in the range of 3 mW for the 100x100 µm^2 microhotplates heated to 400 °C, for Ge NWs growth and of 48 mW for 700 °C in the case of micromembranes (SnO_2 NWs). By coincidence, this latter power is exactly the same used to bring the gas sensor device to a suitable operating temperature of 260 ºC when performing the gas sensing experiments. As commented before, this strong difference in temperature is related to the important heat dissipation in atmospheric pressure due to convection effects.

3.2.3. Experimental instrumentation

The morphology of 1D nanostructures on top of the micromembranes and microhotplates was analyzed using a FEI Inspect F50 scanning electron microscope (SEM). The nanowires were deposited on lacey carbon and carbon film copper grids for TEM characterization (Alfa Aesar). In this study, we used a FEI TECNAI F20 equipped with an EDX detector. Raman measurements were performed on a Jobin Yvon LabRam HR800 using laser excitation wavelength of 325 nm. An objective lens of 40X at room temperature was used for obtaining the Raman scattering signal, in order to maximize the signal from the NWs when grown on top of micromembranes. Lorentzian functions were used to fit the experimental Raman spectra.

3.3. Results and discussion

3.3.1. Growth of SnO_2 nanowires

SnO_2 are grown on closed micromembranes, which have been described in section 2.5. Higher temperatures can be obtained using this type of substrates than using microhotplates, due to their higher robustness, which is a consequence of their design and fabrication process.

A low magnification SEM image of a micromembrane with SnO_2 NWs site-selectively grown, is presented in Figure 3.6 a). The image shows that the surface area is completely covered by tin oxide nanowires, being the nanowire density homogeneous in the centre of the locally heated deposition area. The lighter area in this figure denotes

the area where the growth of the nanostructures has taken place, which follows the temperature profile provided by the heater.

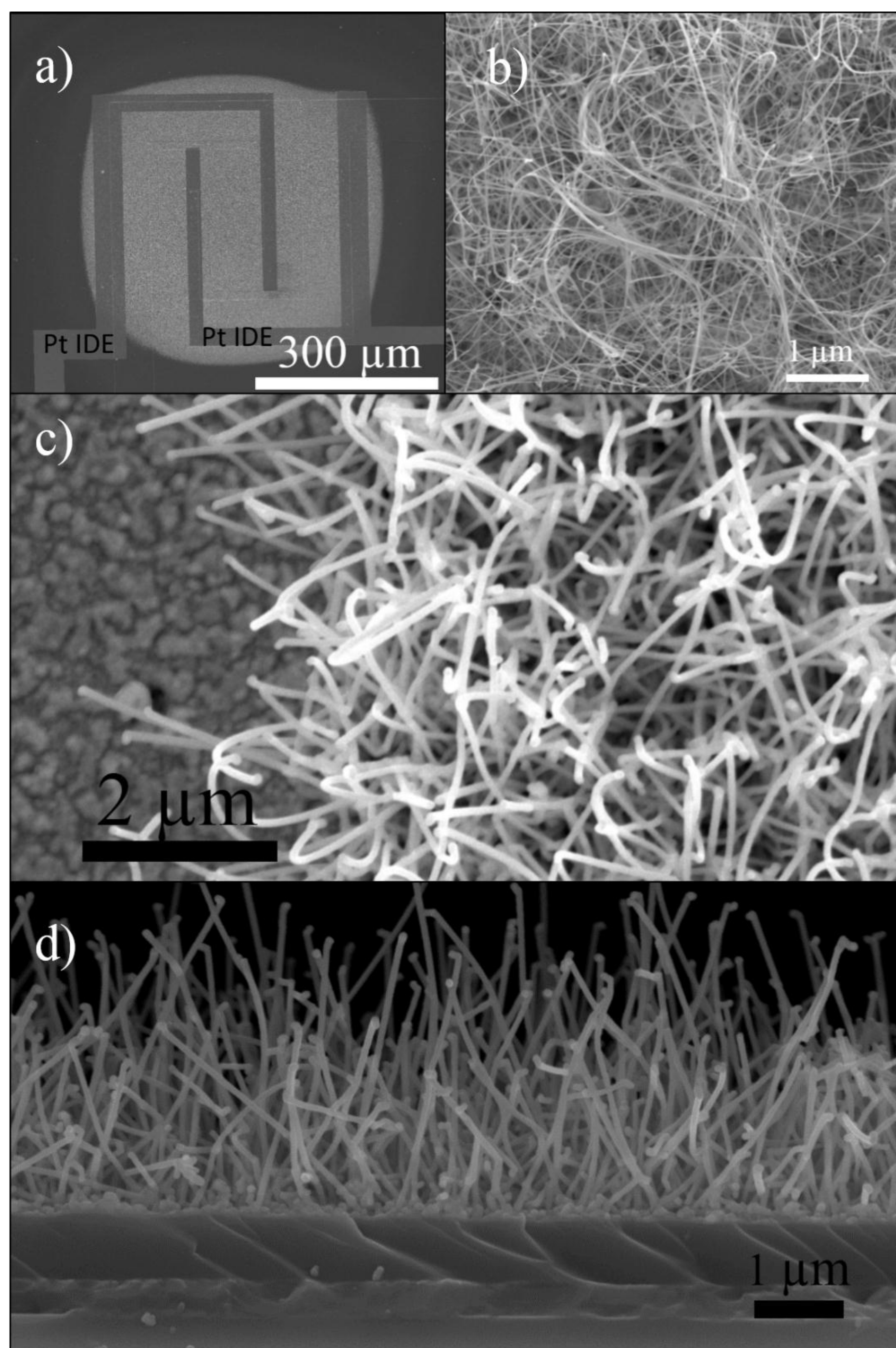

Figure 3.6 SEM image of a) micromembrane and the shape of the heater. The lighter part corresponds to the regions where the NWs are grown; b) Image with high density SnO_2 NWs onto the membrane; c) Detail of the NWs contacting the electrode; d) Cross-section of SnO_2 NWs-based sensor. A very thin layer is observed below the NWs of a thickness between 30-80 nm.

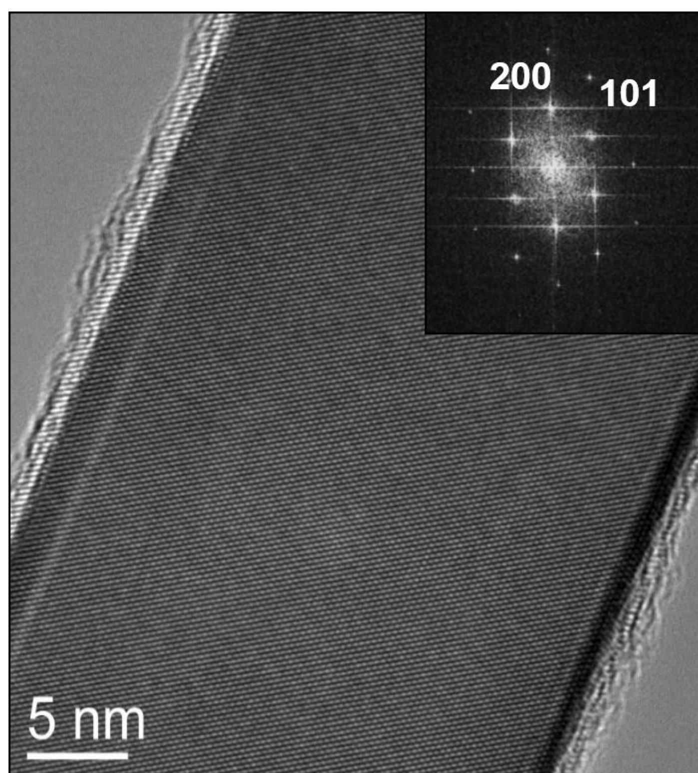

Figure 3.7 HRTEM image of a monocrystalline SnO_2 NW that crystallizes in rutile phase. Inlet FFT illustrates the [101] predominant growth direction

Higher magnification SEM pictures of NWs are shown in Figure 3.6 b) and c), where the high density of grown NWs is shown. The latter figure shows the nanowires nearby the Pt electrode, on top of which no NWs are found. A possible explanation could be that a Pt/Au alloy has formed during the heating step that did not acted as a catalyst for nanowires growth, probably because the alloy reduces the catalytic efficiency. The image also demonstrates the contact of the NW with the electrodes, justifying that the network of nanowires can be electrically measured.

Locally grown SnO_2 nanowires are monocrystalline, with tetragonal (rutile) phase, with predominant [101] growth direction of the tetragonal (rutile) phase, as shown by High Resolution Transmission Electron Microscopy (HRTEM) and the respective fast Fourier transformation (FFT) pattern (see Figure 3.7 and inset imatge). The average SnO_2 nanowires are of the same quality as described elsewhere for large area growth [11].

A cross-section SEM image of SnO_2 NWs on top of a micromembrane, with slightly shorter nanowires, is shown in Figure 3.6 c). On the bottom of the image, the 300 nm thick Si_3N_4 layer and the upper SiO_2 (800 nm) film are observed. The heater from the

microhotplates is not observed in the image. A high density of NWs is found with a length between 2 and 5 µm, and the contact between the network of NWs can also be observed.

Besides, a very thin layer is observed between the nanowires and the SiO_2 layer. This corresponds to the two-dimensional growth of SnO_2, which occurs simultaneously during the synthesis of the nanowires, but with a much lower growth rate, and leads to a thin layer of nanocrystalline SnO_2 because it is a non-catalysed process. The thickness of this layer is between 30 and 80 nm; the layer roughness observed is due to the base of nanowires that remained after the sample preparation. Our estimations from similar samples grown in a conventional furnace indicate that the conductivity in this layer is orders of magnitude lower than that provided by the NW network.

Thus, monocrystalline tin dioxide nanowires have been locally grown on top of micromembranes, forming a network that ensures the electrical contact between them and to the Pt electrodes from the micromembrane, being able to be studied as a gas sensor. This part will be presented in chapter 4.

3.3.2.Growth of Ge nanowires

A microhotplate after the Ge NW growth process is shown in Figure 3.8 a). In the central part of the microhotplate uniform monocrystalline Ge nanowire growth has been achieved, which extends also to parts of the suspending arms because of the still high enough temperature to allow the precursor thermolysis (see arrows in the figure). Moving away from the microhotplate with the embedded heater, the arms are cooling down and at a certain distance from the microhotplate the temperature is not enough to allow the thermolysis of the precursor and, thus, the nanowire growth does not take place. The uniformly grown nanowires are localized preferentially on top of the silicon dioxide layer, between the contacts, since, as explained before, the formation of a Pt-Au eutectic alloy might prevent the presence of Au seeds required for the growth. This depends on the thickness ratio of the Au-to-Pt layers, as for thicker Au layers, NW growth on top of the electrodes has been achieved.

The grown NWs are not aligned and, thus, are interconnected as a mesh, as can be observed in the higher magnification SEM image from Figure 3.8 b). The electrode is observed in Figure 3.8 c), from it it can be seen that the nanowires are connected to.

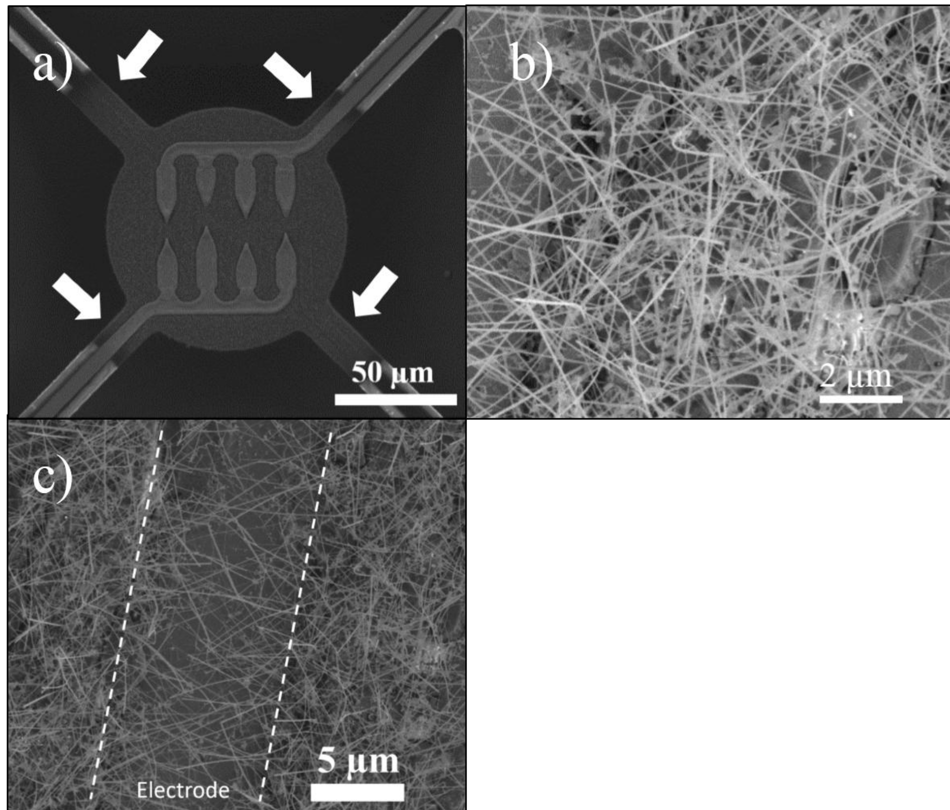

Figure 3.8 a) SEM image of one of the microhotplates after the growth process, which occurred at the center and also on part of the arms closer to the microhotplate (see arrows), while further away, the temperature was not high enough to allow thermolysis; b) High magnification image with high density of Ge NWs; c) SEM image shows the homogeneous growth of Ge NWs on micro-membranes at 400 °C illustrating that on top of the electrodes the NW growth is hampered.

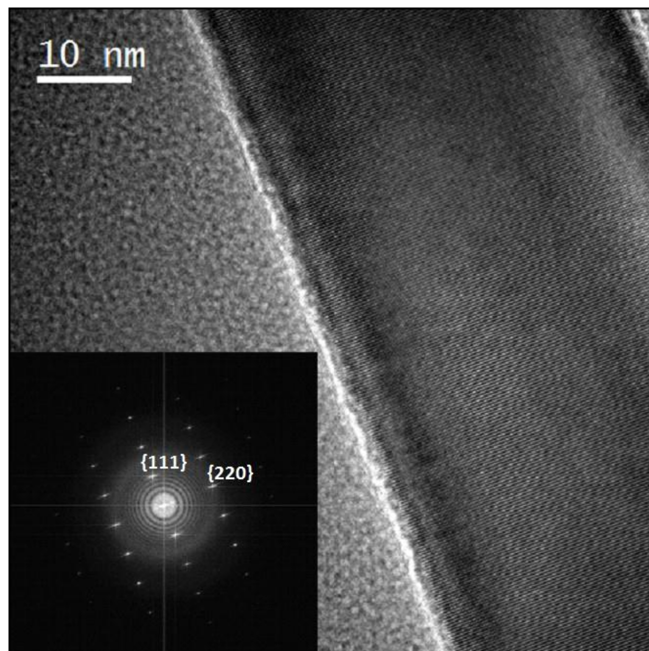

Figure 3.9 HRTEM image of [111]-oriented Ge nanowire grow on a micromembrane illustrating the excellent crystal quality of the germanium nanowire, which is also reflected in the sharp FFT.

The grwon nanowires showed low tendency of tapering, in contrast to Ge nanowires grown using microcantilevers as local heating source [12]. As a function of the growth time, nanowires with lengths in excess of 10 µm are achieved through this method.

(HRTEM) analysis confirms monocrystalline germanium nanowires, which grow predominately along the <111> direction of the cubic crystalline structure, surrounded by a very thin amorphous GeO_x layer of around 1 nm (Figure 3.9)). Both results are in agreement with values reported in other works found in literature [13,14].

As in the case of SnO_2, the localized growth of Ge NWs by VLS method has shown to provide monocrystalline nanostructures, in form of a network that readily after the growth may be used as a gas sensor.

3.3.3.Raman spectroscopy characterization of SnO_2 NWs

Raman scattering studies have been performed on SnO_2 network of nanowires grown by two different methods: i) the locally grown NWs on micromembranes, have been compared to the Raman spectrum of ii) SnO_2 NWs grown on a Si/SiO_2 substrate grown in a cold-wall quartz reactor in which a high-frequency field where the substrate is placed on a graphite susceptor [11]. The latter is the same approach followed for the growth of individual NWs contacted by EBL, which is detailed in the section 2.2.2.2.

The Raman active modes from both samples have been characterized in order to compare the crystalline quality and study the similarities between the structures grown by the two methods. The NWs from both samples have been grown at similar temperature, and the diameter of the NWs is in the same range (around 100 nm). The NWs on top of Si substrate, are however, longer than the locally grown.

The Raman studies have been obtained using an ultraviolet laser, with an excitation wavelength of 325 nm. Visible wavelengths (λ=532 nm) leads to a very low Raman signal due to the non-efficient scattering for this excitation line due to the very low absorption of subbandgap radiation. The measured Raman shift ranges between 350 and 900 cm^{-1}, where the SnO_2 features should be observed. Concerning the locally grown NWs, the Raman signal has been obtained with the NWs on top of the micromembrane.

Different Raman spectra obtained for NWs grown by standard CVD procedure are represented in Figure 3.10 a). The most intense peak, observed at 627 cm^{-1}, corresponds

to the A_{1g} mode of SnO_2 [15]. As can be seen, the Si peak, located at 520 cm^{-1}, is not observed, due to the high density of NWs that provides a high interaction volume which absorbs almost all the incident radiation and that does not allow to see the contribution from the Si substrate. The next Raman peaks, according to their intensity, are found at 472 and 768 cm^{-1}, which are associated to the E_g and B_{2g} vibration modes, respectively, that, together with A_{1g}, are the classic vibration modes of SnO_2 [15]. B_{1g} is also considered a classical mode, which corresponds to a wavenumber of 100 cm^{-1}, out of the measurement range of this study. These peaks correspond to those in other works but with a small blue shift of around 5 cm^{-1} [15-17].

The Raman scattering processes occurring in SnO_2 nanowires synthesized on top of micromembranes are presented in Figure 3.10 b). Similar to the NWs grown on Si substrate, the most intense peak is the one found at 627 cm^{-1}, again, associated to the A_{1g} mode. In this sample, a strong difference is evident because the second most intense peak is found at a Raman shift of 518 cm^{-1}. This peak does not correspond to any known transition in SnO_2 but, rather, can be assigned to the phosphorous-doped poly-Si heater. The Raman scattering peak of single-crystalline Si is known to be at 520 cm^{-1}, but that of polycrystalline Si appears at a lower wavenumber [18].

The third and fourth most intense peaks are found at 472 and 768 cm^{-1}, the E_g and B_{2g} vibrational modes, respectively. These are the same peaks observed in the Raman spectrum of locally grown SnO_2 NWs and with the same order of intensity.

Both experimentally obtained spectra have been fitted using the addition of lorentzian functions. The centre of the different lorentzian functions obtained from both samples are summarized in Table 3.1, and related to the vibrational modes of the SnO_2 crystalline lattice, when possible, or tentatively assigned to plausible contributions. Several similarities can be found from this analysis: the E_g, A_{2u} TO (transversal optical phonon), A_{1g}, A_{2u} LO (longitudinal phonon) and B_{2g} modes from SnO_2 are found at very similar wavenumber values (3 cm^{-1} maximum difference is obtained).

The mentioned peaks for both samples are in good agreement with those of the rutile structure of SnO_2, confirming that SnO_2 NWs possess the same crystalline structure observed by TEM.

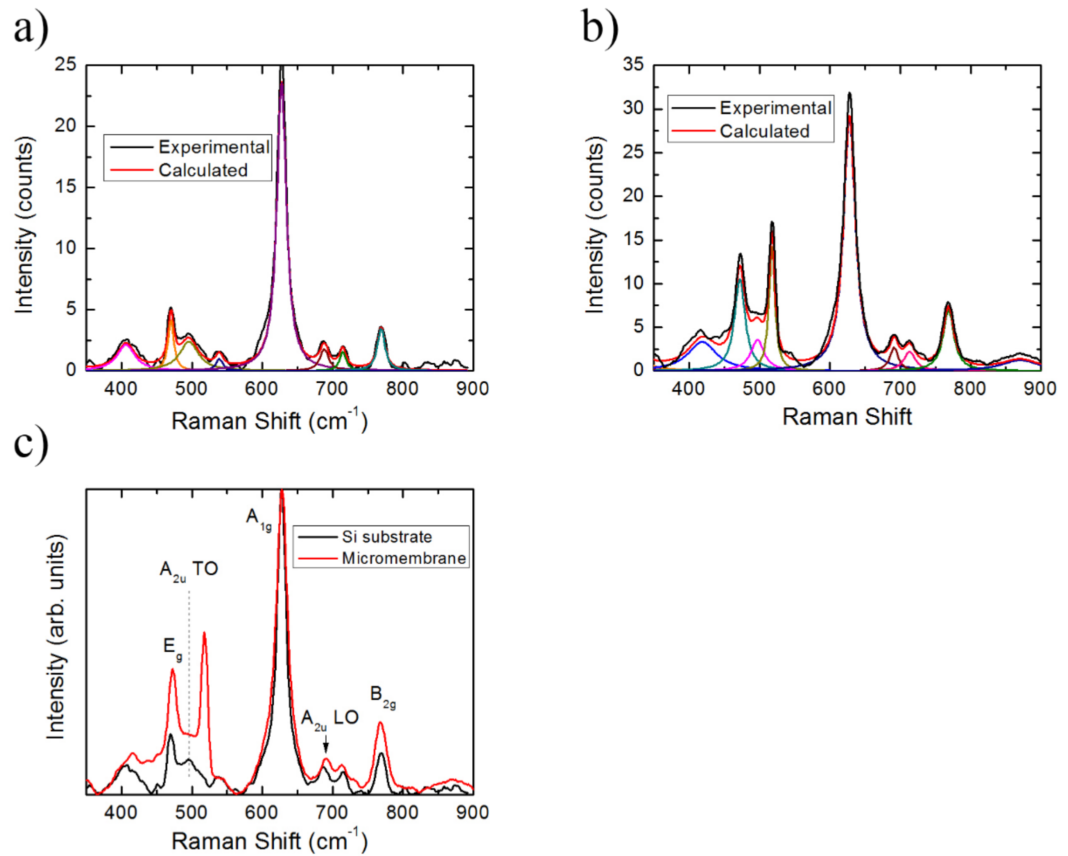

Figure 3.10 a) Raman spectra from SnO_2 NWs grown on Si/SiO_2 substrate in a CVD quartz furnace. The spectra are calculated and experimentally obtained; b) Raman spectra from SnO_2 NWs grown on top of micromembranes, experimental and also the fittings are plotted; c) Normalized Raman spectra from both samples to compare the peak features. Both show very similar characteristics.

Table 3.1. Wavenumber of the different peaks from the decomposed Raman spectra of SnO_2 NWs grown on Si substrate and locally grown on top of a micromembrane. The peaks are related to the vibrational modes.

Vibrational Mode	**Raman Shift (cm^{-1})**	
	Si Substrate	Micromembrane
unknown	407	414
E_g SnO_2 [15,16]	470	472
A_{2u} IR active TO SnO_2 [19]	496	498
P-doped poly-Si [18]		518
	539	
A_{1g} SnO_2 [15,16]	627	627
A_{2u} IR active LO SnO_2 [15,16]	688	691
unknown	715	714
B_{2g} SnO_2 [15,16]	769	769

Two IR-active Raman peaks related to SnO_2 are found in both samples, namely the A_{2u} TO and A_{2u} LO modes. Note that the intensity observed on these modes is much lower than the observed one corresponding to the classical modes. These are Raman forbidden modes that may become weakly active when structural changes induced by disorder and size effects take place [19].

In an infinite crystal only the phonons that are near the centre of the Brillouin zone may contribute to the scattering of the incident photons as a result of the momentum conservation rule between phonos and incident light. However, when the dimensions of the structure or the crystal are reduced to the nanoscale, the k=0 rule selection for the elastic scattering of phonons is relaxed progressively, allowing phonons with $k \neq 0$ to contribute to the Raman spectrum [16]. Size effects appear when the grain size or the nanostructures have dimensions below about 20 nm [15]. When the crystallite is in the nanoscale, the phonon scattering is not limited to the centre of the Brillouin zone, and thus, the phonon dispersion near the centre must be considered. Therefore, symmetry-forbidden modes are observed, in addition of shift and broadening of first-order optical phonon.

TEM measurements, shown in Figure 3.7, prove that the grown material is composed of single-crystalline SnO_2 nanowires, and SEM images ensure that, the nanowires present on top of the membrane have a diameter higher than 80 nm. Thus, crystalline grains of several nanometres of diameter from the NW are discarded as the origin of the assigned IR-active modes. One plausible explanation would come from some thinner nanowires could contribute to the signal. A second plausible explanation comes from the buffer layer under the NWs. The growth of this film, even if the growth conditions are selected to minimize its appearance, is inherent to the 3D non-catalysed growth and cannot be avoided. This film may contain nanocrystalline grains of small size that could give rise to the observed IR modes.

Other features found in both spectra are the band centred at 407-414 cm^{-1} and another peak at 714 cm^{-1}. The first feature appears as a band, more than a peak, due to the large full width half maximum (FWHM) of the peak that is not consistent with values expected for crystalline materials. The second peak can be fitted by a lorentzian shape with a FWHM in better agreement with reported values for crystalline materials.

The origin of both features is unclear, as no Raman peaks from SnO_2, Si or SiO_2 are found at these wavenumbers.

Therefore, very similar features have been found on both spectra from SnO_2 NWs locally or non-locally grown: the same vibrational modes related to rutile SnO_2 are found, and with similar intensity profile. Furthermore, the peaks that show the higher intensity are exactly the same on both structure, and additionally, the same IR active modes are observed on both spectra. Consequently, the Raman study proves that the here presented in-situ growth of SnO_2 NWs gives rise to very similar structure to the grown NWs on a standard CVD process, i.e., the resulting nanostructures obtained by the novel site-specific growth are very similar to those grown by the standard CVD process.

3.4. Conclusions

A CMOS compatible localized CVD growth of inorganic nanowires using microsized platforms with integrated heaters and surface electrodes for the electrical integration of the nanowire bundles has been demonstrated. This approach represents a simple, scalable and cost effective strategy for nanowire integration, which is a fast and low power consuming process. The growth conditions were optimized for specific inorganic material classes including classical group (IV) semiconductors, such as Ge, and functional oxides, illustrated by the controlled formation of SnO_2. The structural characterization of the in-situ grown NWs has shown very similar features to those synthesized by a standard CVD process.

The novel method for site-specific growth of NWs gives rise to their effective confinement in the heated area. The nanowires create a path to cover the gap between the IDEs through multiple NW contacts. Since the resulting structure is already a fully finalised device, requiring no further fabrication step after the growth, it can be used for electrical measurements or, in our case, for gas sensing applications. The in-depth analysis of the gas sensing properties of these devices will be explained in Chapter 4 for the network of SnO_2, giving a detailed analysis of the sensing mechanism towards ammonia, and presenting briefly other measurements. Chapter 5 presents the sensing properties of Ge NWs towards different gases, as first measurements done with this nanostructured material.

Furthermore, the here proposed strategy can be applied to other 1D materials as long as there is a low temperature precursor available and the decomposition temperature lies within the reachable temperatures of the microhotplates and micromembranes. An extension of this work could be the selective deposition of the catalytic metal at the surface of the chips or wafers to avoid the contamination of the surface of the chips with Au. This process could be carried out during the fabrication of the microhotplates, as most of the employed catalytic metals are routinely used in microfabrication.

3.5. References

[1] http://www.planartech.com/cvd-systems.html, (n.d.).

[2] L. Cao, D.N. Barsic, A.R. Guichard, M.L. Brongersma, Plasmon-Assisted Local Temperature Control to Pattern Individual Semiconductor Nanowires and Carbon Nanotubes, Nano Lett. 7 (2007) 3523–3527. doi:10.1021/nl0722370.

[3] J.S. Suehle, R.E. Cavicchi, M. Gaitan, S. Semancik, Tin oxide gas sensor fabricated using CMOS micro-hotplates and in-situ processing, IEEE Electron Device Lett. 14 (1993) 118–120. doi:10.1109/55.215130.

[4] R.E. Cavicchi, S. Semancik, F. DiMeo, C.J. Taylor, Use of Microhotplates in the Controlled Growth and Characterization of Metal Oxides for Chemical Sensing, J. Electroceramics. 9 (2002) 155–164. doi:10.1023/A:1023224123925.

[5] D.C. Lee, T. Hanrath, B.A. Korgel, The Role of Precursor-Decomposition Kinetics in Silicon-Nanowire Synthesis in Organic Solvents, Angew. Chemie Int. Ed. 44 (2005) 3573–3577. doi:10.1002/anie.200463001.

[6] J. Lee, T. Beechem, T.L. Wright, B.A. Nelson, S. Graham, W.P. King, Electrical, Thermal, and Mechanical Characterization of Silicon Microcantilever Heaters, J. Microelectromechanical Syst. 15 (2006) 1644–1655. doi:10.1109/JMEMS.2006.886020.

[7] P. Parthangal, R.E. Cavicchi, D.C. Meier, A. Herzing, M.R. Zachariah, Direct synthesis of tin oxide nanotubes on microhotplates using carbon nanotubes as templates, J. Mater. Res. 26 (2011) 430–436. doi:10.1557/jmr.2010.27.

[8] A. Vomiero, A. Ponzoni, E. Comini, M. Ferroni, G. Faglia, G. Sberveglieri, Direct integration of metal oxide nanowires into an effective gas sensing device, Nanotechnology. 21 (2010) 145502. http://stacks.iop.org/0957-4484/21/i=14/a=145502.

[9] S.Z. Ali, S. Santra, I. Haneef, C. Schwandt, R. V Kumar, W.I. Milne, et al., Nanowire hydrogen gas sensor employing CMOS micro-hotplate, in: Sensors, 2009 IEEE, 2009: pp. 114–117. doi:10.1109/ICSENS.2009.5398224.

[10] CCS4_16A Datasheet, Cambridge CMOS Sensors Ltd, (n.d.).

[11] S. Mathur, S. Barth, Molecule-Based Chemical Vapor Growth of Aligned SnO2 Nanowires and Branched SnO2/V2O5 Heterostructures, Small. 3 (2007) 2070–2075. doi:10.1002/smll.200700213.

[12] C.J. Redcay, O. Englander, Germanium nanowire synthesis using a localized heat source and a comparison to synthesis in a uniform temperature environment, J. Mater. Res. 26 (2011) 2215–2223. doi:10.1557/jmr.2011.181.

[13] S. Barth, M.M. Koleśnik, K. Donegan, V. Krstić, J.D. Holmes, Diameter-controlled solid-phase seeding of germanium nanowires: Structural characterization and electrical transport properties, Chem. Mater. 23 (2011) 3335–3340. doi:10.1021/cm200646e.

[14] P. Nguyen, H.T. Ng, M. Meyyappan, Growth of individual vertical germanium nanowires, Adv. Mater. 17 (2005) 549–553. doi:10.1002/adma.200400908.

[15] A. Diéguez, A. Romano-Rodríguez, A. Vilà, J.R. Morante, The complete Raman spectrum of nanometric SnO 2 particles, 90 (2001) 1550–1557. doi:10.1063/1.1385573.

[16] S.H. Sun, G.W. Meng, G.X. Zhang, T. Gao, B.Y. Geng, L.D. Zhang, et al., Raman scattering study of rutile SnO2 nanobelts synthesized by thermal evaporation of Sn powders, Chem. Phys. Lett. 376 (2003) 103–107. doi:10.1016/S0009-2614(03)00965-5.

[17] T. Lan, C.W. Li, B. Fultz, Phonon anharmonicity of rutile SnO2 studied by Raman spectrometry and first principles calculations of the kinematics of phonon-phonon interactions, Phys. Rev. B - Condens. Matter Mater. Phys. 86 (2012) 1–7. doi:10.1103/PhysRevB.86.134302.

[18] N. Nickel, P. Lengsfeld, I. Sieber, Raman spectroscopy of heavily doped polycrystalline silicon thin films, Phys. Rev. B. 61 (2000) 15558–15561. doi:10.1103/PhysRevB.61.15558.

[19] L. Abello, B. Bochu, a Gaskov, S. Koudryavtseva, G. Lucazeau, M. Roumyantseva, Structural Characterization of Nanocrystalline SnO 2 by X-Ray and Raman Spectroscopy, 85 (1998) 78–85.

4. SITE-SELECTIVELY GROWN SnO_2 NWS NETWORKS FOR AMMONIA SENSING IN HUMID CONDITIONS

Abstract

SnO_2 NWs networks site-selectively grown on heated micromembranes have been characterized as ammonia sensors. The approach allows achieving reproducible growth together with stable and long-lasting ammonia sensing. The concurrent sensing mechanisms are analyzed relating the experimental sensing kinetics with the known ammonia oxidation processes. In humid conditions, moisture reduces the response to ammonia but also lowers the activation energy of the reaction process. Furthermore, the devices have been tested both in dry and humid conditions showing response time as short as two minutes. Sensors have been tested up to 1 month, only presenting variation of the base resistance with full retention of the response towards the gaseous analytes. The response towards other gases is also presented.

4.1. Introduction

Ammonia is a toxic gas with irritant properties that can injure the respiratory tract [1]. Anthropogenic emissions of ammonia come in a 95% from agriculture, where ammonium salts are widely used as fertilizers [2]. On the other hand, swine farms can achieve high concentrations of ammonia up to 100 ppm, which are dangerous for human health, generated by decomposition of pig manure via metabolic activities of bacteria and fungi [3]. Long term exposure to ammonia must be below 25 ppm in order to avoid difficulties in breathing [4]. Concentrations of 500 ppm of NH_3 leads to immediate and severe irritation of the nose and throat, and above 1000 ppm can cause pulmonary edema.

On the other hand, ammonia, together with urea, is used in automotive applications for selective catalytic reduction (SCR) of nitrogen oxide (NO_x) to nitrogen in order to avoid harmful gas emissions in diesel engines, which gives also H_2O as a byproduct [5,6]. Accurate measurements of the ammonia concentration for SCR are needed in order to achieve an efficient process and to recycle the non-reacted ammonia fraction.

Furthermore, measuring ammonia in breath can provide an easy diagnostic approach for patients with ulcers caused by bacterial stomach infections or kidney disorder [7]. Consequently, a clear necessity of monitoring the ammonia concentration is required in different application fields.

A considerable amount of works are available in literature regarding the sensing of ammonia by employing metal oxide sensors, using a wide variety of materials like SnO_2 [8-12], ZnO [13-15], In_2O_3 [13,16], WO_3 [17,18] or TiO_2 [19,20], either based on a thin film or nanostructured materials. However, just few works study the reaction paths of the interaction of metal oxide/ammonia [21,22]. The reported sensing mechanisms are, mainly, analyzed in dry conditions. On the other hand, density functional theory (DFT) calculations have been performed to study the ammonia adsorption and have been compared with experimental measurements performed on a SnO_2 individual nanowire [12]. The interference of water vapor in that work is, nevertheless, briefly studied.

Nanostructures, and specifically nanowires, as explained in previous chapters, are excellent candidates to be employed as the active part of a gas sensor due to the high surface to volume ratio. Following this direction, the devices presented in chapter 3,

based on SnO_2 nanowires site-specifically grown on micromembranes, have been employed immediately after the growth without requiring any additional fabrication step to study the ammonia adsorption and sensing mechansims.

The nanowires require to be heated in order to enhance the charge transfer between the adsorbate and the surface of the nanowire, i.e., to operate as a gas sensor. Thus, the heater used to promote the growth of the nanowires has been used to provide the desired operation temperature.

In summary, in this chapter an ammonia gas sensor based on SnO_2 nanowires grown by a straight integration process of nanostructures with the electronic platform is presented. The concurrent sensing mechanisms of the interaction with ammonia vapor are related to the experimental observations, and analyzed in detail diluted in air. The interference of water in the sensing processes is well-known for adding complexity to the system, whose contribution has also been studied in this work.

4.2. Experimental section

The micromembranes with buried heaters and top electrodes detailed in section 2.5 are the ones substrates used for these sensors. The electric power consumption at atmospheric pressure requires 13 and 28 mW in order to deliver 200 °C and 400 °C at the surface of the micromembrane, respectively.

The growth of SnO_2 NWs is described in detail Chapter 3. The gas sensing measurements are obtained keeping a constant flow of 200 ml/min for dry and humid air measurements. The relative humidity conditions indicated throughout the paper are referenced to the RH at room temperature.

4.3. Results and discussion

4.3.1. Oxygen adsorption

The behavior of the electrical resistance of SnO_2 NWs at different temperatures in air has been investigated in order to study the initial oxygen species that are chemisorbed at the surface of the metal oxide nanostructure (Figure 4.1 a)). I-V curves

of the sensor show an ohmic behavior even at room temperature, which remarks the absence of a Schottky barrier that would be expected for a pure Pt/SnO_2 interface as a consequence of the difference in electron affinity and work function of the two materials. The interface between the Pt electrodes and the SnO_2 NWs is partially responsible for the low resistance values observed, since a Schottky barrier would decrease the conductivity of the network of the nanowires.

Regarding the temperature behavior, the resistance of SnO_2 NWs at room temperature is 2850 Ω, and decreases for increasing temperatures up to 200 °C. Above this temperature, the resistance changes its tendency and increases with temperature. The observed $R(T)$ curve is associated with the gas specie adsorbed on the surface, i.e., oxygen specie.

Atmospheric oxygen is predominantly physisorbed at the surface of the SnO_2 at low temperatures, i.e., below 100°C approximately [23]. This mechanism takes place without electron transfer with the surrounding adsorbate; therefore, no change in the resistance of the semiconductor occurs. During physisorption, the observed reduction of resistance is purely due to the excitation of charge carriers.

On the other hand, molecular oxygen (O_2^-) is chemisorbed at the surface at temperatures around 150-200 °C, leading to a charge transfer from the oxide towards the adsorbate, following the reaction:

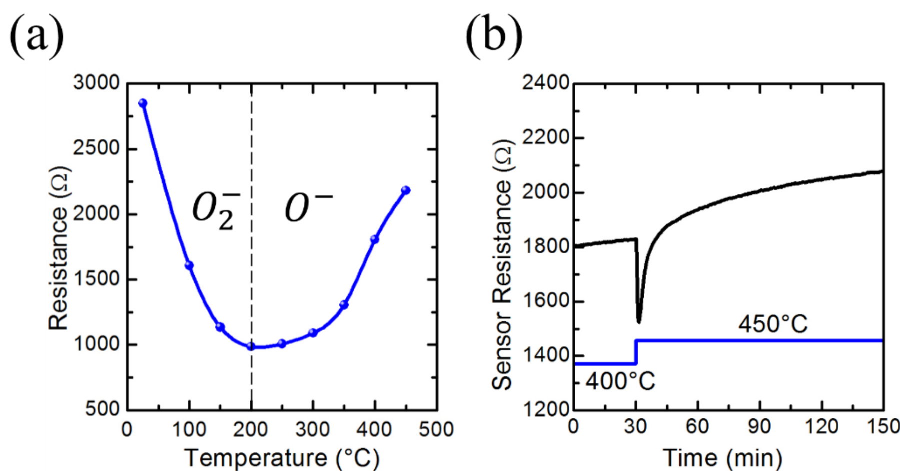

Figure 4.1 a) Resistance of SnO_2 locally grown NWs as a function of temperature. The minimum in resistance reflects the change in the adsorbed oxygen specie; b) Transient response of the sensor resistance in a change of temperature illustrating the increase in resistance for increasing temperatures above 200 °C. Blue line represents the evolution of temperature.

$$O_{2(g)} + e^{-} + S \leftrightharpoons O^{-}_{2(s)} \quad (4.1)$$

Above 200 °C the oxygen trapped through chemisorption can dissociate into two atomic oxygen species (O^-) according to:

$$O^{-}_{2(g)} + e^{-} \leftrightharpoons 2O^{-}_{(g)} \quad (4.2)$$

Consequently, O^- leads to capturing more electrons from the semiconductor and, thus, produces an increase of its resistance, which explains the behavior in Figure 4.1 a), in a good agreement with other authors regarding the temperature range [23,24]. Therefore, we can conclude that the resistance change is related to the particular oxygen species adsorbed at the metal oxide surface. A completely different situation occurs in a high temperature regime, starting at 600 °C, at which oxygen atoms that share two electrons (O^{2-}) with the metal oxide are promoted [23]. However, these high temperatures are beyond the range of the gas sensing measurements carried out in the present work.

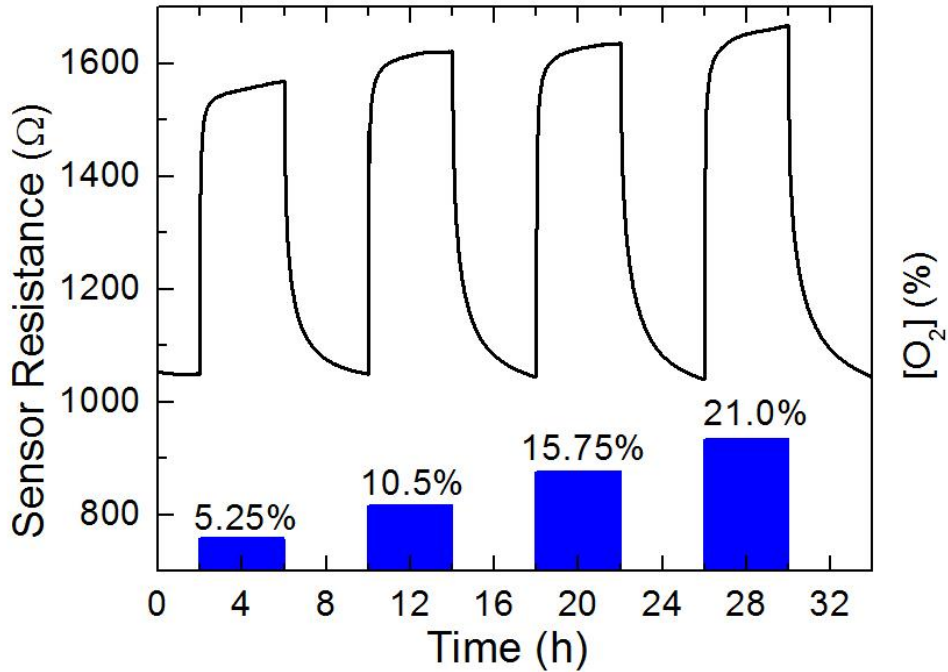

Figure 4.2. Change in resistance of SnO_2 NWs towards different oxygen concentration diluted in nitrogen. The temperature is kept at 150 °C.

A transient response of the SnO_2 NW device's resistance with increasing temperature from 400 to 450 °C is represented in Figure 4.1 b). The low thermal mass of the micromembranes provides a fast thermal response; for instance, only tens of microseconds are required to reach 200 °C [25]. Therefore, the initial fast decay in resistance when the temperature is changed (at time 30 minutes) is due to the increase in charge carriers as a result of the temperature rise.

The gradual increase in resistance that follows, can only be related to the chemisorption of atomic oxygen species, since temperature changes induce a new dynamic equilibrium between the wire and the adsorbate in a slower process than the thermal induced increase of charge carriers. Consequently, chemisorption of oxygen molecules is the cause of the positive resistance coefficient observed for temperatures above 150 °C.

From another point of view, the oxygen adsorption has been studied keeping a constant temperature, and changing its concentration using nitrogen as a background gas. The evolution of the resistance towards this gas mixture is represented in Figure 4.2, where the temperature was kept at 150 °C. Oxygen is let in into the chamber for 4 hours, the same time hold as a recovery time. Although a fast initial increase is observed after the introduction of the nitrogen-oxygen gas mixture, the complete saturation of the response, i.e., the time required to achieve a steady state value takes about 7 hours.

The response towards concentrations above 10.5 of oxygen is maintained almost stable, as observed in Figure 4.2, meaning that the surface reached the maximum oxygen coverage, leading to the saturation of the response. On the other hand, it is inferred that the sensor would not exhibit any change in the baseline when working in an oxygen deficient environment, above 10% of oxygen concentration.

4.3.2. Response to ammonia in dry synthetic air

The change in resistance of the locally grown nanowires against ammonia in synthetic air has been studied at different temperatures. The concentration of ammonia has been varied between 10 and 40 ppm, which is in the range of time-weighted average exposure limit recommended by NIOSH (25 ppm) for up-to 10 h workday [4]. The evolution of the sensor's resistance at different temperatures and for changing pulses of ammonia is represented in Figure 4.3 a), where the decrease in resistance in the

presence of ammonia, expected for an n-type semiconductor gas sensor, like tin dioxide, towards a reducing gas, is observed.

The response of the sensor is defined as:

$$Response(\%) = \frac{R_{air} - R_{gas}}{R_{air}} \tag{4.3}$$

The summary of the responses as a function of temperature is represented in Figure 4.3 b). The locally grown SnO_2 NWs show a response of up to 36% for 40 ppm of NH_3 at 400 °C, temperature at which the highest response is found.

On the other hand, the response time has been calculated, defined as the time to evolve from 10% to 90% of the steady state value. A response time as low as 2 minutes is obtained, again, at 400 °C. An Arrhenius plot of the response time as a function of the temperature is represented Figure 4.3 (c), which is fitted to an exponential behavior following $\tau = \tau_0 \exp\left(\frac{E_{act}}{k_B T}\right)$.

Concerning the sensing mechanisms that leads to the change in resistance, three competitive reactions are described in the literature for ammonia oxidation on metal oxide surfaces [21,22,27]:

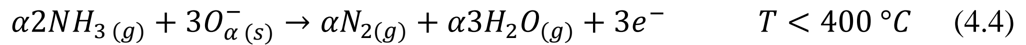

$$\alpha 2NH_{3\,(g)} + 3O^{-}_{\alpha\,(s)} \rightarrow \alpha N_{2(g)} + \alpha 3H_2O_{(g)} + 3e^{-} \qquad T < 400\,°C \tag{4.4}$$

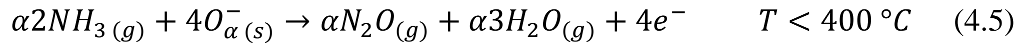

$$\alpha 2NH_{3\,(g)} + 4O^{-}_{\alpha\,(s)} \rightarrow \alpha N_2O_{(g)} + \alpha 3H_2O_{(g)} + 4e^{-} \qquad T < 400\,°C \tag{4.5}$$

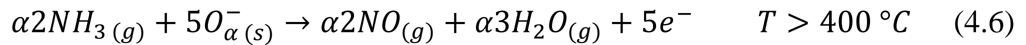

$$\alpha 2NH_{3\,(g)} + 5O^{-}_{\alpha\,(s)} \rightarrow \alpha 2NO_{(g)} + \alpha 3H_2O_{(g)} + 5e^{-} \qquad T > 400\,°C \tag{4.6}$$

where *(g)* stands for a non-adsorbed gas molecule, *(s)* for a molecule adsorbed at the surface, e^- is a conduction electron, α is a coefficient that is equal to 1 for atomic oxygen O^- or 2 for molecular oxygen O_2^- ionosorbed species. The oxygen specie adsorbed at the surface depends on the working temperature. From the results obtained in the previous section, for 100<T<200 °C molecular oxygen is predominantly adsorbed, and above 200 ºC the atomic form is mainly found at the surface. The three reaction mechanisms (4.4)-(4.6) are supported by chemisorbed oxygen at the surface of the metal oxide, which corresponds to the temperature regime used in this work, above 150 °C, employed in order to achieve acceptable response time for the gas sensing.

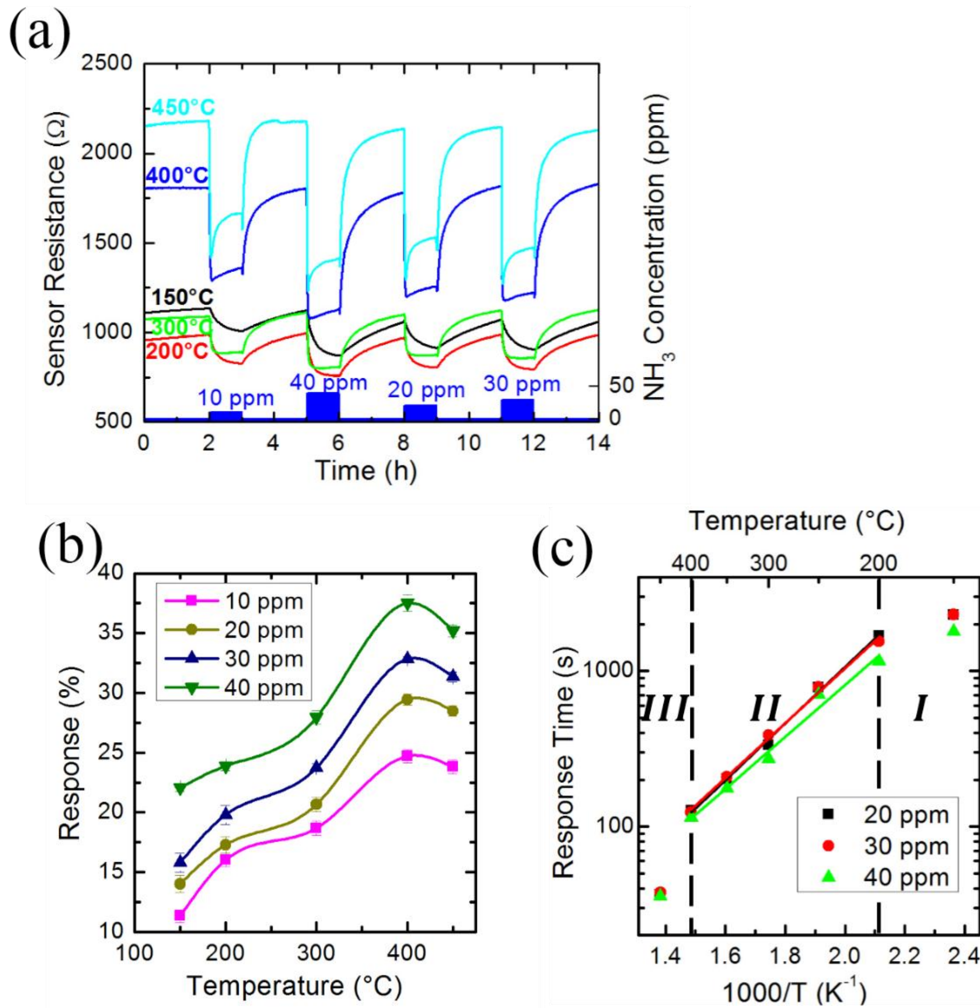

Figure 4.3 a) Evolution of SnO_2 NWs resistance in front of different concentration of ammonia in synthetic air; b) Response of the test represented in a) in function of temperature; c) Arrhenius plot of the response time for pulses of 30 ppm of NH_3. Symbols are experimental values and lines are the fitted exponential decay.

It is well known from catalysis that in a large number of metal oxides, depending on the temperature, one specific reaction is preferred over the others [27,28]. In this direction, it is difficult to distinguish between the sensing reactions (4.4) and (4.5). Indeed, these reactions account for oxygen adsorption in the form of the active species and subsequent H stripping from the ammonia molecules until a relevant intermediate containing the N-N or N-O bond is formed. When this takes place, further H elimination with the concomitant formation of H_2O takes place. Furthermore, equations (4.4) – (4.6) share more than 70% of their elementary steps. Consequently, in the low temperature regime, i.e., below 400 °C approximately, the reactions (4.4) and (4.5) take place simultaneously.

Reaction (4.6) dominates at temperatures above 400 °C and surface coverage governs the reaction. Since higher energy barriers can be surpassed at this temperature, the NO byproduct becomes dominant [27,28].

The nitrogen containing products of the three reactions are therefore oxidized as a function of temperature: the higher the temperature at which the reaction takes place, the more oxidized is the nitrogen containing product. At the same time, the more oxidized is the nitrogen product, the higher the activation energy, following the relationship $E_{(4.4)}^{act} < E_{(4.5)}^{act} < E_{(4.6)}^{act}$ [27].

The activation energy of the sensor response towards ammonia has been obtained from the exponential temperature behavior of the response time, which is represented in Figure 4.3 c) in an Arrhenius plot. Three different kinetic regions are defined from the plot according to the experimental measurements: I) temperatures below 200 °C; II) between 200 and 400 °C and III) above 400 °C. Each of these regions presents different activation energies.

The interaction with ammonia at region I, i.e., at low temperature, involves molecular oxygen ions, since this specie and not atomic oxygen is the main adsorbate form at this temperature range, as discussed previously. The activation energy from region I cannot be derived due to the small number of points measured, but a lower slope than region II can be inferred.

The activation energy obtained from the Arrhenius plot in region II is $E_{II}^{act} = 0.35 \pm 0.04 eV$, which corresponds to a temperature ranges between (200>T>400°C), governed by atomic oxygen (α=1). Thus, atomic oxygen reacts with ammonia causing a higher activation energy than the molecular form (α=2) ($E_{O_2}^{act} < E_{O}^{act}$), which has been also reported in [29]. Therefore, the differences in sensing kinetics observed on the Arrhenius plot are between region I and II are explained by the different oxygen species promoting the NH_3 oxidation.

On the other hand, this region comprehends the temperature range where reactions (4.4) and (4.5) can take place on the tin dioxide surface. The exponential behavior of the response time in the Arrhenius plot suggests that the same mechanism takes place over the whole temperature range. This confirms what was pointed out before, that both

reactions can occur simultaneously at these temperatures and that their contribution cannot be separated from each other.

Furthermore, the ratio between oxygen and ammonia partial pressures (p_{O_2}/p_{NH_3}) also influences which of the three reactions are dominant. As shown in [27], for p_{O_2}/p_{NH_3}>10 and temperatures below 400 °C, which are the conditions of the region II, the selectivity is lost, and N_2 and N_2O are produced in equivalent percentage. On the other hand, for low p_{O_2}/p_{NH_3} ratios (<0.1), N_2 production is enhanced [22,27] and N_2O production is almost negligible. This is in agreement with the described sensing mechanism in region II.

Comparing the values of the activation energy to those available in the literature, the one obtained in this work (0.35 eV) is lower than the reported ones in [27] and [12], which obtained an activation enthalpy of 0.74 eV (temperature range between 210-260 °C, reaction mixture of 10% of ammonia and 90% of O_2) and 0.5 eV (150<T<300 °C, 21% O_2 and 200 ppm of NH_3), respectively.

Furthermore, density functional theory (DFT) studies concluded that the rate-determining step of NH_3 sensing mechanism in a single SnO_2 monocrystalline nanowire is the oxygen adsorption, with an associated activation energy of 0.5 eV, not far from the experimental value obtained in that work [12]. Notice, though, that the errors intrinsic to DFT, particularly when dealing with the description of O_2, make the DFT value only a qualitative estimate. Additionally, if oxygen adsorption is energetically favored, i.e. oxygen binding energy to the surface increases, then the activation energy of the whole process could be lowered.

A change in tendency of the response time as a function of temperature is observed at 450 °C (see Figure 4.3 c)), the labelled region III. The variation in the kinetic behavior at 450 °C suggests that a different reaction takes place, which could correspond to (4.6), since this reaction starts to dominate at about 400 °C. The temperature intervals for the reaction that give rise to NO production are in agreement with other works, and are also supported by the faster response of the sensor's resistance due to the ammonia interaction between 400 and 450 °C. The initial interaction of ammonia with the metal oxide surface leads to a fast reduction of the NWs resistance at these temperatures, followed by a slow increase during the further exposure to NH_3. The same behavior has also been observed in metal oxide sensors like

WO_3 [18] and In_2O_3/MgO bilayer structure [21] in the characterization of their responses towards ammonia diluted in air.

This slow rise in resistance indicates, probably, that it is caused by gas adsorption. It is well known that nitric oxide (NO) is easily and readily oxidized to NO_2 at 400 °C [21,30]. SnO_2 NW-base gas sensors are known to respond to NO_2 concentrations below 100 ppb [31], a value that can be easy to reach during the ammonia and nitric oxide oxidation. Other products generated in the reactions cannot explain the observed increase in the resistance. On the one hand, H_2O acts as a reducing gas to tin dioxide and its adsorption would give rise to a reduction of the resistance of n-type tin oxide NWs and, consequently, as a product of reaction (4.4), (4.5) and (4.6), could not account for the increase in resistance. N_2 behaves as inert gas at the analyzed temperature range and does not affect the conductivity. Furthermore, SnO_2 without additives on its surface requires tens of ppm of N_2O [32] to achieve an observable response. As a result, the only reaction that will give rise to the observed behavior is the oxidation of NO to NO_2, which is the only specie able to promote the resistance increase. According to this, NO_2 attaches to an oxygen vacancy at the SnO_2 surface [33], trapping an electron, and therefore the resistance of the SnO_2 is increased as a result of the reactions:

$$2NO_{(g)} + O_2 \rightarrow 2NO_{2(g)} \quad (4.7)$$

$$NO_{2\,(g)} + e^- \rightarrow NO^-_{2(s)} \quad (4.8)$$

In fact, the initial resistance drop towards ammonia at 450 °C is larger than that at 400 °C, although the further resistance increase due to NO_2 adsorption reduces the final response (see Figure 4.4 d)). Consequently, at this temperature, the process is described by equations (4.6), (4.7) and (4.8) that take place simultaneously, being the last two secondary reactions.

4.3.3 SnO_2 NWs sensing mechanisms in humid conditions

4.3.3.1 SnO_2 NWs interaction towards H_2O

Water vapor is a gas widely present in the atmospheric air, that interferes with other gas analytes in gas sensing processes. The interaction of water vapor diluted in synthetic air with the surface of thin or thick SnO_2 films has been studied and examined at

temperatures between 200-400 ºC [34-36], exhibiting a reversible response for different concentrations of water vapor. Less works are found regarding the water response towards SnO_2 NWs [37].

The changes in the electrical signal of the sensor towards the presence of water vapor are shown in Figure 4.4 a) at an operation temperature of 400 °C. The concentration of water vapor in this work is expressed as relative humidity in %, i.e., the ratio of partial water vapor pressure and saturation pressure obtained at room temperature (20 °C).

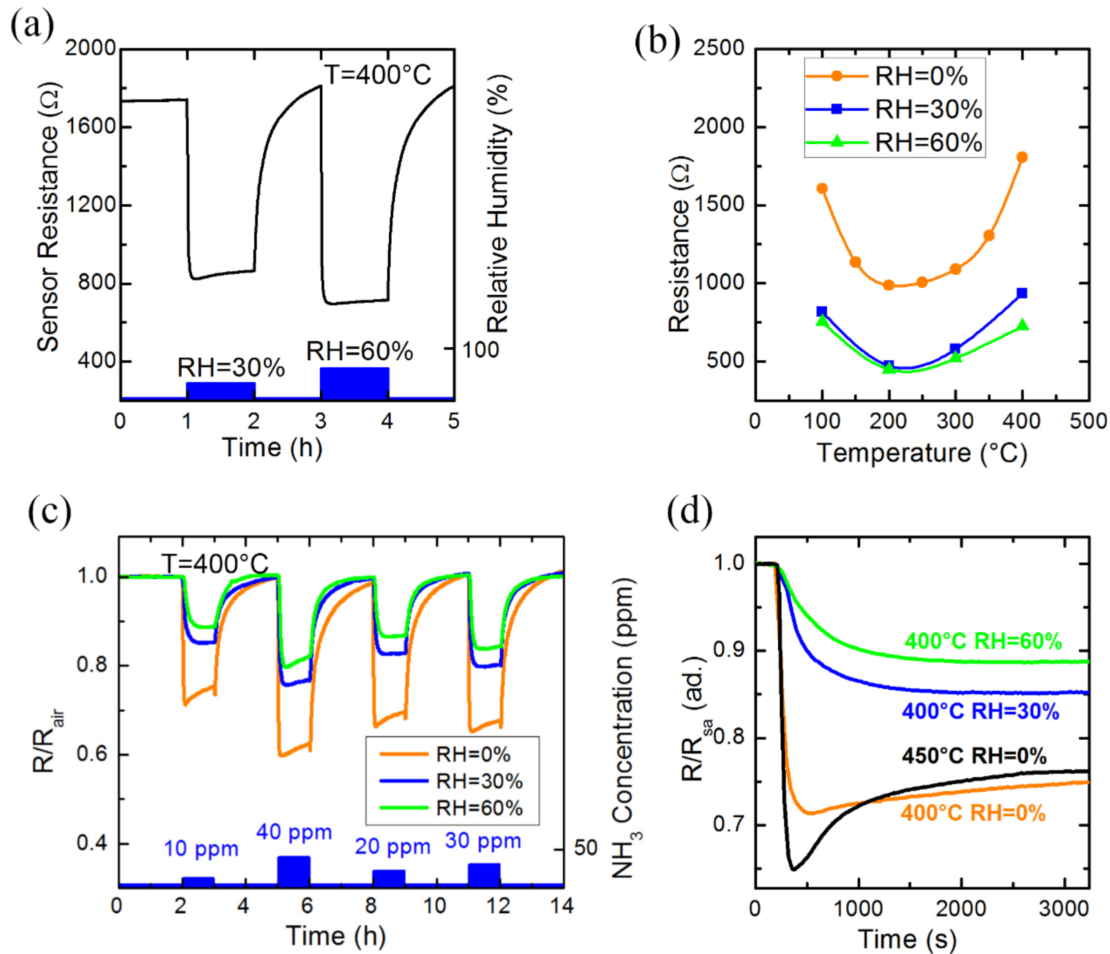

Figure 4.4 a) Electrical response of SnO_2 NWs to different concentrations of water vapor in synthetic air at 400 °C; b) Resistance of SnO_2 NW-based gas sensor for different humidity levels at different temperature. The U-shaped R-T curve is also obtained in humid conditions due to dissociation of molecular to atomic oxygen at a temperature of 200 °C; c) Electrical response of SnO_2 NWs in dry, 30% and 60% relative humidity conditions (RH at room temperature) towards different ammonia pulses in synthetic air. Three tests have been performed by keeping a constant temperature of 400 °C; d) Sensor response towards 10 ppm of NH_3 at different water vapor conditions. The overshoot in resistance is visible for 450 °C and RH=0% curve.

A clear decrease in resistance due to the presence of water vapor is observed, which is reversible, as can be seen in the same figure from the fact that the baseline value is fully recovered when water vapor is removed from the chamber. The behavior of the NWs resistance as a function of the relative humidity denotes that water vapor acts as a reducing gas for SnO_2 nanostructures. There are several mechanisms proposed in the literature explaining the interaction of H_2O with the tin dioxide surface.

The first mechanism is based on the homolytic dissociation of water, which involves the reaction with lattice oxygen, leading to the production of two rooted hydroxyl groups. Thus, two electrons per water vapor molecule are released to the conduction band according to the following equation [34,35,38]:

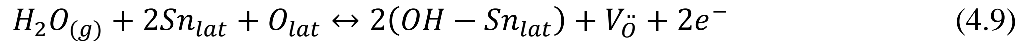

$$H_2O_{(g)} + 2Sn_{lat} + O_{lat} \leftrightarrow 2(OH - Sn_{lat}) + V_{\ddot{O}} + 2e^- \quad (4.9)$$

where Sn_{lat} and O_{lat} stands for a tin and oxygen atom in lattice position, respectively, and $V_{\ddot{O}}$ is a doubly ionized oxygen vacancy. The neutral H atoms from the water vapor molecule react with lattice oxygen to form OH. The electron affinity of OH is lower than the lattice oxygen, and as a consequence, it is ionized more easily and gives as a result the donation of electrons to the metal oxide.

Another mechanism related to chemisorbed oxygen at the SnO_2 surface is the reaction of water with pre-adsorbed oxygen ions, which is similar to equation (4.9), but involves chemisorbed atomic oxygen [35]:

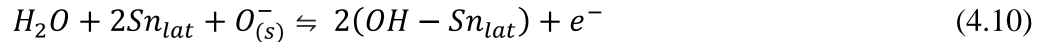

$$H_2O + 2Sn_{lat} + O^-_{(s)} \leftrightharpoons 2(OH - Sn_{lat}) + e^- \quad (4.10)$$

Equation (4.10) is supported by diffuse reflectance infrared Fourier transform (DRIFT) spectroscopy measurements that conclude that only OH terminal groups are formed at the surface of SnO_2 [35]. The authors observed that the concentration of these surface hydroxyl groups increased with oxygen partial pressure, reaching a saturation, and showed that this effect was reversible. Therefore, the concentration of hydroxyl groups, which can account for the increase in conductivity to the metal oxide, is strongly dependent on chemisorbed oxygen. Consequently, when another reducing gas is present in the measuring chamber, besides H_2O, both will compete for reacting with chemisorbed oxygen atoms, as will be considered in the combined response to water vapor and ammonia.

The resistance as a function of temperature in both dry and humid conditions (30% and 60% relative humidity) is represented in Figure 4.4 b). As can be seen, the sensor's resistance decreases at higher concentrations of water vapor, confirming the reducing character of this gas and the fact that, even though a very high concentration of gas is introduced into the chamber, no saturation has been reached. On the other hand, the resistance of SnO_2 NWs increases with temperature above 200 °C, showing a U-shaped resistance-temperature curve, which is in agreement with the curve shown in Figure 4.1 that is related to the different oxygen species adsorbed at the surface of the metal oxide. This increasing resistance, as shown in section 4.3.1, is due to the adsorption of atomic oxygen and, therefore, it is ensured that atomic oxygen is available to react with ammonia in the presence of water vapor, as discussed in the next section.

4.3.3.2 Ammonia sensing in humid conditions

Once the resistance changes of locally grown nanowires towards different concentrations of NH_3 and water vapor have been separately analyzed in detail, the sensing capabilities of the nanowires are studied with both gases being simultaneously present.

The tests have been carry out by adding two different concentrations of water vapor to synthetic air; in terms of relative humidity, the employed levels are 30 and 60% for each temperature. The humid air is considered as the background, and hence, ammonia has been added to it, using the same sequence of ammonia pulses as used in the dry air experiments. The response of the SnO_2 NWs has been investigated at temperatures of 200, 300 and 400 °C. Operating at this temperature range, mainly atomic oxygen is chemisorbed at the semiconductor's surface.

The sensor's resistance, normalized to the baseline (SA+H_2O) value at 400 °C, is represented in Figure 4.4 c) for both dry and humid conditions towards different concentrations of ammonia. As can be clearly seen, the response (resistance variation) is reduced in the presence of increasing amounts of water vapor as compared to dry conditions. The sensor's resistance does not show the overshoot in resistance which was observed in the response towards ammonia in dry conditions at 450 °C (see Figure 4.4 d) for comparison), suggesting that reactions (4.4) and (4.5) are the main ones occurring in the studied range, while the effect of equation (4.6) is here negligible.

The reduced response of tin dioxide nanowires against ammonia in the presence of water vapor can be explained by several concurring mechanisms. On the one hand, competitive adsorption between water vapor and ammonia with chemisorbed oxygen takes place, as described in reaction (4.10) for water vapor, and in (4.4), (4.5) and (4.6) for ammonia sensing. Furthermore, 60% of relative humidity at 20 °C corresponds to approximately 14300 ppm of water, a concentration three orders of magnitude higher than that of ammonia throughout these experiments. Thus, the partial pressure of water vapor is considerably higher than that of ammonia, which should lead to a much higher coverage of the dissociated fragments at the metal oxide surface.

The Arrhenius plot of the response time of the sensor in dry and humid conditions for 30 ppm of ammonia (Figure 4.5 a)) shows that the response is slower in humid conditions. Longer response times are a direct consequence of the competitive adsorption between atomic oxygen and water vapor that reduces the probability of oxidizing ammonia to be adsorbed and decomposed at the surface and, thus, slows down the reaction.

At the same time, the activation energies shown in Figure 4.5 b), deduced from Figure 4.5 a) for the different ammonia concentrations at the various studied relative humidity values, clearly decrease in the presence of water vapor and are essentially independent of the ammonia concentration, at least, within the experimental uncertainty of these experiments. As mentioned before, water vapor can be dissociated in two hydroxyl species, those being chemisorbed at the surface of tin oxide assisted by Sn_{lat} and $O^{-}_{(s)}$ as described in reaction (4.10). A tentative explanation for the behavior could be derived from the interaction of hydroxyl groups with O_2, as proposed by Epling *et al.* [39,40] in monocrystalline rutile TiO_2 according to:

$$OH_{(s)} + O_{2(g)} \rightarrow O^{-}_{(s)} + (O_a - OH)_{(s)} \quad (4.11)$$

Where O_a stands for an oxygen adatom. This mechanism creates a new path for oxygen dissociation, which can occur even at lower temperatures than oxygen dissociation described according to reaction (4.1), reducing the activation barrier for oxygen dissociation. According to other works dealing with ammonia interaction mechanisms, oxygen dissociation is precisely the energy limiting step [12].

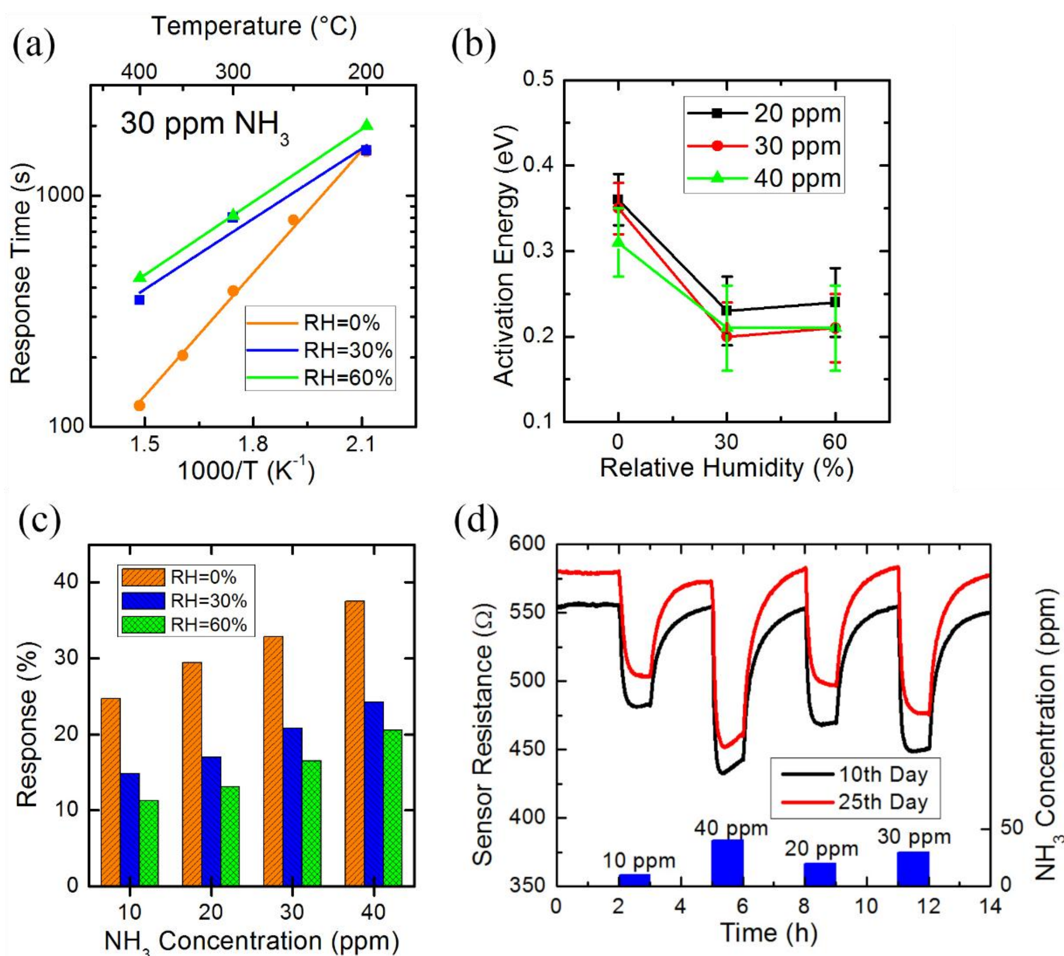

Figure 4.5 a) Sensor response time for NH_3 pulses of 30 ppm in dry and humid conditions, represented in an Arrhenius plot. Symbols are experimental values and lines are the fitted exponential decays; b) Activation energy obtained from the response time to ammonia as a function of the relative humidity for all the concentrations studied in this work; c) Response of SnO_2 NWs against ammonia in humid condition at 400 °C; d) Comparison between the response of the sensor at 300 °C and 30% of RH from 10th and 25th day of measurements. A change of 5% in the resistance baseline is seen, while the response is almost unchanged.

Thus, a mechanism similar to (4.11) could justify the lowering in the activation energy of ammonia sensing in presence of water. The oxygen (O_a) grows with increasing number of OH groups at the surface, and can act as sites for dehydrogenation of ammonia (H scavenging centers), following the same scheme provided in dry air.

Regarding the long-term stability of the SnO_2 nanowires operating in the extremely aggressive ammonia environment, the sensors were operated for 1 month in dry and humid conditions. The most noticeable result is that a drift in resistance of 7% from the initial values was observed, but where the resistance change due to the presence of the gases was almost invariant in its value, being only about 1% in terms of response. Figure 4.5 d) shows the resistance change at 300 °C and 30% of RH obtained at the 10th and 25th day of operation, and illustrates the repeatability of the measurements obtained

by this nanowire-based device. The sensor has shown a good durability, and offers relatively fast response time towards 30 ppm of NH_3 of 6 minutes in the presence of water vapor, and 2 minutes in dry conditions.

4.3.4. Response towards other gases

Some other gas sensing results will be presented in this subsection. As it is well known, although metal oxides present highly sensitivity and low cost, among other benefits, they are not selective to a specific gas specie, i.e., metal oxides show a response against several oxidising and reducing gases. Here the behaviour towards CO and NO_2 will be shown.

4.3.4.1. Response towards CO

The measurements of the interaction of the SnO_2 nanowire-based devices towards different CO concentrations in dry synthetic air are shown in Figure 4.6 a). It is evident that the interaction of this gas with the metal oxide gives rise to a reduction in the resistance of the nanowires and that this reduction increases with CO concentration, as in the case of ammonia, confirming the reduction character of this gas. Note that the lowest tested CO concentration (10 ppm) is very close to the legal limit for 8h exposure time weighted average (TWA) of 8.6 ppm [41]. As for completeness, the reaction path that leads to the sensing of CO at the SnO_2 surface is described according to [42] in the following equation:

$$\beta CO_{(g)} + O^{-}_{\beta(s)} \rightarrow \beta CO_{2(g)} + e^{-} + S \qquad (4.12)$$

The equation describes the oxidation of CO by previously chemisorbed molecular (β=2) or atomic (β=1) oxygen, in a similar way to the description of the ammonia oxidation of section 4.3.2, but following a more simple path in dry conditions because of the more simple CO molecule.

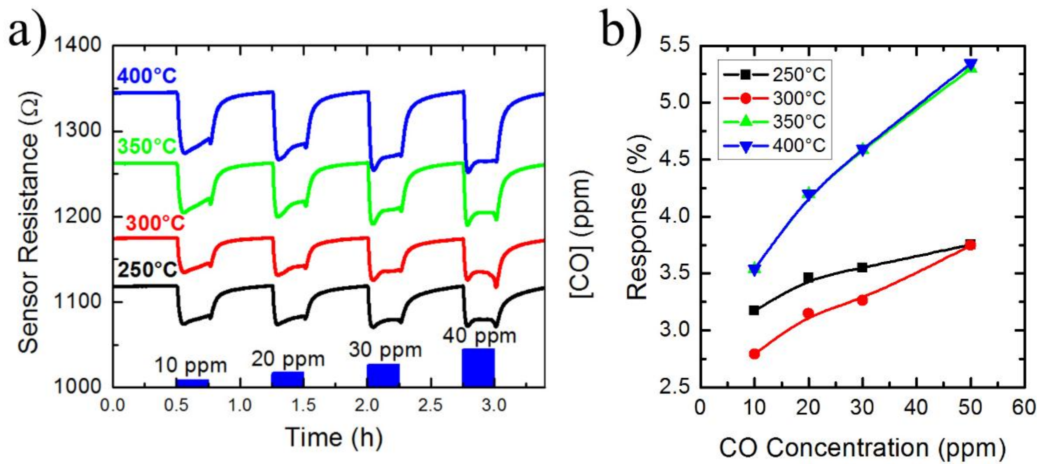

Figure 4.6. a) Different resistance evolutions of SnO_2 NWs network to pulses for several concentrations of CO in synthetic air at different temperatures; b) Response of the NWs network as a function of CO concentration.

The response towards CO is defined in the same form as for ammonia, since both are reducing gases, in (4.3). The change of the device's resistance is about 3% for the lowest concentrations employed in this work, illustrating that the nanowires are less sensitive to the harmful concentrations of CO than for ammonia (see Figure 4.6 b)). The response time is below 1 minute for all the represented sensing experiments towards CO.

4.3.4.2. Response towards NO_2

Nitrogen dioxide is a harmful gas that causes adverse respiratory effects, produced mainly by the internal combustion engines that burn fossil fuels. Nitrogen dioxide is an important gas for sensing and detection, due to the presence of harmful concentrations in cars and roads. Concentrations above 210 ppb can provide adverse effects on human health, even though is still not understood if they are caused by NO_2 itself or by other secondary combustion related by-products [43].

The resistance of SnO_2 NWs have been characterized towards different concentrations of NO_2 diluted in synthetic air at different temperatures, as shown in Figure 4.7 a). The exposure time of NO_2 is 15 min, and the time left for the sensor recovery is 30 minutes. As shown previously in this chapter, the total resistance of the NWs increases with the temperature above 200ºC due to the dissociation of molecular oxygen into atomic oxygen. NO_2 increases the resistance of the nanowires network through its adsorption at the surface oxygen vacancies (see eq. (4.8)).

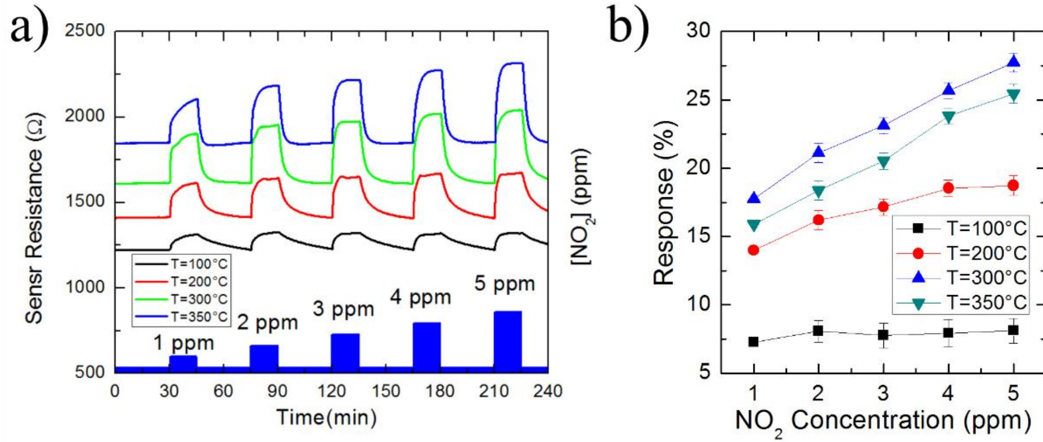

Figure 4.7. a) Resistance evolution of SnO_2 NWs towards NO_2 in synthetic air; b) response of the NWs for increasing nitrogen dioxide concentration. Maximum response is obtained at 300 °C.

The response of the sensor is represented in in Figure 4.7 b), obtained according to:

$$Response(\%) = \frac{R_{NO_2} - R_{air}}{R_{air}} \quad (4.13)$$

The adsorption of NO_2 is slightly promoted at 100 °C and, at the same time, with the increase of the temperature, the response and recovery time are reduced. The maximum response occurs at 300°C. Remarkably, the response time at 300°C for 5 ppm of nitrogen dioxide is less than 3 minutes.

The response towards NO_2 at 300 ºC can be extrapolated to the recommended exposure limit, (210 ppb), obtaining a value of 15.7±0.4% of response. Therefore, the sensor should be able to detect the presence as low as 100 ppb of NO_2 according to the results obtained.

4.4. Summary of the different responses

The results presented above confirm the non-selective response of the fabricated gas sensors, as it is expected for most metal oxides and, concretely, for SnO_2 NWs.

The response of the devices to the different gases, however, shows fast response with a stable behaviour, confirming their operability and stability. It is important to point that low consumption in the range of tens of mW is required for the operation of the sensor and that this mainly comes from the heater consumption.

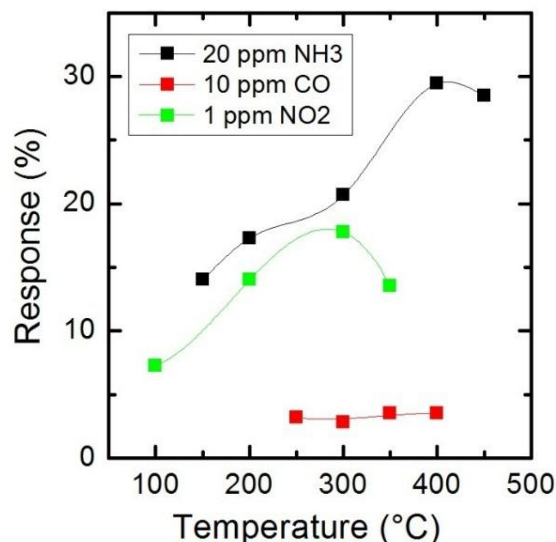

Figure 4.8. Temperature behavior of the response of SnO_2 NWs towards different gases in synthetic air. The maximum response observed is against NH_3.

The temperature behaviour of the sensor's resistance towards different gas species is depicted in Figure 4.8, namely for 20 ppm of NH_3, 10 ppm of CO and 1 ppm of NO_2. The selected concentrations of gases are the nearest measured proportions to the recommended exposure limits that one would consider as the highest values to be measured. The ammonia and carbon monoxide concentrations are in the range of the exposure limit recommended by WHO or NIOSH, however, nitrogen dioxide is one order of magnitude above (210 ppb) [43].

The highest response obtained towards the oxidizing and reducing gases correspond to 20 ppm of ammonia, at 400°C, with a value of 30%. The sensor response towards CO reaches a value of 5.3% at the same temperature. Towards NO_2, although it has been analysed up to 350 °C, a response around 10% can be estimated from the Response-Temperature curve. Thus, the responses towards the other gases are negligible in front of the ammonia interaction.

On the other hand, water vapour is observed to reduce importantly the resistance of the NWs, whose adsorption on the surface of the NWs is saturated at relative humidity levels above 60%, since no further reduction is observed at higher levels.

4.4 Conclusions

SnO_2 nanowires locally grown nanowires on microhotplates, have shown a complex behaviour towards ammonia diluted in dry and humid synthetic air that has been described in detail and analysed from not only the electrical response point of view but also the kinetics. Different temperature regimes have been identified in the sensor kinetic response. In dry conditions, the promotion of NO as byproduct at high operating temperatures reduces the response of the sensor and gives rise that the maximum response to ammonia is obtained at 400 °C. When operated in humid conditions, the response of tin dioxide nanostructures is reduced and slowed down by the presence of water vapor. Simultaneously, the activation energy is lowered by moisture, which could be explained through the reaction between O_2 and the OH adsorbed groups, consequence of water decomposition.

Finally, the integrated growth of SnO_2 on micromembranes has been demonstrated as a fast, reproducible and low power consuming approach, which gives rise to ammonia sensors with good repeatability and fast response. Sensors have been tested up to 1 month, only presenting variation of the base resistance with full retention of the response towards the gaseous analytes.

4.5 References

[1] T.M. Banhazi, J. Seedorf, D.L. Rutley, W.S. Pitchford, Identification of risk factors for sub-optimal housing conditions in Australian piggeries: Part 1. Study justification and design, J. Agric. Saf. Health. 14 (2008) 5–20.

[2] J.N. Galloway, F.J. Dentener, D.G. Capone, E.W. Boyer, R.W. Howarth, S.P. Seitzinger, et al., Nitrogen cycles: Past, present, and future, 2004. doi:10.1007/s10533-004-0370-0.

[3] F.-X. Philippe, J.-F. Cabaraux, B. Nicks, Ammonia emissions from pig houses: Influencing factors and mitigation techniques, Agric. Ecosyst. Environ. 141 (2011) 245–260. doi:10.1016/j.agee.2011.03.012.

[4] National Institute for Occupational Safety and Health (NIOSH), NIOSH Pocket Guide to Chemical Hazards - Human Services, Saf. Heal. (2007).

[5] S. Brandenberger, O. Kröcher, A. Tissler, R. Althoff, The State of the Art in Selective Catalytic Reduction of NOx by Ammonia Using Metal-Exchanged Zeolite Catalysts, Catal. Rev. 50 (2008) 492–531. doi:10.1080/01614940802480122.

[6] M. Mehring, M. Elsener, O. Kröcher, Diesel soot catalyzes the selective catalytic reduction of NOx with NH3, Top. Catal. 56 (2013) 440–445. doi:10.1007/s11244-013-9993-5.

[7] B. Timmer, W. Olthuis, A. Van Den Berg, Ammonia sensors and their applications - A review, Sensors Actuators, B Chem. 107 (2005) 666–677. doi:10.1016/j.snb.2004.11.054.

[8] D.C. Meier, S. Semancik, B. Button, E. Strelcov, A. Kolmakov, Coupling nanowire chemiresistors with MEMS microhotplate gas sensing platforms, Appl. Phys. Lett. 91 (2007) 1–4. doi:10.1063/1.2768861.

[9] A. Teeramongkonrasmee, M. Sriyudthsak, Methanol and ammonia sensing characteristics of sol-gel derived thin film gas sensor, Sensors Actuators, B Chem. 66 (2000) 256–259. doi:10.1016/S0925-4005(00)00346-4.

[10] G.X. Wang, J.S. Park, M.S. Park, X.L. Gou, Synthesis and high gas sensitivity of tin oxide nanotubes, Sensors Actuators, B Chem. 131 (2008) 313–317. doi:10.1016/j.snb.2007.11.032.

[11] L.V. Thong, L.T.N. Loan, N. Van Hieu, Comparative study of gas sensor performance of SnO2 nanowires and their hierarchical nanostructures, Sensors Actuators, B Chem. 150 (2010) 112–119. doi:10.1016/j.snb.2010.07.033.

[12] F. Shao, M.W.G. Hoffmann, J.D. Prades, J.R. Morante, N. López, F. Hernández-Ramírez, Interaction mechanisms of ammonia and Tin oxide: A combined analysis using single nanowire devices and DFT calculations, J. Phys. Chem. C. 117 (2013) 3520–3526. doi:10.1021/jp3085342.

[13] C.S. Rout, M. Hegde, a Govindaraj, C.N.R. Rao, Ammonia sensors based on metal oxide nanostructures, Nanotechnology. 18 (2007) 205504. doi:10.1088/0957-4484/18/20/205504.

[14] G.K. Mani, J.B.B. Rayappan, A highly selective room temperature ammonia sensor using spray deposited zinc oxide thin film, Sensors Actuators, B Chem. 183 (2013) 459–466. doi:10.1016/j.snb.2013.03.132.

[15] M.Z. Yang, C.L. Dai, C.C. Wu, A Zinc Oxide Nanorod Ammonia Microsensor Integrated with a Readout Circuit on-a-Chip, Sensors. 11 (2011) 11112–11121. doi:10.3390/s111211112.

[16] S.K. Bhardwaj, N. Bhardwaj, M. Kukkar, A.L. Sharma, K.H. Kim, A. Deep, Formation of high-purity indium oxide nanoparticles and their application to sensitive detection of ammonia, Sensors (Switzerland). 15 (2015) 31930–31938. doi:10.3390/s151229895.

[17] I. Jiménez, M. a. Centeno, R. Scotti, F. Morazzoni, A. Cornet, J.R. Morante, NH3 Interaction with Catalytically Modified Nano-WO3 Powders for Gas Sensing Applications, J. Electrochem. Soc. 150 (2003) H72. doi:10.1149/1.1556055.

[18] I. Jiménez, M.A. Centeno, R. Scotti, F. Morazzoni, J. Arbiol, A. Cornet, et al., NH3 interaction with chromium-doped WO3 nanocrystalline powders for gas sensing applications, J. Mater. Chem. 14 (2004) 2412. doi:10.1039/b400872c.

[19] B. Karunagaran, P. Uthirakumar, S.J. Chung, S. Velumani, E.-K. Suh, TiO2 thin film gas sensor for monitoring ammonia, Mater. Charact. 58 (2007) 680–684. doi:10.1016/j.matchar.2006.11.007.

[20] D. Biskupski, B. Herbig, G. Schottner, R. Moos, Nanosized titania derived from a novel sol–gel process for ammonia gas sensor applications, Sensors Actuators B Chem. 153 (2011) 329–334. doi:http://dx.doi.org/10.1016/j.snb.2010.10.029.

[21] Y. Takao, High Ammonia Sensitive Semiconductor Gas Sensors with Double-Layer Structure and Interface Electrodes, J. Electrochem. Soc. 141 (1994) 1028. doi:10.1149/1.2054836.

[22] M. de Boer, H.M. Huisman, R.J.M. Mos, R.G. Leliveld, a. J. van Dillen, J.W. Geus, Selective oxidation of ammonia to nitrogen over SiO2-supported MoO3 catalysts, Catal. Today. 17 (1993) 189–200. doi:10.1016/0920-5861(93)80023-T.

[23] S. Ahlers, T. Becker, W. Hellmich, C. Braunmühl, G. Müller, Temperature- and Field-Effect-Modulation Techniques for Thin-Film Metal Oxide Gas Sensors, in:

T. Doll (Ed.), Adv. Gas Sens. SE - 6, Springer US, 2003: pp. 123–159. doi:10.1007/978-1-4419-8612-2_6.

[24] S. Chang, Oxygen chemisorption on tin oxide: Correlation between electrical conductivity and EPR measurements, J. Vac. Sci. Technol. 17 (1980) 366. doi:10.1116/1.570389.

[25] J. Puigcorbé, D. Vogel, B. Michel, A. Vilà, I. Gràcia, C. Cané, et al., Thermal and mechanical analysis of micromachined gas sensors, J. Micromechanics Microengineering. 13 (2003) 548–556. doi:10.1088/0960-1317/13/5/304.

[26] N. Yamazoe, K. Shimanoe, Theory of power laws for semiconductor gas sensors, Sensors Actuators, B Chem. 128 (2008) 566–573. doi:10.1016/j.snb.2007.07.036.

[27] N.I. Il'chenko, Catalytic Oxidation of Ammonia, Russ. Chem. Rev. 45 (1976) 1119–1134. doi:10.1070/RC1976v045n12ABEH002765.

[28] V.A. Sadykov, L.A. Isupova, I.A. Zolotarskii, L.N. Bobrova, A.S. Noskov, V.N. Parmon, et al., Oxide catalysts for ammonia oxidation in nitric acid production: properties and perspectives, Appl. Catal. A Gen. 204 (2000) 59–87. doi:10.1016/S0926-860X(00)00506-8.

[29] C.-M. Hung, Decomposition kinetics of ammonia in gaseous stream by a nanoscale copper-cerium bimetallic catalyst, J. Hazard. Mater. 150 (2008) 53–61. doi:10.1016/j.jhazmat.2007.04.044.

[30] K. Skalska, J.S. Miller, S. Ledakowicz, Kinetics of nitric oxide oxidation, Chem. Pap. 64 (2010) 269–272. doi:10.2478/s11696-009-0105-8.

[31] J.D. Prades, R. Jimenez-Diaz, F. Hernandez-Ramirez, S. Barth, A. Cirera, A. Romano-Rodriguez, et al., Ultralow power consumption gas sensors based on self-heated individual nanowires, Appl. Phys. Lett. 93 (2008) 123110. doi:10.1063/1.2988265.

[32] E. Kanazawa, G. Sakai, K. Shimanoe, Y. Kanmura, Y. Teraoka, N. Miura, et al., Metal oxide semiconductor N2O sensor for medical use, Sensors Actuators, B Chem. 77 (2001) 72–77. doi:10.1016/S0925-4005(01)00675-X.

[33] P.T. Moseley, Solid state gas sensors, Meas. Sci. Technol. 8 (1997) 223–237. http://stacks.iop.org/0957-0233/8/i=3/a=003.

[34] S.H. Hahn, N. Bârsan, U. Weimar, S.G. Ejakov, J.H. Visser, R.E. Soltis, CO sensing with SnO2 thick film sensors: Role of oxygen and water vapour, Thin Solid Films. 436 (2003) 17–24. doi:10.1016/S0040-6090(03)00520-0.

[35] D. Koziej, N. Bârsan, U. Weimar, J. Szuber, K. Shimanoe, N. Yamazoe, Water-oxygen interplay on tin dioxide surface: Implication on gas sensing, Chem. Phys. Lett. 410 (2005) 321–323. doi:10.1016/j.cplett.2005.05.107.

[36] N. Barsan, U. Weimar, Understanding the fundamental principles of metal oxide based gas sensors; the example of CO sensing with SnO 2 sensors in the presence of humidity, J. Phys. Condens. Matter. 15 (2003) R813–R839. doi:10.1088/0953-8984/15/20/201.

[37] F. Hernandez-Ramirez, S. Barth, A. Tarancon, O. Casals, E. Pellicer, J. Rodriguez, et al., Water vapor detection with individual tin oxide nanowires., Nanotechnology. 18 (2007) 424016. doi:10.1088/0957-4484/18/42/424016.

[38] G. Heiland, D. Khol, Physical and Chemical Aspects of Oxidic Semiconductor Gas Sensors, Kodansha Ltd, 1988. doi:10.1016/B978-0-444-98901-7.50007-5.

[39] W.S. Epling, C.H.F. Peden, M.A. Henderson, U. Diebold, Evidence for oxygen adatoms on TiO2(110) resulting from O2 dissociation at vacancy sites, Surf. Sci. 412–413 (1998) 333–343. doi:10.1016/S0039-6028(98)00446-4.

[40] M.A. Henderson, W.S. Epling, C.H.F. Peden, C.L. Perkins, Insights into Photoexcited Electron Scavenging Processes on TiO 2 Obtained from Studies of the Reaction of O 2 with OH Groups Adsorbed at Electronic Defects on TiO 2 (110), J. Phys. Chem. B. 107 (2003) 534–545. doi:10.1021/jp0262113.

[41] M.A. Danzon, R. Van Leeuwen, M. Krzyzanowski, Air Quality Guidelines for Europe, World Health Organization, 2nd ed., Copenhagen, 2000.

[42] N. Barsan, U. Weimar, Conduction model of metal oxide gas sensors, J. Electroceramics. 7 (2001) 143–167. doi:10.1023/A:1014405811371.

[43] World Health Organization, WHO Air quality guidelines for particulate matter, ozone, nitrogen dioxide and sulfur dioxide: global update 2005: summary of risk assessment, Geneva World Heal. Organ. (2006) 1–22. http://whqlibdoc.who.int/hq/2006/WHO_SDE_PHE_OEH_06.02_eng.pdf?ua=1.

5. LOW TEMPERATURE SENSOR BASED ON GE NWS LOCALLY GROWN ON SUSPENDED MICROHOTPLATES

Abstract

The gas sensing properties of germanium monocrystalline nanowires (NWs) at temperatures up to 100 ºC have been demonstrated for the first time. The devices have been fabricated based on a site-specific vapour-liquid-solid growth of NW meshes on top of microhotplates. The devices have been investigated for the sensing of different gases. The preadsorbed oxygen is established to be crucial for the interaction with CO. The adsorption of water vapour, however, follows a different mechanism, attributed to a physisorption process and to the presence of phenyl groups at the surface. The different sensing mechanisms are detailed, for which the presence of a stable oxide layer plays a key role and this justifies the requirement of low temperature operation.

5.1. Introduction

Germanium is a semiconductor with a direct bandgap of 0.8 eV that was used more than 60 years ago to create the first transistor [1]. Two decades later, germanium was replaced by silicon because of the feasibility to grow a much more stable and electrically isolating oxide [2] . More recently, Ge has been studied to substitute Si in a niche application because of the higher electron and hole mobility taking advantage of the advances in semiconductor and components processing [3].

Germanium has been scarcely studied as gas sensor due to the difficulties to maintain a stable germanium oxide. The effect of several gases on the germanium surface and the consequent change in electrical resistance were investigated in early studies, which were pioneering for modern resistor-based gas sensing [4,5]. The few works studying Ge surface gas interactions are typically focused on the oxidation of pure germanium surfaces [6]. The chemisorption of oxygen molecules was studied and experimentally observed [7,8], and non-dissociative adsorption has been identified to be involved in the process [9].

More recently, germanium n-type nano-cluster films have been studied as hydrogen and humidity sensors, showing response to water vapour even at room temperature, but no information about the crystalline properties of the material were given [10]. On the other hand, DFT studies carried out on the chemisorption of oxygen at the germanium surface predicted a dissociative chemisorption of the oxygen molecule [11,12]. Thus, charge transfer between oxygen molecules and the germanium surface has been both experimentally observed and theoretically studied in literature. However, to the best of our knowledge, Ge NWs have not been studied in terms of their applicability in gas sensors. The techniques employed to synthesize Ge NWs are similar to those described for silicon and are discussed in detail elsewhere [13,14].

In this chapter, Ge NW-based devices have been fabricated by a Au-seeded process on top of heated microhotplates with integrated top electrodes, as described in chapter 3. The structural characterization of the NWs, with special emphasis on the thin GeO_x shell, has been carried out, since the outer oxide layer plays a key role in the gas adsorption. The electrical response of these devices towards different gases has been studied and sensing mechanisms based on the experimental results, are proposed.

5.2. Experimental details

Microhotplates with buried heaters and top electrodes have been fabricated using surface micromachining. The active area of the devices consists of a Si_3N_4 layer (700 nm thick), in which the platinum heating element is embedded. SiO_2 layers are found on top (400 nm) and below (50 nm) of the Si_3N_4. The microhotplates require 8 mW to achieve a temperature of 200 °C under atmospheric pressure.

The site-specific growth procedure of Ge NWs on top of microhotplates has been described in Chapter 3 of this thesis. As specific experimental details in this chapter, the field effect measurements have been performed using a Keithley 4200 SCS Semiconductor Characterization System, equipped with 3 source and measurement unit (SMU).

5.3. Results and discussion

5.3.1. Structural characterization and conducting behaviour

The Ge NWs are single-crystalline, and grow predominately along the <111> direction of the cubic crystalline lattice, as already presented in chapter 3. After the growth the Ge core of the NWs is surrounded by a very thin amorphous GeO_x shell of around 1 nm (Figure 5.1 c)). The thin germanium oxide layer thickness lies in the same range as other values reported in literature, grown by supercritical-fluid-solid-solid (SFSS) mechanism [15] or by chemical vapour deposition [16].

In order to identify the conduction type of the NWs, field effect transistor (FET) measurements have been performed, for which the upper electrodes of the microhotplate have been used as the source and drain of the transistor, and the buried heater, as a bottom gate electrode (see Figure 5.2Figure 5.2 a)). The thickness of the silicon nitride layer of the suspended membrane is 700 nm, and the SiO_2 layer is 400 nm thick. Although the field effect is quite reduced due to the thick oxide acting as gate oxide (the thickness of the gate oxide in FET devices is usually around 50 nm), the electrical field effect on the Ge NWs is observed under this configuration.

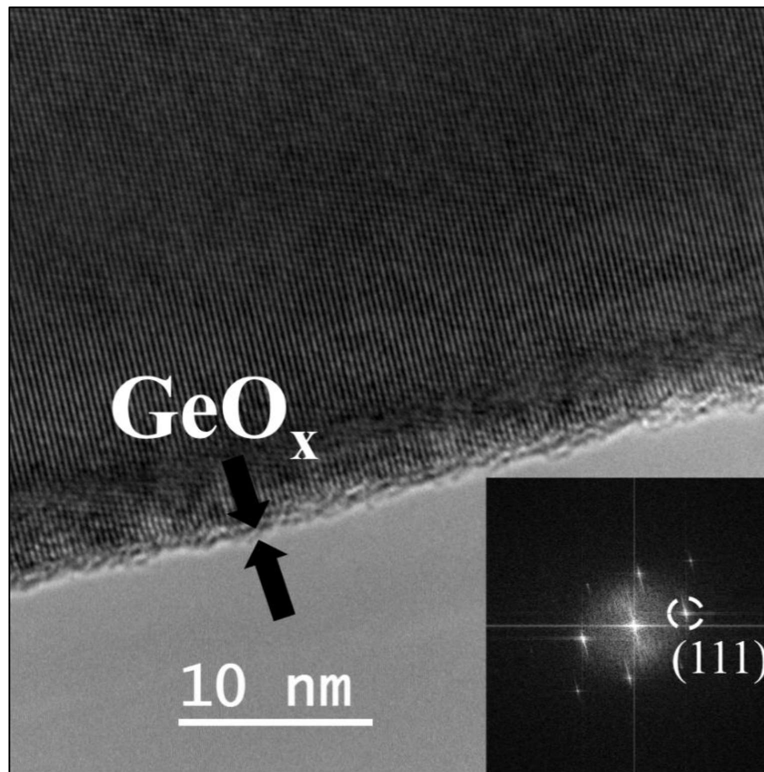

Figure 5.1 HRTEM image of a monocrystalline Ge NW. A thin GeO_x is observed at the surface, highlighted by arrows. Fast Fourier Transform (FFT) is shown in the inset, proving the monocrystalline nature of the NW.

The transfer function of the FET based on the Ge NWs, obtained by varying the gate voltage between -80 and 80 V and measuring the drain-source current forcing V_{DS}=+1 V, is represented in Figure 5.2 c). An increase of the I_{DS} current when negative gate voltages (V_{GS}) are applied, which is shown in the figure, indicates unambiguously a p-type behaviour of the NWs. The Figure 5.2Figure 5.2 b) shows the I-V curve of the Ge NWs at room temperature, i.e., the $I_{DS}(V_{DS})$ with V_{GS}=0 V. An ohmic behaviour is observed, with a resistance of 59.2 kΩ, which has been observed in all the measured sensors.

The $I_{DS}(V_{DS})$ curves obtained at different gate voltages, from -80 to 80 V, are represented in Figure 5.2 d), showing moderate increase of the source-drain current at negative voltages. Note that large gate voltages are used in order to see the field effect on the nanowires, in agreement with the thick “gate” oxide. The 3-dimensional grown nanowire meshes do not have homogeneous contacts nor distances to the gate electrode. This configuration reduces the field effect, as compared to a geometry with a nanowire meshes lying flat on the surface of the microhotplate or single horizontal nanowire

measurements with similar back-gating geometry. Nevertheless, even with this reduced field effect, it is possible to determine the p-type behaviour of the Ge NWs.

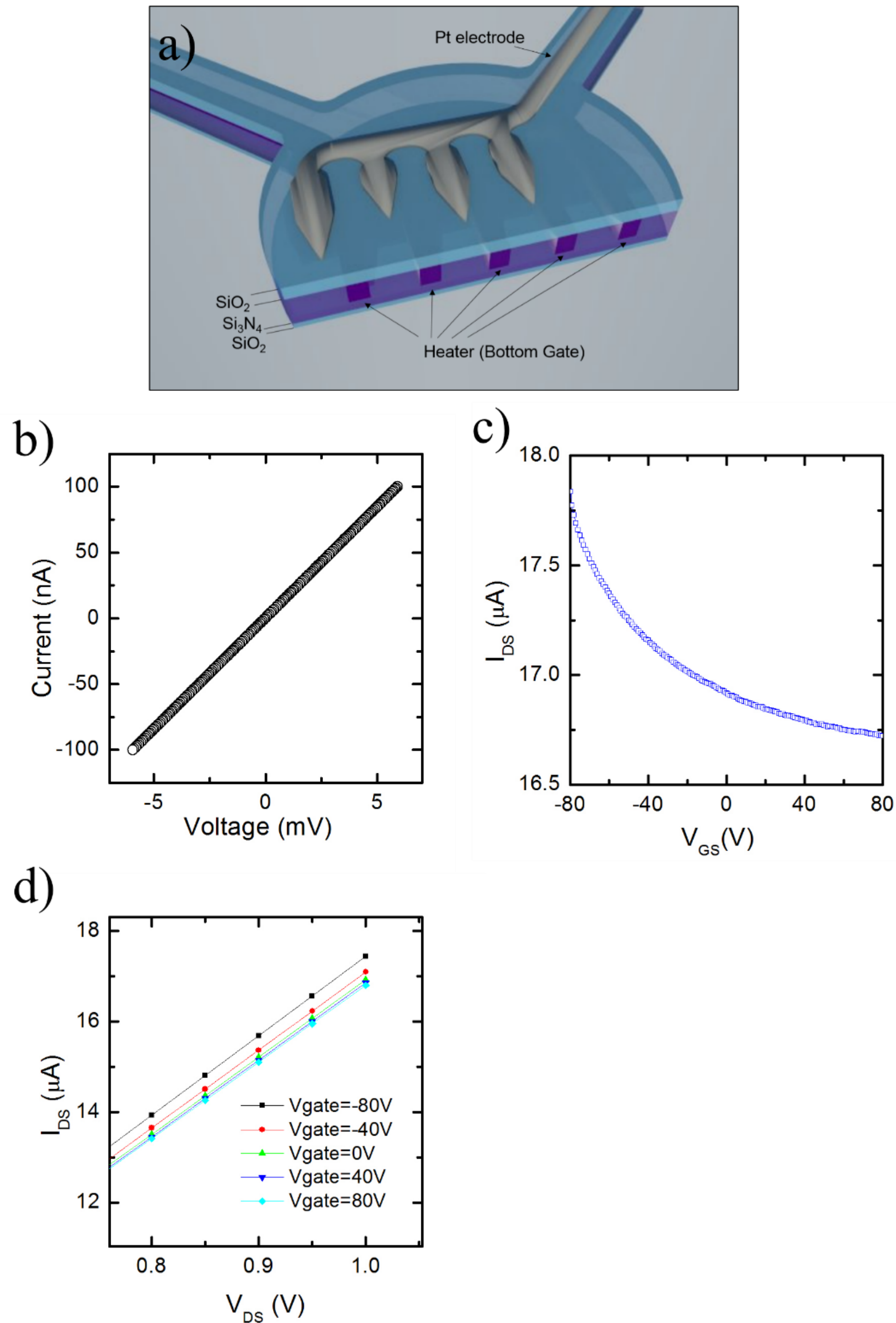

Figure 5.2 a) Scheme of the microhotplate, where the buried heater and the top Pt electrode are observed. The thickness of the SiO_2, Si_3N_4 layers and Pt electrode are not to scale. The electric field effect on Ge NWs on top of microhotplates is obtained using the Pt buried heater as the gate electrode; b) I_{DS}-V_{DS} curve of Ge NWs at room temperature with V_G=0 V; c) Transfer curve of the Ge NWs-based FET. Measurement has been obtained at room temperature applying V_{DS}=+1 V. The drain-source current increases when negative gate voltages are applied, indicating that Ge NWs are p-type; d) Different $I_{DS}(V_{DS})$ curves obtained applying gate voltages from -80 to 80 V. The conduction increases again clearly for negative applied voltages.

The observed conductivity type is in agreement with the catalyst incorporation in the nanowire, which is known to create an impurity level within the bandgap in NWs prepared by different methods [17,19]. Furthermore, Au is expected to behave as electron acceptor in Ge, as reported in [20], providing the p-type semiconductor behaviour.

5.3.2. Determination of the optimal sensing temperature

The first studies carried out in this thesis and aiming at analysing the behaviour of Ge NWs as gas sensors, are focused on elucidating the operating temperature that must be kept in order to obtain a reversible response of the nanowires and to achieve a stable baseline.

The experiments carried out at temperatures above 200 °C towards different gases have shown a severe drift of the resistance baseline, and in some cases, the response towards the gas is reduced for subsequent gas exposures, independently of the gas concentration (see Figure 5.3 as an example). A possible explanation of this behaviour could be the fact that with accumulated oxidizing atmosphere the thickness of the GeOx outer layer increases due to the easy oxidation of the Ge core at that temperature. This would, on the one hand, change the effective section of the Ge channel in the NWs and, on the other, because of the thicker oxide, the charge transfer that might occur at the surface due to the interaction with the gas is hindered because of the thicker barrier. In agreement with this explanation, at temperatures below 200 °C, a more stable baseline is achieved.

As a consequence of this time variation, the evolution and the drift of the resistance of the Ge NWs in air was characterized for 48h at 100 and 150 °C, in order to analyse the time required to reach a dynamic equilibrium at the surface that would assure a stable and reproducible starting point for the measurements.

The first 10 hours of the evolution of the resistance are represented in Figure 5.4 a). The drift observed when Ge NWs are heated to 150 °C is 2% after 48h, calculated from the minimum value of the resistance, which is reached after 2.5 hours of the process (red arrow in the figure). The mentioned drift at 150 ºC is attributed to a further oxidation of the outer GeO_x layer of the NWs at this temperature, but much smaller than at 200 ºC.

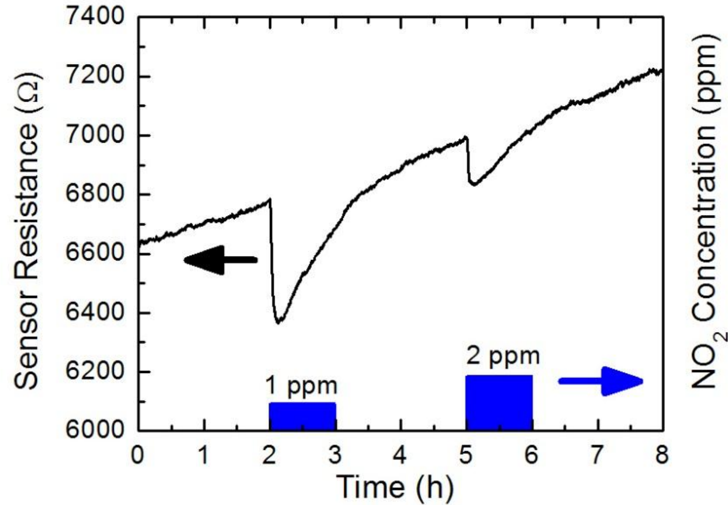

Figure 5.3. Resistance evolution of Ge NWs at 250°C against NO_2 pulses. The resistance shows a severe drift and the changes in resistance are not proportional to NO_2 concentration.

However, while working at 100 ºC, the drift was only 0.1%, calculated by taking as starting point the resistance after 7 hours of the initial decay (black arrow in the figure), which seems to indicate a more stable GeO_x layer arising under these conditions.

As the only modification which can occur is the oxidation, the importance of a stable thickness of germanium oxide in order to obtain a stable and repeatable response is inferred. Since 100°C is found to be the most appropriate operational temperature, the thickness of GeO_x has been experimentally characterized by HRTEM, before and after annealing the nanowires at 100 °C for 1 week in air to simulate the additional oxidation that could occur in the wires while in operation as gas sensors. The results show no post-annealing increase of the GeO_x layer thickness, keeping its value at 1 nm approximately (image not shown). As a consequence of these tests, the maximum operation temperature has been set to 100 °C.

5.3.3. Response to oxidizing species

Once the sensing temperature has been selected, the locally grown Ge nanowires have been studied as a gas sensor towards different oxidizing species.

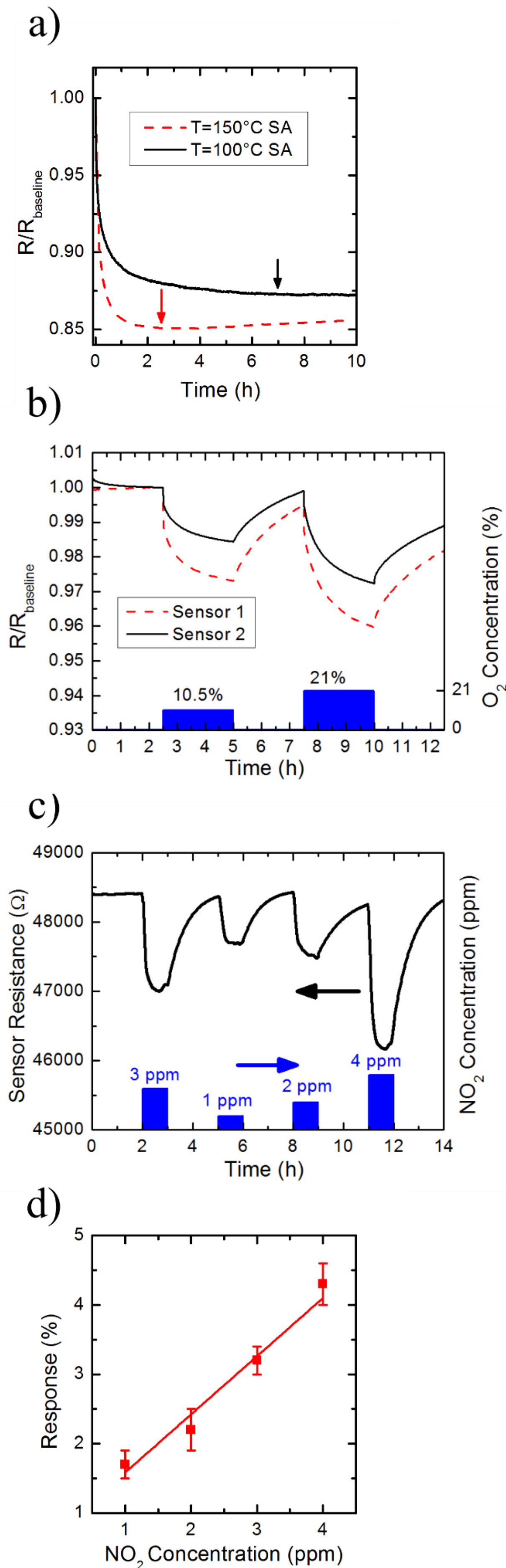

Figure 5.4 a) Stabilization of the resistance keeping 100 °C and 150 °C under synthetic air flow. A drift in resistance is observed after the initial resistance dip when the sensor is kept at 150°C; b) Resistance evolution of two different sensors towards different concentrations of O_2 diluted in nitrogen at 100°C; c) Change in the resistance of Ge NWs towards different pulses of NO_2 in SA at 100 ºC; d) Response of Ge NWs as a function of NO_2 concentration at 100 ºC.

The evolution of the resistance of the device towards different concentrations of oxygen in nitrogen was studied at 100 °C, keeping a constant flow of 200 ml/min, (see Figure 5.4 b)), showing a clear decrease of the resistance in the presence of oxygen, while it increases when oxygen is removed from the test chamber. The transient response towards oxygen is slow, as evidenced by Figure 5.4 b). From this figure, by extrapolating the curve, the oxygen adsorption is estimated to require 6 hours to achieve a steady resistance.

Oxygen, when chemisorbed at the surface of a metal oxide, captures one electron from the semiconductor, giving rise to a negative charge at the surface of the NWs, which causes an upward band bending at the surface. The surface charge causes a resistance change that is opposite for n- or p-type semiconducting gas sensors. The upward bending reduces the majority charge carrier density near the surface in an n-type semiconductor, leading to the creation of a depletion layer of electrons. Therefore, the effective conductive section in the nanowire is reduced, giving as a result the increase of the measured resistance. In the case of a p-type semiconductor, the concentration of majority carriers (holes) is increased at the surface due to the upward band bending, providing a higher conductive layer on the outer part and thus, lowering the resistance [23,24]. Therefore, the observed resistance reduction when oxygen is adsorbed can be accounted by the following reaction:

$$O_{2(g)} + S \leftrightarrow O^{-}_{2(s)} + h^{+} \qquad (5.1)$$

where $O_{2(g)}$ is molecular oxygen, S stands for an adsorption site, $O^{-}_{2(s)}$ for a chemisorbed molecular oxygen at the surface of Ge NWs and h^{+} is a hole generated by charge transfer of an electron to a surface acceptor level.

In order to justify the here-proposed sensing mechanism, the germanium oxide layer must be taken into account. GeO_x covers the surface of the Ge NWs and, necessarily, during the adsorption of gases the charge transfer must take place through it. Stoichiometric germanium oxide GeO_2 is a dielectric with a bandgap of 5.56 eV [25] and, thus, showing a very low conductivity. The GeO_x amorphous layer, for which no reliable electrical data are available, is expected also to be a dielectric, with an electric behaviour somewhere in between Ge and GeO_2. Since the current measured in the devices necessarily passes through the Ge core of the NW, the resistance change observed should be the result of the interaction between chemisorbed molecules and the

charge carriers from the Ge core. This is a plausible situation due to the reduced GeO_x thickness, of only 1 nm.

The response of the device at 100 °C towards another oxidizing gas, NO_2, is represented in Figure 5.4 c), where, again, a clear decrease of the device's resistance in the presence of this gas is observed. The response towards nitrogen dioxide is visibly faster than that caused by the oxygen adsorption. The proposed sensing mechanism for nitrogen dioxide does not involve ionosorbed oxygen and is described according to the reaction [26]:

$$NO_{2(g)} + S \leftrightarrow NO_{2(s)}^{-} + h^{+} \quad (5.2)$$

where S stands for an adsorption site and $NO_{2(s)}^{-}$, for a chemisorbed NO_2 molecule at the surface of Ge NWs. In this mechanism nitrogen dioxide plays a similar role to that of the ionosorbed oxygen in equation (5.1), giving rise to the negative charge accumulation at the surface of the GeO_x layer and, subsequently, to the upward band bending at the surface.

The response towards NO_2 is defined according to the following equation:

$$Response(\%) = \frac{R_{ox} - R_{air}}{R_{air}} \cdot 100 \quad (5.3)$$

where R_{ox} is the resistance of the device in the presence of the oxidizing gas and R_{air}, the reference value in dry synthetic air. The measured response to NO_2 concentrations up to 4 ppm is within 5%, as shown in Figure 5.4 d).

5.3.4. Response to reducing gases

The sensing of a metal oxide at temperatures above 200 °C in the presence of reducing species, like NH_3 and CO, is known to undergo through the interaction with pre-adsorbed oxygen. In order to evaluate if Ge NWs exhibits a similar mechanism, the sensing behaviour towards carbon monoxide (CO) diluted either in dry synthetic air (SA) or in nitrogen has been studied. In both cases, the tests have been performed at operating temperatures between 75 and 100 °C. The evolution of the resistance of the device is shown in Figure 5.5 a). The decrease in resistance for the higher temperature is evidenced by the behaviour in SA at 75 and 100ºC, as is expected for a semiconductor.

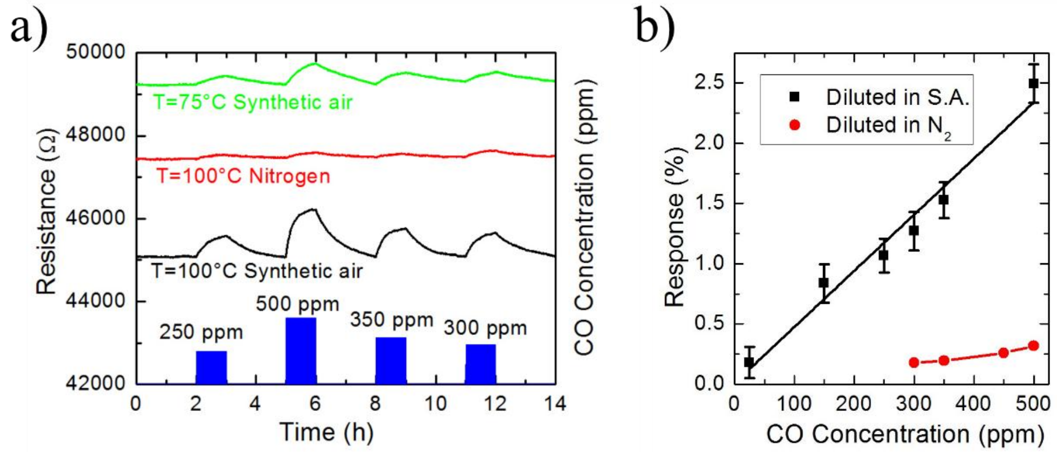

Figure 5.5 a) Evolution of the resistance of Ge NWs against different concentrations of CO diluted in synthetic air at 75 and 100 °C, and diluted in nitrogen at 100 °C. Clearly, the response towards CO in nitrogen is reduced; b) Response of Ge NWs as a function of CO concentration in SA and nitrogen, both measured at 100 °C.

Furthermore, at 100 °C, the resistance in nitrogen is higher than in synthetic air, in agreement with the observed resistance decrease in the presence of oxygen. In this figure, the response towards CO in synthetic air can be clearly observed, while it is almost suppressed when CO is diluted in N_2.

In the case of a p-type metal oxide semiconducting sensor, the accepted sensing mechanism in the presence of CO is due to the oxidation of the CO molecule by one ionosorbed oxygen molecule O_2^-, reducing the negative charge at the surface and giving CO_2 as a result [23]:

$$2CO_{(g)} + O^-_{2(s)} + h^+ \leftrightarrow 2CO_{2(g)} + S \quad (5.4)$$

This process, in opposition to the response to oxygen, reduces the above-mentioned band bending, decreasing the hole density near the surface and, thus, gives rise to an increase of the resistance. This is the expected behaviour for p-type semiconductors in the presence of a reducing gas that requires pre-adsorbed oxygen for its sensing mechanism. The mechanism (5.4), thus, accounts for the observed response of the Ge NWs-based device towards CO.

When the device is exposed to CO diluted in nitrogen, because no replacement of the desorbed oxygen molecules occurs, a strong lowering of the response of the NWs towards CO is expected. This is evidenced in the red line in Figure 5.5 a), where almost no variation of the resistance to different concentrations of CO can be observed. The non-zero variation observed in the figure may be due to residual oxygen traces coming

from the CO/N_2 gas bottle, nominally below 5 part per million (ppm), providing in a continuous manner a very low level of molecular oxygen during the sensor measurements. These experiments confirm that oxygen molecules are required for the CO sensing mechanism of Ge NWs, which is consistent with the model accepted for metal oxide gas sensors.

In general, the response against a reducing gas is obtained according to the following equation:

$$Response(\%) = \frac{R_{air} - R_{red}}{R_{air}} \cdot 100 \quad (5.5)$$

where R_{red} is the resistance of the device in the presence of the reducing gas and R_{air}, the reference value in dry synthetic air. The values of the response against CO are found to be in the range between 0.25 and 2.5% for concentrations between 25 and 500 ppm (Figure 5.5 b)).

Water vapour is another reducing gas whose effect on the device's resistance has been studied. This is shown in Figure 5.6Figure 5.5 a), whose measurement is obtained operating at a temperature of 100 ºC. Alternated pulses of dry and humid air, with different relative humidity (RH) levels, are introduced into the gas test chamber. The figure clearly reveals the repeatability of the measurements and the fact that the baseline is recovered after each measurement. The shortest measured response time is 10 min for the highest RH employed (80%). The response shown by the sensor is represented in in Figure 5.6Figure 5.5 b).

Furthermore, in order to analyze the role of oxygen in the adsorption of water vapor, the response towards different concentrations of water vapor diluted in nitrogen and air at 100°C has been studied. Figure 5.6 c) shows the resistance changes in Ge NW devices upon exposure to different relative humidity values. The overall responses are very similar in both atmospheres, besides an offset of the baseline caused by the oxygen adsorption. This independence of the response on the oxygen partial pressure indicates that oxygen plays a negligible role on the adsorption of water vapor molecules.

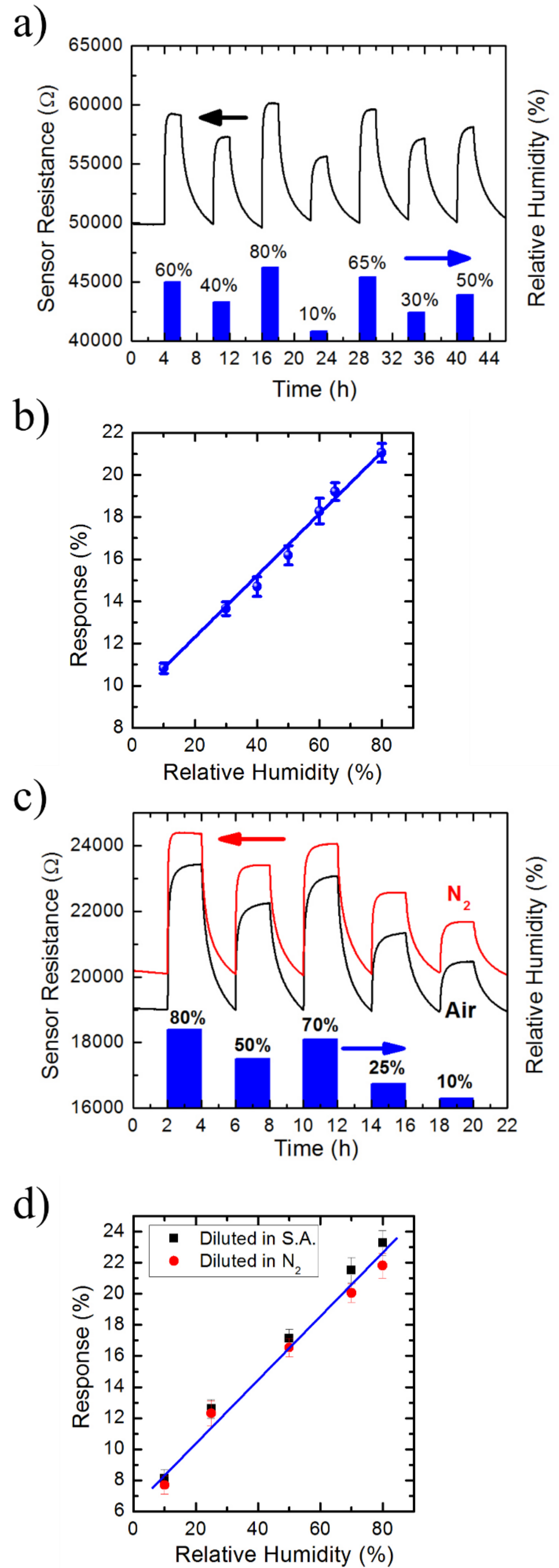

Figure 5.6. a) Change in resistance of Ge NWs towards different pulses of water vapour at 100 °C. The water vapour concentration is expressed in terms of relative humidity; b) Response of the Ge NWs towards relative humidity in synthetic air; c) Different transient responses of Ge NWs towards several pulses of water, diluted in nitrogen and synthetic air, obtained holding a temperature of 100°C; d) Response as a function of relative humidity obtained in nitrogen and synthetic air at 100°C.

The initial baseline is recovered when switching back and forth from nitrogen or synthetic air and operating the device to detect humidity levels. The obtained response is shown in Figure 5.6 b). Note that the resistance as a fundamental baseline differs from device to device.

The sensing behavior towards water vapor at temperatures above 200°C is generally accepted in metal oxide to involve the formation of hydroxyl groups [27,28]. Furthermore, the chemisorbed oxygen has been observed to interfere with water vapor, providing higher response towards H_2O in air than in nitrogen flow, as illustrated for the case of SnO_2 [27]. However, the here presented results depict a different mechanism, as a result of the low temperature employed during the tests (100°C). Water vapor does not react with chemisorbed oxygen, and both do not compete for the same adsorption sites. The latter is confirmed by the fact that the response towards water vapor is the same in both nitrogen and synthetic air, with the only difference being the shift in the signal due to the chemisorbed oxygen.

On one hand, the formation of OH groups is highly unlikely, since it involves the oxidation/reduction of the surface that at that 100 ºC is almost no promoted, which cannot give as a results the high response observed.

Hence, a plausible explanation would be that the sensing mechanism is attributed to separated charges in the adsorbed water vapor molecules, in the form of electric dipoles. Our hypothesis is that the adsorption of these dipoles takes place at the surface with the hydrogen from the dipolar H_2O molecules pointing towards the oxide. This configuration is rather unusual; however, organic groups from the precursor can still partially reside on the surface of Ge nanowires after the growth [29], and in our case the electron-rich phenyl groups could lead to the described orientation of the water dipole. As a consequence, the majority carriers in the Ge core experience higher repulsion effect from the closer hydrogen atoms (positive charge) than attraction coming from the farther oxygen atom (negative charge). This leads to a narrowing of the Ge NW conduction effective section, giving as a result the increase of the resistance. Since the conductivity changes are almost identical in nitrogen and synthetic air, water adsorption should predominantly take place at the surface not covered by oxygen, noticing no interaction with oxygen.

Table 5.1 Response of Ge NW-based devices towards different gas concentrations obtained at 100 °C in synthetic air, and the recommended exposure limit by WHO.

Gas concentration (ppm)	**Response (%)**	**Recommended exposure limit by WHO**
150 ppm CO	0.8	8.6 ppm (8 h exposure CO)
1 ppm NO_2	1.7	210 ppb (24 h exposure NO_2)
10% RH	10.8	-
80% RH	21.0	-

5.3.5. Gas selectivity and sensing mechanisms

The summary of the response of the Ge NWs to certain gas concentrations of the previously analysed gases is given in Table 5.1, which proves that the response towards water vapour is the dominant one. For practical applications, one has to bear in mind that the recommended exposure limit by the World Health Organization are 8.6 ppm (8 hours exposure) for CO and 210 part per billion (ppb) (24 hours exposure) for NO_2 [30,31] and that the two values indicated in the table are beyond these limits. When extrapolating the linear dependences shown for these two gases to the mentioned exposure limits, the response of the sensors would be of about 0.1 and 0.8%, respectively. The response to water vapour, on the other hand, is in the range of several %. This assures that for relevant outdoor environments the response of the gas sensor towards water vapour will be dominant. Even a variation of the oxygen concentration in the atmosphere would only give rise to a small variation in the resistance of the device, since the complete removal of oxygen leads to a change of a 5%, approximately, of the baseline (see Figure 5.4 b)).

A result to notice is that, within the limited gas concentrations measured in this work, the sensing response of the Ge NW-based devices towards CO, NO_2 and water vapor shows a linear dependence on the concentration, which simplifies the interpretation of the dependence between the resistance changes and the gas concentration measured.

The fact that the Ge NWs are surrounded by a thin GeO_x shell plays a key role in the sensors properties. The uniform thickness will ensure a stable response when using the nanostructures as gas sensor and will control the charge transfer between the core of the nanowire and the surface of the oxide described in the different sensing mechanisms because of the strong isolating character of GeO_x. Changes in the composition and thickness of the surface layer as a result of the further oxidation of the NWs surface would result in drastic changes in the charge transfer characteristics and the resistance, leading to non-reproducible and drifting sensing responses, similar to what has been observed when the sensor is kept at temperatures in excess of 200 ºC. Since these effects are not observed in our measurements, we conclude that there is no further alteration in the materials composition under the given experimental conditions. For this reason, all the sensing experiments have been carried out at temperatures up to 100ºC. The fact that the Ge-NWs show p-type conductivity further supports the GeO_x layer uniformity, as it has been experimentally observed by X-Ray photoelectron spectroscopy that n-type Ge NWs are more easily oxidized than p-type, first to GeO, and, afterwards, to GeO_2 [32].

Furthermore, residual surface termination is inferred from the negligible interaction of oxygen in the adsorption of water. The partial blocking of surface adsorption sites by hydrocarbon groups can explain the low response observed towards other reducing or oxidizing species that require chemisorbed oxygen or available adsorption sites. Adsorption of water vapor, however, can be described by a physisorption process that would be ruled by the presence of phenyl groups at these temperatures.

An alteration or removal of the germanium oxide layer due to the condensation of water and subsequent dissolution of the oxide on the surface should not occur because the temperature difference of the environment and the sensor surface is higher than 50°C. Detailed investigations on the exact surface termination and also density of organic groups are part of future studies in this system.

5.4. Conclusions

Ge NWs have been energy efficiently grown via the vapour-liquid-solid method on specific locations on top of microhotplates that contain electrodes on their surface. This strategy allows overcoming one of the critical steps in the fabrication of nanowire-based

devices, the integration/contacting issue. P-type semiconducting behaviour, expected for the employed fabrication route, has been proven for the Ge NWs.

The resulting devices have been tested for the first time to the best of our knowledge as gas sensors towards oxygen, CO, NO_2 and water vapour, showing stable and reproducible responses at low temperatures, up to 100 ºC. High response is obtained for water vapour, while for the other gases the resistance variation is small, providing gas selectivity to the devices. Sensing mechanisms have been proposed for the studied gases, which, for the case of oxygen, CO and NO_2 are similar to those reported for other p-type semiconductor gas sensors. The mechanism against water dipoles is different, taking place as a physisorption process, attributed to the presence of phenyl groups at the surface. In these Ge NW-based devices, the 1 nm thick native GeO_x layer surrounding the nanowires plays a key role in the sensing processes, providing the reaction sites for the different gas species and allowing the charge transfer from the semiconductor. The chemical stability of this oxide, even in the presence of large amounts of water vapour, assures the repeatability of the measurements.

5.5. References

[1] J. Bardeen, W.H. Brattain, The Transistor, A Semi-Conductor Triode, Phys. Rev. 74 (1948) 230–231. http://link.aps.org/doi/10.1103/PhysRev.74.230.

[2] S.F. Bent, Chapter 5 - Semiconductor Surface Chemistry, in: A. Nilsson, L.G.M. Pettersson, J.K. Nørskov (Eds.), Chem. Bond. Surfaces Interfaces, Elsevier, Amsterdam, 2008: pp. 323–395. doi:http://dx.doi.org/10.1016/B978-044452837-7.50006-X.

[3] A. Dimoulas, G. Mavrou, G. Vellianitis, E. Evangelou, N. Boukos, M. Houssa, et al., HfO2 high- K gate dielectrics on Ge (100) by atomic oxygen beam deposition, Appl. Phys. Lett. 86 (2005) 1–3. doi:10.1063/1.1854195.

[4] M.J. Sparnaay, A.H. Boonstra, J. Van Ruler, The influence of chemisorption upon the electrical properties of germanium surfaces, Surf. Sci. 2 (1964) 56–63. doi:http://dx.doi.org/10.1016/0039-6028(64)90043-3.

[5] M. Lasser, C. Wysocki, B. Bernstein, Effects of Thick Oxides on Germanium Surface Properties, Phys. Rev. 105 (1957) 491–494. http://link.aps.org/doi/10.1103/PhysRev.105.491.

[6] L. Surnev, M. Tikhov, Oxygen adsorption on a Ge(100) surface: I. Clean surfaces, Surf. Sci. 123 (1982) 505–518. doi:http://dx.doi.org/10.1016/0039-6028(82)90343-0.

[7] D.A. Hansen, J.B. Hudson, Oxygen scattering and initial chemisorption probability on Ge(100), Surf. Sci. 254 (1991) 222–234. doi:http://dx.doi.org/10.1016/0039-6028(91)90655-C.

[8] D.A. Hansen, J.B. Hudson, The adsorption kinetics of molecular oxygen and the desorption kinetics of GeO on Ge(100), Surf. Sci. 292 (1993) 17–32. doi:http://dx.doi.org/10.1016/0039-6028(93)90387-Y.

[9] X.L. Fan, W.M. Lau, Z.F. Liu, Nondissociative Adsorption of O2 on Ge(100), J. Phys. Chem. C. 113 (2009) 8786–8793. doi:10.1021/jp809480c.

[10] D.M.A. Mackenzie, S.A. Brown, Germanium nano-cluster films as humidity and hydrogen sensors, J. Appl. Phys. 112 (2012) 74514. doi:http://dx.doi.org/10.1063/1.4758284.

[11] J.M. Soon, C.W. Lim, K.P. Loh, N.L. Ma, P. Wu, Initial-stage oxidation mechanism of Ge(100)2×1 dimers, Phys. Rev. B - Condens. Matter Mater. Phys. 72 (2005) 1–6. doi:10.1103/PhysRevB.72.115343.

[12] G.A. Shah, M.W. Radny, P. V Smith, Initial Stages of Oxygen Chemisorption on the Ge(001) Surface, J. Phys. Chem. C. 118 (2014) 15795–15803. doi:10.1021/jp503541n.

[13] L.Z.P. and Z.Y. Cai, A Review on Germanium Nanowires, Recent Pat. Nanotechnol. 6 (2012) 44–59. doi:http://dx.doi.org/10.2174/187221012798109291.

[14] S. Barth, F. Hernandez-Ramirez, J.D. Holmes, A. Romano-Rodriguez, Synthesis and applications of one-dimensional semiconductors, Prog. Mater. Sci. 55 (2010) 563–627. doi:10.1016/j.pmatsci.2010.02.001.

[15] S. Barth, M.M. Koleśnik, K. Donegan, V. Krstić, J.D. Holmes, Diameter-controlled solid-phase seeding of germanium nanowires: Structural characterization and electrical transport properties, Chem. Mater. 23 (2011) 3335–3340. doi:10.1021/cm200646e.

[16] P. Nguyen, H.T. Ng, M. Meyyappan, Growth of individual vertical germanium nanowires, Adv. Mater. 17 (2005) 549–553. doi:10.1002/adma.200400908.

[17] J.M. Redwing, X. Miao, X. Li, 9 - Vapor-Liquid-Solid Growth of Semiconductor Nanowires, in: T.F. Kuech (Ed.), Handb. Cryst. Growth (Second Ed., Second Edi, North-Holland, Boston, 2015: pp. 399–439. doi:http://dx.doi.org/10.1016/B978-0-444-63304-0.00009-3.

[18] J. Greil, S. Birner, E. Bertagnolli, A. Lugstein, Nanowires enabling strained photovoltaics, Appl. Phys. Lett. 104 (2014) 2012–2016. doi:10.1063/1.4871458.

[19] G. Collins, M. Koleśnik, V. Krstić, J.D. Holmes, Germanium nanowire synthesis from fluorothiolate-capped gold nanoparticles in supercritical carbon dioxide, Chem. Mater. 22 (2010) 5235–5243. doi:10.1021/cm1012137.

[20] W.C. Dunlap, Gold as an Acceptor in Germanium, Phys. Rev. 97 (1955) 614–629. doi:10.1103/PhysRev.97.614.

[21] Z.M. Jarzebski, J.P. Marton, Physical Properties of SnO2 Materials: II . Electrical Properties, J. Electrochem. Soc. 123 (1976) 299C–310C. doi:10.1149/1.2133090.

[22] K.G. Godinho, A. Walsh, G.W. Watson, Energetic and Electronic Structure Analysis of Intrinsic Defects in SnO2, J. Phys. Chem. C. 113 (2009) 439–448.

[23] M. Hübner, C.E. Simion, A. Tomescu-Stănoiu, S. Pokhrel, N. Bârsan, U. Weimar, Influence of humidity on CO sensing with p-type CuO thick film gas sensors, Sensors Actuators B Chem. 153 (2011) 347–353. doi:10.1016/j.snb.2010.10.046.

[24] P.T. Moseley, Solid state gas sensors, Meas. Sci. Technol. 8 (1997) 223–237. http://stacks.iop.org/0957-0233/8/i=3/a=003.

[25] N.M. Ravindra, R.A. Weeks, D.L. Kinser, Optical properties of GeO2, Phys. Rev. B. 36 (1987) 6132–6134. http://link.aps.org/doi/10.1103/PhysRevB.36.6132.

[26] B.J. Hansen, N. Kouklin, G. Lu, I.K. Lin, J. Chen, X. Zhang, Transport, analyte detection, and opto-electronic response of p-type CuO nanowires, J. Phys. Chem. C. 114 (2010) 2440–2447. doi:10.1021/jp908850j.

[27] F. Hernandez-Ramirez, S. Barth, A. Tarancon, O. Casals, E. Pellicer, J. Rodriguez, et al., Water vapor detection with individual tin oxide nanowires., Nanotechnology. 18 (2007) 424016. doi:10.1088/0957-4484/18/42/424016.

[28] D. Koziej, N. Bârsan, U. Weimar, J. Szuber, K. Shimanoe, N. Yamazoe, Water-oxygen interplay on tin dioxide surface: Implication on gas sensing, Chem. Phys. Lett. 410 (2005) 321–323. doi:10.1016/j.cplett.2005.05.107.

[29] T. Hanrath, B.A. Korgel, Chemical Surface Passivation of Ge Nanowires, J. Am. Chem. Soc. 126 (2004) 15466–15472. doi:10.1021/ja0465808.

[30] World Health Organization, Environmental health criteria 13: Carbon monoxide, Environ. Int. (1999). http://apps.who.int/iris/bitstream/10665/42180/1/WHO_EHC_213.pdf.

[31] World Health Organization, WHO Air quality guidelines for particulate matter, ozone, nitrogen dioxide and sulfur dioxide: global update 2005: summary of risk assessment, Geneva World Heal. Organ. (2006) 1–22. http://whqlibdoc.who.int/hq/2006/WHO_SDE_PHE_OEH_06.02_eng.pdf?ua=1.

[32] D. Wang, H. Dai, Germanium nanowires: From synthesis, surface chemistry, and assembly to devices, Appl. Phys. A Mater. Sci. Process. 85 (2006) 217–225. doi:10.1007/s00339-006-3704-z.

6. INDIVIDUAL SnO_2 NWS CONTACTED BY EBL

Abstract

A new methodology based on the use of Electron Beam Lithography for contacting individual nanowires on top of micromembranes and microhotplates has been developed. The different experimental steps, as the spin-coating of PMMA resist, electron exposure, and metallization of the patterned structures have been analysed and optimized. Furthermore, the fabrication and characterization of functional nanodevices have been demonstrated with prototypes of single nanowire-based gas sensors that show a reversible and remarkable response towards NH_3 and NO_2.

6.1 Introduction

The requirement of high surface to volume ratio leads to the use of the nanowires as an optimal active material form in gas sensing. Gas sensors based on individual nanowires, on the other hand, allow to study and analyse the specific material response and the involved kinetics towards a gas, due to the well-defined surface and geometry of the nanowire [1]. Further benefit of such morphology is its considerably lower power consumption as compared to their bulk counterpart, attainable by an adequate device layout, allowing to match the limits required in mobile gas sensing applications [2].

Dual-beam systems has been demonstrated as successful approach for contacting indivudla nanowires [3,4]. However, the technique is highly time consuming and requires several hours for contacting one single nanowire. Additionally, the Pt/C contacts importantly contribute to the overall resistance, due to the carbon content of the organometallic precursor.

EBL appears, thus, as an alternative for the fabrication of nano-contacts to the nanostructures. Electron Beam Lithography, as a pattern transferring process, is nowadays, one of the fundamental techniques of nanofabrication. It is used in very different fields for fabrication of transistors, metallic tunnelling junctions or photonic crystals [5]. EBL has been used, besides, for fabricating gas sensors based on nano-trenches by etching TiO_2 [6], SnO_2 [7] or Pd films [8], among others. The reported works, however, deal with multiple polycrystalline nanostructures, instead of a single one, and the process fabrication limits severely the wideness of the structures, which is higher than 200 nm. EBL is also employed for contacting individual nanowires, in order to fabricate field effect transistors using the nanowire as a channel [9-11].

Few works are found, however, for resistive gas sensor purposes instead of a FET configuration. In these works, the process is performed on top of bulk substrates with no suspended structures and without an embedded microheater [12-14], i.e., the final devices either work at room temperature or are externally heated, which involves higher power consumption. At the best of our knowledge, this is the first time that nanowires are contacted on top of a microhotplate using this method for gas sensing purposes.

The aim of this chapter, thus, is the development of a new method for fabricating gas sensors based on single nanowire, by means of Electron Beam Lithography, that

allows to overcome some drawbacks present in the Dual Beam approach. The main issues are the reduction of the required time for the contact fabrication, since the process allows to mount different substrates on the same support, and the fabrication of more conductive metal lines and contacts with a lower Schottky barrier.

Tin dioxide nanowires have been chosen for this new approach, since among metal oxides, SnO_2 is one of the preferred materials due to the easy fabrication technology, good crystallographic properties, good sensitivity and well known sensing interactions [15]. Furthermore, individual SnO_2 one-dimensional nanostructures have been already characterized, being suitable to be compared to our previous works.

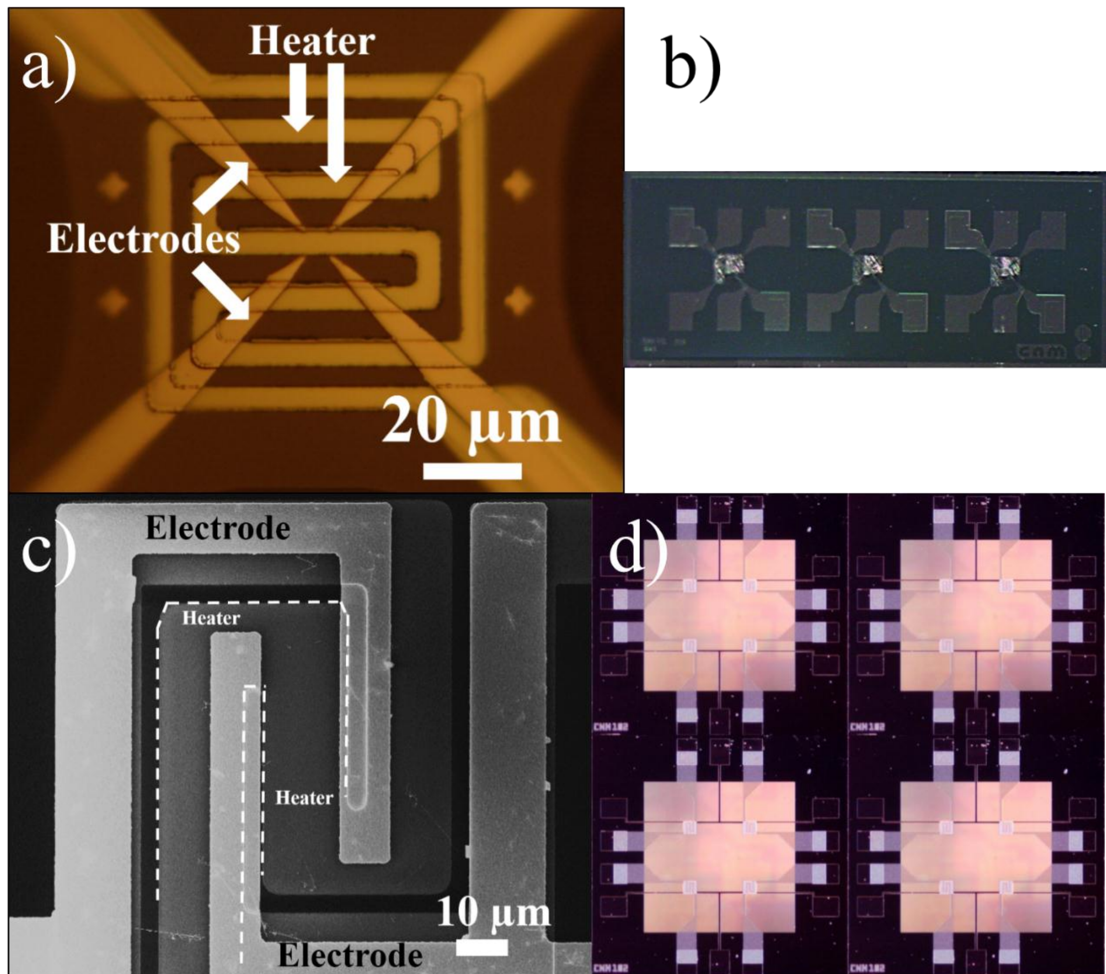

Figure 6.1 a) Optical image of the suspended microhotplate; b) General view of the chip, which includes 3 microhotplates; c) SEM image of one of the micromembranes, with a distance of 10 µm between the electrodes d) General view of the chip with 16 micromembranes. Both chips have been employed for contacting individual nanowires by means of EBL.

6.2 Experimental details

As already explained in chapter 2, tin dioxide nanowires are grown by a CVD process in a cold-wall quartz reactor in which a high-frequency field is used inductively to heat the substrates (Si or Al_2O_3) by placing them on a graphite susceptor. The chamber temperature is kept at around 700°C and the process is catalysed by a Au layer of 3-5 nm thickness that forms nanoclusters when temperature is raised. The precursor used is $Sn(OtBu)_4$, which is introduced into the chamber in the gas phase, and decomposed on Au nanoclusters. More details on the growth of nanowires are given elsewhere [16].

The fabrication of the electrical nanosized contacts of the individual nanowires has been performed onto two different types of substrate: suspended microhotplates with alignment marks, whose optical image is shown in Figure 6.1 a), and micromembranes with a space between the electrodes of 100 µm (see Figure 6.1 b)). The details of the layer structure and the materials used for the fabrication of this type of substrates are described in section 2.5 of this dissertation. The deposition of NWs on top of the substrate and the design of the shape and the size of the contacts for the NWs are explained in section 2.4.2

6.2.1 Uniformity of PMMA coating on chips

The spin-coating of PMMA resist on top of the chips is an important step of the overall process, since the uniformity of the thickness of the resist depends on it. A non-desired effect caused by the spin-coating is the so-called edge effect, which involves a small bead of coating thickness difference around the rim of the substrate. Since the fluid flows uniformly outwards, depending on the surface tension, viscosity of the solvent, and rotation rate, the edges of the chip may present a thicker coating.

Therefore, the sizes of the chips are a relevant issue, since smaller chips may have an important part of the surface affected by the edge effect. The chips containing the microhotplates have a size of 1.2x3.4 mm^2, and the chips with micromembranes have dimensions of 3x3 mm^2. Usually, in order to achieve a uniform resist thickness that is not affected by the surface tension occurring at the edges of the substrate during the spin-coating, relatively large samples of at least 2x2 cm^2 are required. However, due to

the limitations imposed by the wire-bonding of the chips onto TO-8 holders, which only accept chips of size below 1x1 cm^2, and to the fact that for each membrane or hotplate we have to bond 4 or 6 wires and the TO-8 holder has 12 pins, we can only work with chips of the size indicated above.

Thus, in order to reduce the edge effect, a stainless steel holder for the chips was designed and fabricated, which fits into the spin-coater. The upper surface of the chip and of the holder lie at the same height and, thus, the resist can be extended over the surface of the holder in a manner that the edge effects will only appear at the edges of the stainless steel holder (see Figure 6.2). Two rectangular pieces are screwed to the base of the holder, which embed the chip and fix it robustly. The edge effects in the chip are strongly reduced by this procedure; therefore, it has been used to fabricate the nano-contacts that will be described in this chapter.

Furthermore, the roughness of the surface of the chips affects the uniformity of the PMMA coating, since a *valley* in the surface may induce a thicker area of PMMA. In general, thicker layers of PMMA require higher electron acceleration voltages and doses for a complete exposure, which induces to a more important proximity effect, reducing the final resolution of the defined patterns.

Therefore, the roughness profile of the suspended microhotplates has been studied by confocal microscopy. The whole chip was covered with a Au layer with a thickness of approximately 10 nm because the SiO_2 layer on the suspended membrane does not reflect the white light employed by the microscope, and thus, the sample cannot be observed by the technique.

Figure 6.2. Image of the holder used to extend the effective area at which the resist is deposited during the spin-coating process

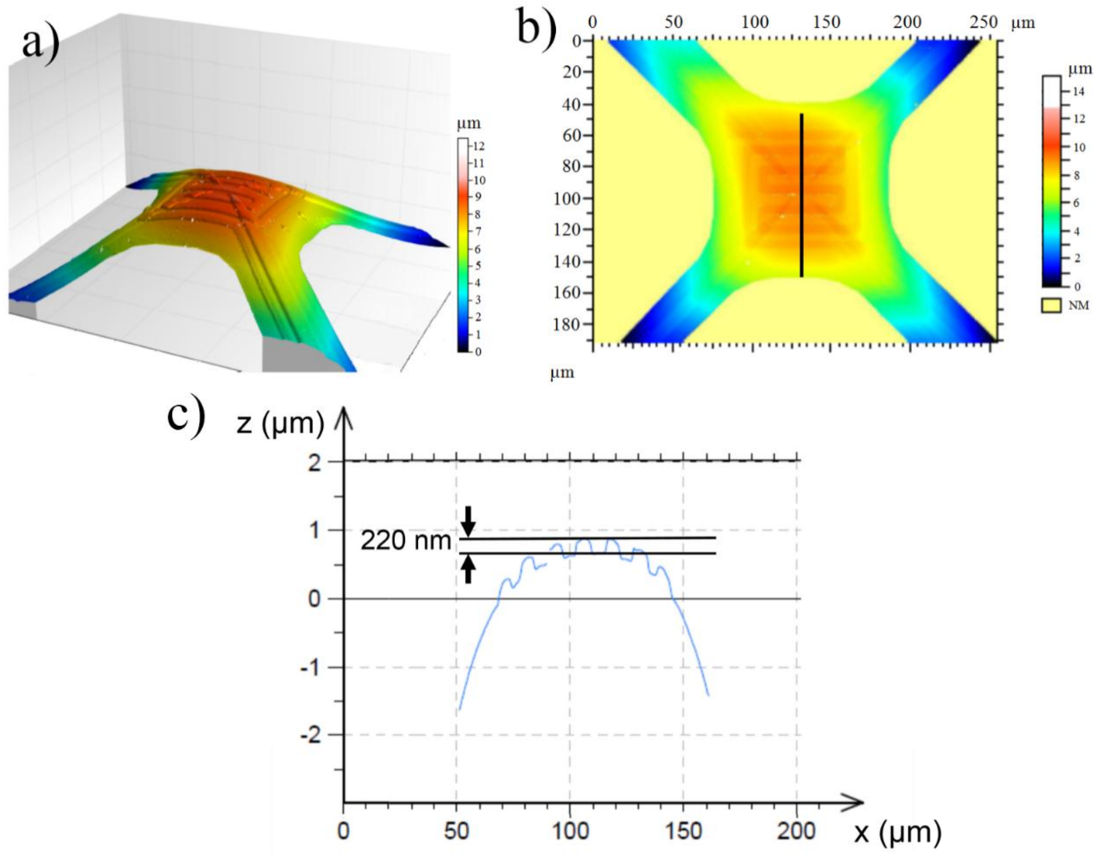

Figure 6.3 a) 3-D image of a suspended microhotplate obtained by confocal microscopy. The central part is bent upward. Note that x-y axes are different from that of the z-axis; b) Topography map of the central part of the membrane, where the heater and electrodes are visible due to the distinct height at which they are found; c) Height profile from the segmented line remarked in b). The prominences observed, of 220 nm height, are due to the heater.

The 3-dimensional image of the topography measurements obtained by confocal microscopy is shown in Figure 6.3 a). Note that the x-y axes are on a different scale than the z axis. The central part of the suspended membrane is bent upward about 10 µm, as it is also visible in the topography mapping represented in Figure 6.3 b), due to mechanical stress that suffers the structure after the bulk micromachining process.

The segmented line in Figure 6.3 b) defines a profile line at the surface of the suspended membrane that is due to the heater, since the interdigitated electrodes do not reach the line. The topography profile is shown in Figure 6.3 c), which is caused by the heater, and supposes a difference in height of 220 nm. Thus, a first picture of the surface of suspended microhotplates is presented, showing non-negligible topography that will affect the PMMA coating profile.

The next step towards the implementation of the process is focused on how the spin-coated PMMA onto suspended micromembranes is affected by the shown topography. The remaining profile of PMMA (950k A7) after being spin-coated on top of a suspended microhotplate has been studied by locally milling the sample in a Dual Beam Focused ion Beam system in order to obtain a cross-section view. A thin Au layer was sputtered before performing the cross-section to facilitate the observation of the PMMA layer edge. The SEM image of the central part of the membrane is shown in Figure 6.4, with the sample tilted by 52°. The picture corresponds to the central from the three membranes that each chip contains. The spin-coating was performed at 4500 rpm for 1 minute and subsequently soft-baked for 1 minute at 180°C. After the spin coating, a 5-10 nm thick Au layer was sputtered on the top of the resist in order to recognize the edge of the PMMA layer (bright zones in the upper part of the picture). At the right part of the picture, the heater and the electrode are clearly seen. The thickness of the PMMA layer on top of the heater region is visibly thinner (between 230 and 290 nm) than in the area with no underlying heater (thickness between 330 and 400 nm).

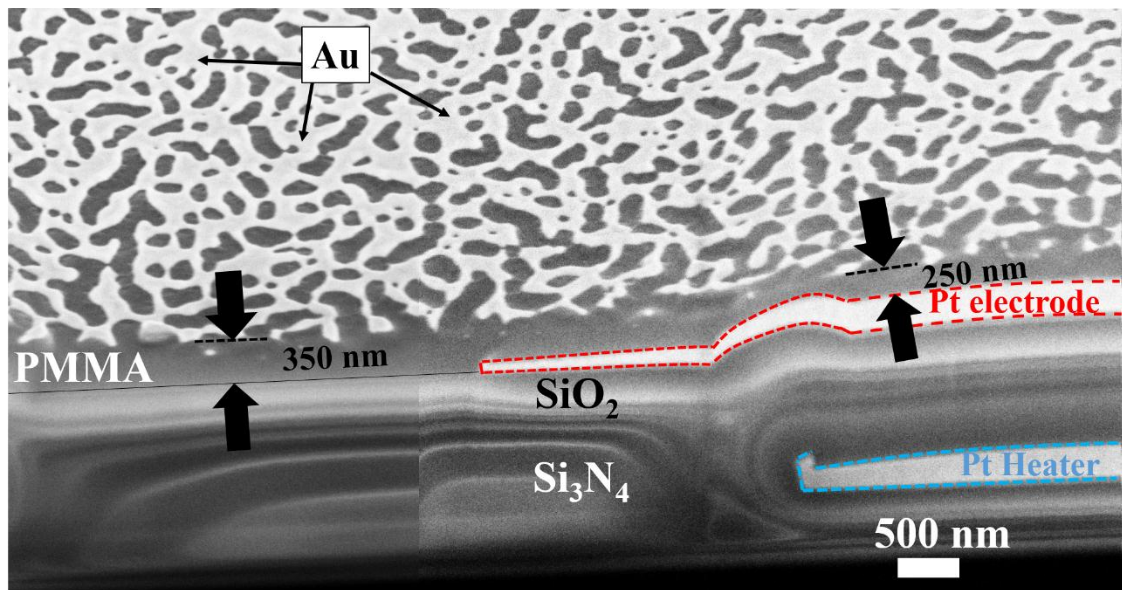

Figure 6.4 Cross section SEM image of the central area of a suspended microhotplate with spin-coated PMMA on the top. The shown membrane corresponds to the central one out of the three present in the chip. The heater gives rise to a thinner resist on top of it, and the area between the heater lines involves a thicker PMMA layer. The scale and the distances are compensated for the tilt of the sample, which is of 52°.

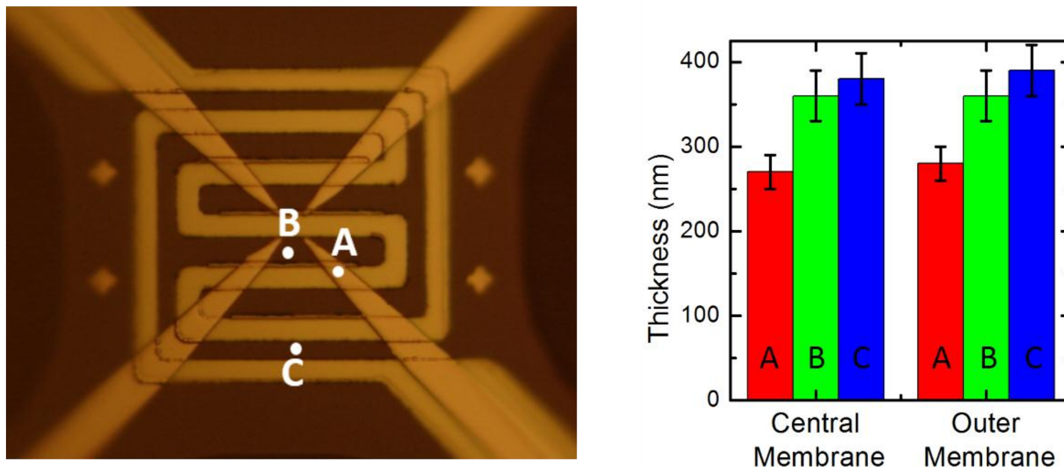

Figure 6.5 Left: Optical micrograph of one of the microhotplates showing the three regions from where cross-sections have been fabricated by FIB and that allow to measure the thickness of the PMMA. The resist was spin-coated at 4500 rpm for 1 minute on top of microhotplates. The thickness has been measured from a cross-section on three different points: A: on top of the electrode and the heater, on B: central part with no underlying heater or electrode, and C: outer part of the membrane, also with no underlying heater or electrode. The analysis has been made on the central membrane and the outer membranes of the chip.

The change in the thickness of the PMMA layer is caused, thus, mainly by the heater, although the electrodes add also a smaller roughness. This effect is taken into account for the fabrication of the contacts, since a contact that follows the heater meander is more convenient in order to avoid a thick area of PMMA, which might not be completely electron exposed.

The profile of PMMA has been studied in three different zones of the microhotplate by performing other similar cross-sections. The outer and the central microhotplates from the chip have been studied and the measured PMMA thickness is represented in Figure 6.5.

The thickness of the PMMA layer has been found, from these measurements, to very slightly increase about 10 nm, in the outer zone of the membranes (C) compared to the central part (B), but this falls almost within the uncertainty of the measurement. On the other hand, no appreciable difference in thickness is found between the outer and the central membranes, proving that they are nominally equal. The main PMMA thickness different contribution is, however, the topography induced by the heater, which supposes a height difference of almost 100 nm. Thus, the height differences of about 200 nm at the microhotplate’s surface before the deposition are reduced to almost 100 nm after the PMMA spin coating at 4500 rpm. Consequently, the experimental

methodology should be able to successfully expose a PMMA layer with a changing thickness throughout the same microhotplate.

6.2.2 Optimization of the fabrication parameters

The final fabrication conditions and parameters, such as electron exposure, spin-coating, and metallization thickness, that have been definitely chosen for the fabrication of the contacts to individual nanowires will be explained and justified in this section, based on the different observations obtained during the first fabrication procedures.

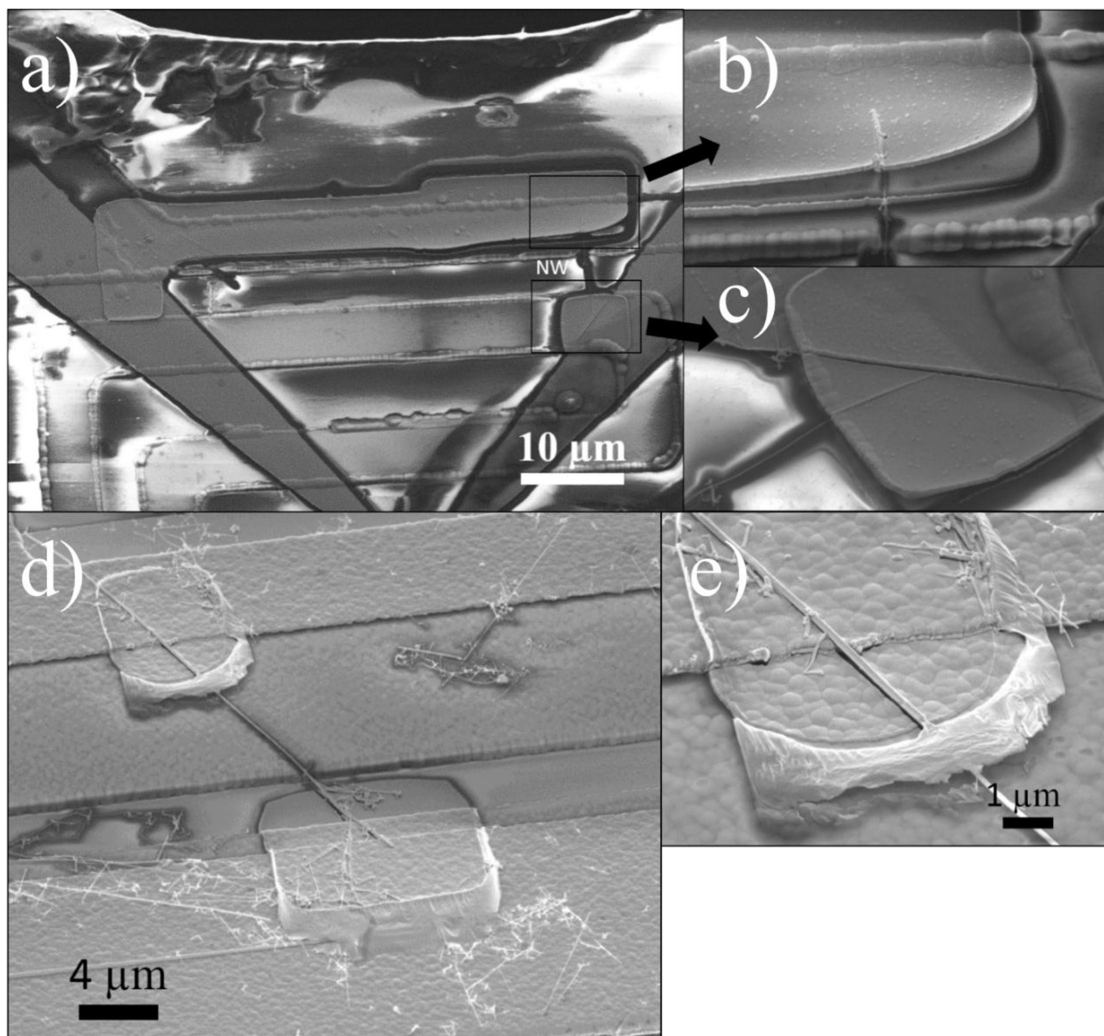

Figure 6.6 SEM images of the Ti/Pt contacts fabricated by EBL: a) on a suspended microhotplate. A bad adherence due to the remaining resist, which is caused by an incomplete exposure, is shown in b) and c); d) Remaining resist after the lift-off on top of micromembranes; e) Detail of the contact on top of the NW and the electrode.

The first determinant of the approach is given by the diameter of the NWs, ranging between 50 – 80 nm. Therefore, the metal deposition has been chosen to have a thickness between 100-120 nm. Consequently, the resist coating should have a thickness of, at least, 400 nm to ensure a successful lift-off process. The PMMA resist coating that better fits the mentioned requirements is PMMA 950k A7 (7% dissolved in anisole and supplied by MicroChem; the PMMA dissolved in chlorobenzene is not used since anisole is much less toxic). Nominally, the spin-coating of this resist provides a range of 400 to 800 nm nominally on a wafer, when spin-coated at 4000 to 1500 rpm, respectively.

Thus, taking into account that the acceleration voltage of the electrons will be 20 kV and using the mentioned PMMA resist, different spin-coating speeds in the range of 3000-4500 rpm were studied. The devices fabricated when PMMA spin-coated below 3000 rpm showed a too high remaining thickness that caused an incomplete exposure and most part of the fabricated contacts were removed during the lift-off step. The most appropriate conditions for the PMMA deposition, in terms of a successful exposure and lift-off, have been found to be 4000 rpm for 1 minute.

Under the mentioned conditions, and using an electron dose between 200 and 400 $\mu C/cm^2$, a bad adhesion of the metal layers has been observed. The SEM images included in Figure 6.6 show the metallization stripes that are, clearly, not well adhered, on top of one microhotplate (on a), b) and c)) and one micromembrane (on d) and e)). The local examination of the still visible metal contacts by Energy Dispersive X-Ray Spectroscopy (EDX) showed the presence of Ti and Pt layers, which, a priori, confirm a good adhesion of the metals at the oxide surface. Note that the contacts in Figure 6.6 a), b), c) and e) are located at the areas on top of the heater, which correspond to the thinner PMMA. The remaining PMMA visible in the areas where metal should have remained appears due to an incomplete exposure of the resist, a consequence of the low electron dose employed.

As a consequence of the previously indicated, the electron dose was increased to 600 $\mu C/cm^2$ in order to ensure a complete exposure. On the other hand, the selected dose is sufficiently low to avoid PMMA to be converted into a negative resist, which takes place at doses around 3000 $\mu C/cm^2$.

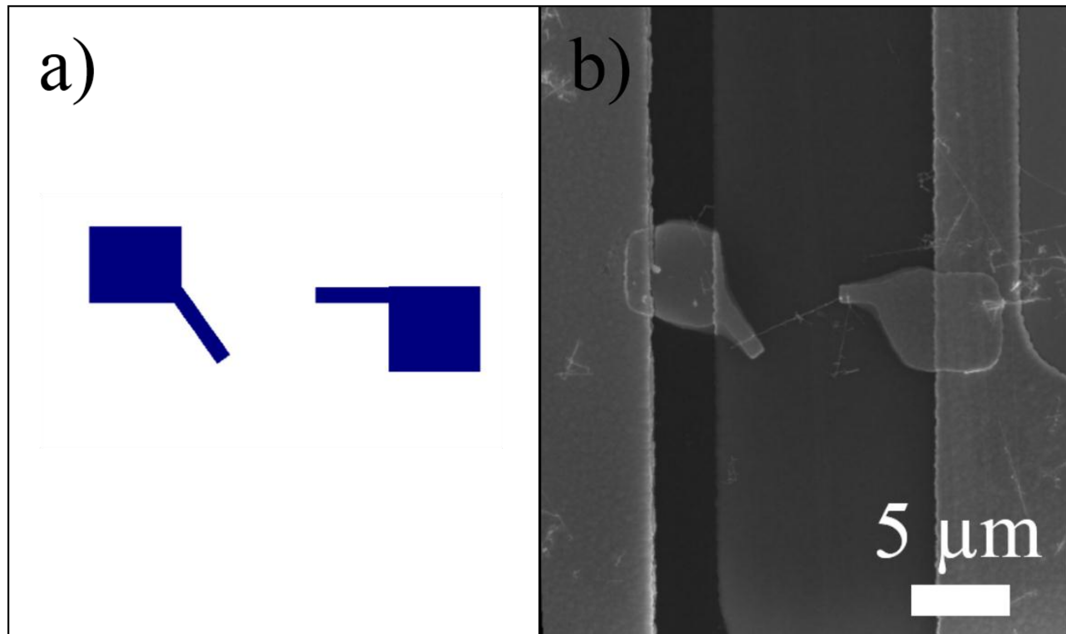

Figure 6.7. a) Scheme of the designed patterns for contacting the NW; b) SEM image of the final Ti/Pt contacts, taken after the lift-off process. Clearly, the proximity effect leads to a widening of the contacts.

During the fabrication of the contacts to the individual nanowires, a widening of the final shape of the patterns, as compared to the designed ones, has been observed, which is attributed to the proximity effect. This is exemplified in Figure 6.7 a), where the pattern designed for contacting a nanowire on a micromembrane is represented. Subsequently, the metal deposition and the lift-off process resulted in the structure shown Figure 6.7 b), where the widening from both patterns is visible.

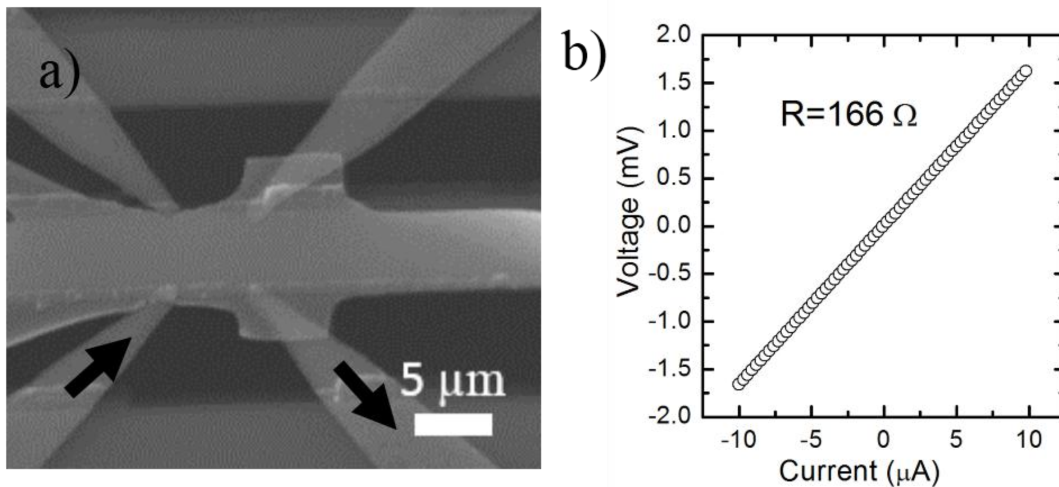

Figure 6.8 a) SEM image of a Ti/Pt deposition whose resistance has been characterized. b) I-V curve of the Ti/Pt metallization indicated by the arrows on a).

This effect is non-desirable, and, in order to minimize it, the thickness of the resist should be reduced, or the acceleration voltage should be diminished [17], which also requires thinner resists for a complete exposure. Since the thickness cannot be reduced, as mentioned previously, the proximity effect cannot be avoided.

A positive aspect, however, is that the nanowires are longer than 10 µm; hence, the fabricated contacts will be separated by several microns, and thus, the overlap of both contacts due to the proximity effect is easily avoided. Furthermore, the size of the patterns is not a critical issue in our approach, considering that the main requirement is to fabricate a metal contact that connects the NW and the electrode.

Titanium and platinum have been used as metal layers for the fabrication of the contacts, since titanium provides a good adhesion to insulating materials, and platinum is not oxidized easily. The resistance of the Ti (20 nm)/Pt (80 nm) contacts has been characterized, obtaining a value between 150 and 300 Ω (see Figure 6.8), depending on the length and wideness of the contact, being negligible in comparison to the resistance of the nanowires, usually between hundreds of kΩ and hundreds of MΩ.

The experimental tests performed to check the resistance of the metal depositions, together with the explained effects, allowed us to find the optimal conditions for the experimental procedure, which are given in detail in Table 6.1. The mentioned conditions have been successfully employed, besides, on both micromembranes and microhotplates.

Table 6.1 Summary of the optimal parameters for the fabrication of contacts for NWs by EBL

Acceleration voltage (kV)	20
Aperture (µm)	20
Spin-Coating	4000 rpm for 1 minute
Soft-bake	180ºC, 60 s on a hotplate
Exposure dose (µC/cm2)	600
Magnification	1000 x
Writing field size (µm2)	100x100
Development	30s MIBK in IPA (ratio 1:2) + 30 s IPA
Metal layers	Ti (20 nm) / 80 nm (Pt)

An estimation of the time for contacting the NWs in one chip using the EBL process is about 2 hours, while for the five chips this may take approximately 6 h, allowing the fabrication of the contacts of about 15 NWs using this procedure, because one chip contains three MHP with their alignment marks. The metal deposition and lift-off process takes about 2 hours in total, thanks to the fact that these processes are done in parallel for all the chips. Comparing to the FIB methodology, which requires 1-2 h for contacting one single NW, the new approach reduces the fabrication time significantly. Furthermore, the low and repetitive resistance of the fabricated contacts is an advantage of the developed methodology when compared to the “platinum” deposits in the FIB, which give rise to a graphitic deposit with platinum inclusions.

6.3 Results and discussion

SEM pictures of three different SnO_2 NWs with EBL-fabricated contacts are shown in Figure 6.9. A single NW, contacted on top of a microhotplate and with a diameter of 50 ± 3 nm, is shown in Figure 6.9 a). The NWs on Figure 6.9 c) and e) have been contacted on top of micromembranes and have a diameter of 55±4 and 70±5 nm, respectively. The figures 6.9 b), d), f) and g) show the details of the fabricated structures with the sample tilted and at higher magnification to assure the coverage of the NW and also to quantify the roughness and the steps of the fabricated contacts created by the heater and by the surface electrodes. The parameters and conditions employed for the fabrication are the detailed in Table 6.1.

6.3.1 Electrical characterization

The contacted nanostructures have been electrically characterized at different temperatures in order to determine the type of contact formed between the deposited metals and the NW. I-V curves obtained at different temperatures for one specific nanowire are shown in Figure 6.10 a).

In general, the junction between a metal and a semiconductor can introduce an energy barrier for the charge carriers crossing the junction, the so-called Schottky barrier that gives rise to an exponential *I-V* behaviour. The contact barrier height, ϕ_b, at

a metal/n-type semiconductor junction is defined as the difference between the bottom of the conduction band of the semiconductor and the Fermi level of the metal:

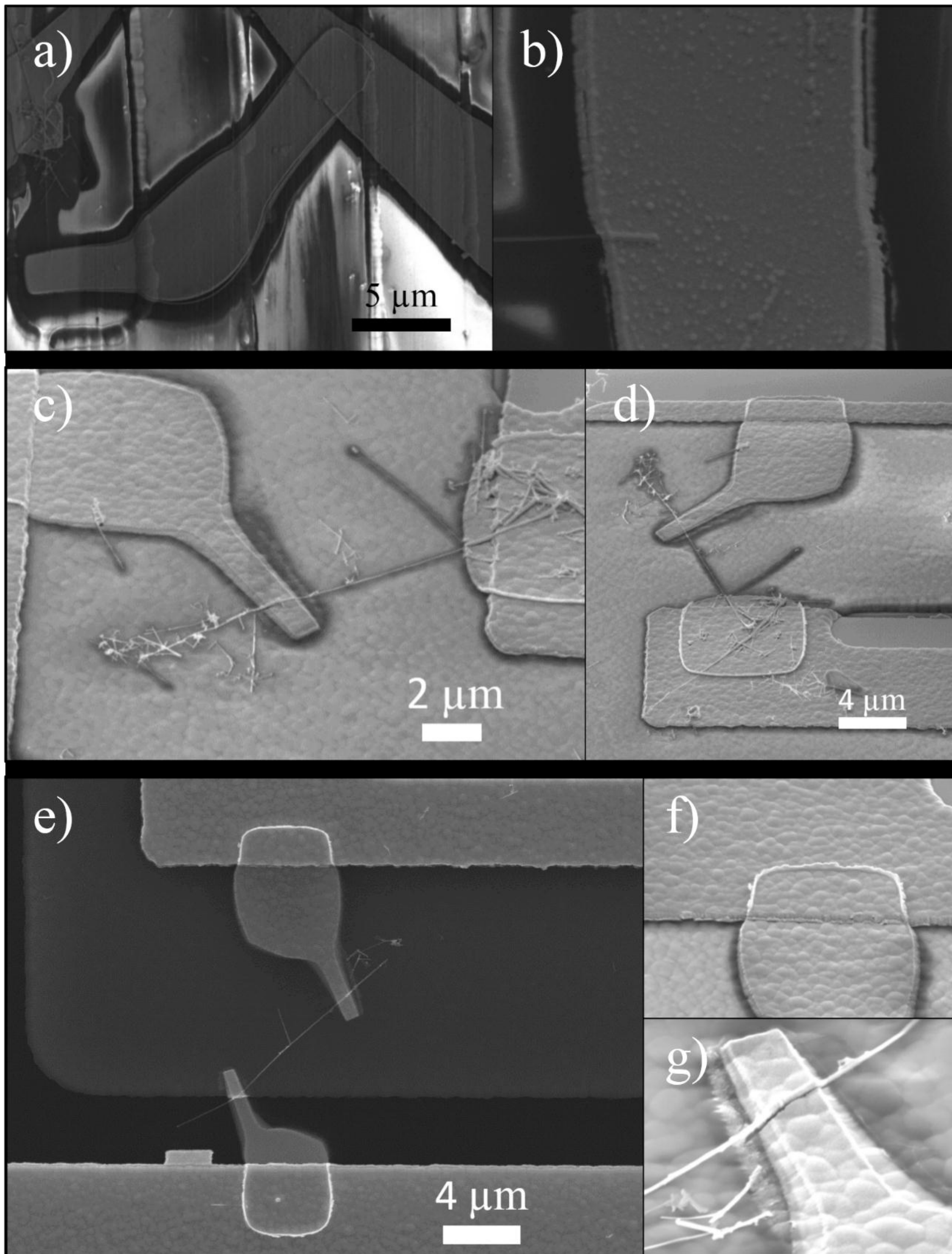

Figure 6.9. SEM pictures of SnO_2 NWs contacted by EBL procedure, on top of a) and b) one microhotplate; c), d), e) f) and g) on top of micromembranes.

$$\phi_b = \phi_m - \chi_s \tag{6.1}$$

Where ϕ_m is the work function of the metal and χ_s is the electron affinity of the semiconductor. Since Ti has a low work function (3.84 eV), and the electron affinity is around 4.9 eV in SnO_2 [18], there should result no barrier and the junction is expected to be Ohmic [19].

However, the I-V curves measured are not ohmic, since at low voltages the I-V curve cannot be fitted to a linear behaviour, but neither to an exponential one. Additionally, the curves are asymmetric, being the device more conductive at negative voltages. Furthermore, the current increases with temperature, as it is represented in Figure 6.10 b), with a subsequent reduction of resistance with temperature, as expected for a semiconductor. It is important to notice that the measured resistance values are relatively high, in comparison to other electrical measurements of single tin dioxide nanowire contacted by FIB [4,20].

The non-Ohmic behaviour can be attributed to the poor electrical contacts, probably due to a the oxidation of the metal, which has been observed by Ti and Cr layers, the most common materials used as adhesion layer [21]. Besides, chemical impurity residues at the semiconductor/metal interface can give rise to the non-ohmic behaviour, which could be originated from organic solvents. This effect is consistent with the high resistance observed for the nanowires.

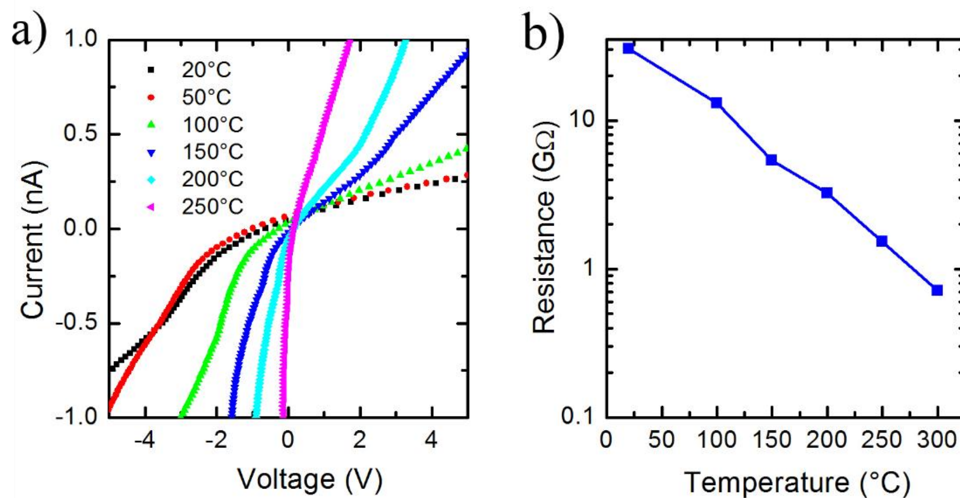

Figure 6.10. a) *I-V* curves at different temperatures from a SnO_2 NW contacted on top of a microhotplate; b) Resistance as a function of temperature, taken as *R*=*V*/*I* with *I*=1 nA.

In order to improve the quality of the contacts and achieve a low resistance Ohmic contacts, an oxygen plasma cleaning process is proposed to be carried out after the development of the resist and before the deposition of the metals, as reported in [21].

6.3.2 Response towards NH_3

Individual SnO_2 NWs have been studied towards different concentrations of ammonia in synthetic air. The same gas sequence alternating ammonia and synthetic air has been used at different temperatures, as it is represented in Figure 6.11 a). The adsorption of ammonia reduces the resistance of the single NW proportionally to the concentration, as can be observed in the same figure. The response of the sensor is defined as follows:

$$Response(\%) = \frac{R_{air} - R_{NH_3}}{R_{air}} \quad (6.2)$$

The steady state response shown by the nanowire as a function of ammonia concentration is represented in Figure 6.11 b). The maximum response shown by the NW reached a value of 75% for 20 ppm of NH_3 at 200 °C. The response at 400 °C is not included in the figure due to the abnormal behaviour observed during the ammonia exposure, which almost cancels the response of the response at this temperature.

Since the study on the ammonia sensing of the SnO_2 NWs network detailed in Chapter 4 has been performed in similar ranges of temperatures and concentrations, the results obtained here will be compared with those of chapter 4.

The maximum response of the locally grown tin dioxide nanowires is 36%, at 400 °C for 40 ppm of ammonia in dry air, which is considerably lower response than for the the single nanowire contacted by EBL. Both sensors demonstrate different kinetic behaviour on the ammonia oxidation, since the response is maximum at different temperatures.

Note, that the nanowire's resistance at 400 °C is diminishes initially when ammonia enters in the measuring chamber, followed by a slow rise of the resistance. This tendency has been also observed in the network of nanowires at 400 and 450°C. This effect is more pronounced in single NW, resulting in an almost negligible response at this temperature, and as explained in Chapter 4, is caused by the oxidation of ammonia to nitric oxide according to the following reaction:

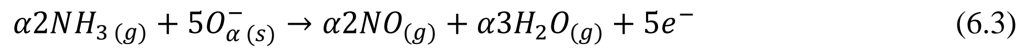

$$\alpha 2NH_{3\,(g)} + 5O^{-}_{\alpha\,(s)} \rightarrow \alpha 2NO_{(g)} + \alpha 3H_2O_{(g)} + 5e^{-} \qquad (6.3)$$

Nitric oxide is oxidized to NO_2 and, then, chemisorbed at the surface, causing the increase in resistance as described by the following two subsidiary reactions:

$$2NO_{\,(g)} + O_2 \rightarrow 2NO_{2(g)} \qquad (6.4)$$

$$NO_{2\,(g)} + e^{-} \rightarrow NO^{-}_{2(s)} \qquad (6.5)$$

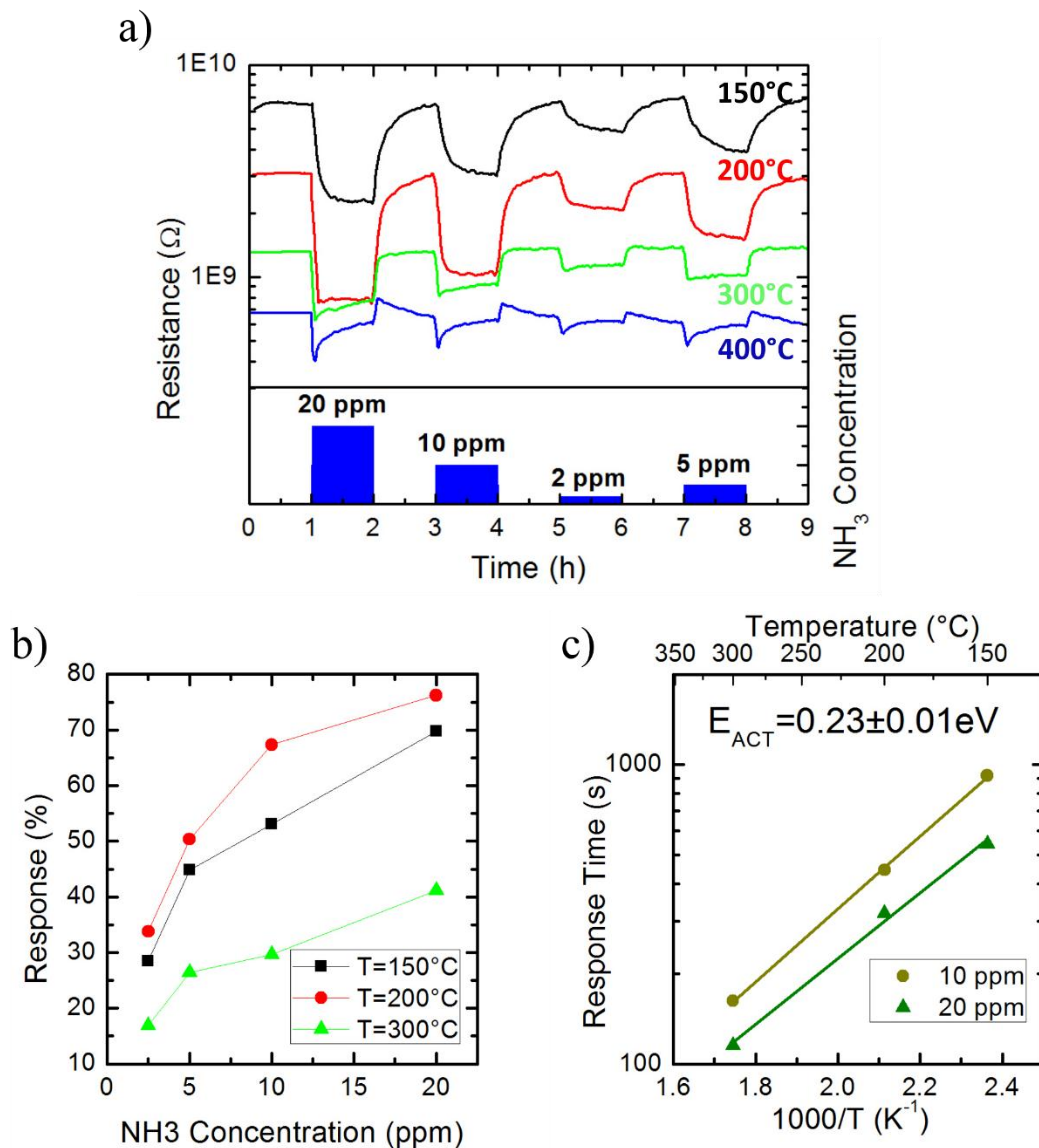

Figure 6.11 a) Resistance change of individual NW towards different ammonia exposure of 1 hour, at four different temperatures; b) Measured response represented as a function of ammonia concentration. The response obtained at 400°C is not shown due to an abnormal behaviour that almost cancels it; c) Arrhenius plot of the response time, represented for pulses of 10 and 20 ppm of NH_3. Symbols are the experimentally obtained values and lines are the exponential fittings.

However, another effect is observed on individual nanowire that has not been observed in the SnO_2 nanowires network. The sensor resistance increases when ammonia is removed from the chamber, followed by a slow reduction, as can be observed from Figure 6.11 a). Both abnormal effects were observed in ammonia sensing using nanocrystalline WO_3 powders at temperatures above 300°C [22,23]. The second effect is attributed to the remaining chemisorbed NO_2 molecules, which are desorbed more slowly than ammonia molecules at those temperatures. Therefore, after the ammonia removal, NO_2 molecules are still adsorbed at the surface; the subsequent desorption of nitrogen dioxide leads to the decrease in resistance. Consequently, for practical applications, that temperature regime should be avoided in order to operate a reliable ammonia sensor.

Regarding the kinetic properties, the individual nanowire sensor shows a response time towards 20 ppm of ammonia of less than 2 minutes at 300 ºC, a smaller value than the one measured for the network of NWs at the same temperature (about 5 minutes). A possible explanation is that the latter contains multiple nanowires, distributed in a network to which the gas adsorbate must diffuse and be adsorbed. The diffusion thus, takes place more slowly than in the single nanowire-based sensor, resulting in a longer response time.

An Arrhenius plot of the response time as a function of the inverse of the temperature is represented in Figure 6.11 c), which can be fitted to an exponential dependence according to:

$$\tau = \tau_0 \exp\left(\frac{E_{act}}{k_B T}\right) \quad (6.6)$$

The activation energy obtained from the fitting is E_{act}=0.23±0.01 eV, for which the data between 150 and 300 °C have been employed. A linear behaviour in the Arrhenius plot implies that the same sensing mechanism takes place over the whole temperature range, which, as it was discussed in Chapter 4, can be described by two concurring reactions:

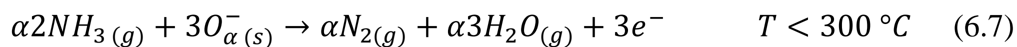

$$\alpha 2NH_{3\,(g)} + 3O^-_{\alpha\,(s)} \rightarrow \alpha N_{2(g)} + \alpha 3H_2O_{(g)} + 3e^- \qquad T < 300\ °C \quad (6.7)$$

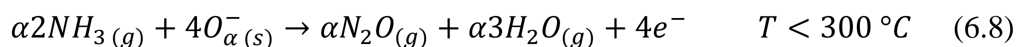

$$\alpha 2NH_{3\,(g)} + 4O^-_{\alpha\,(s)} \rightarrow \alpha N_2O_{(g)} + \alpha 3H_2O_{(g)} + 4e^- \qquad T < 300\ °C \quad (6.8)$$

From the experimental data, we can only ensure that this mechanism takes place up to 300 °C. At 400 °C, because of the unstable response time, one cannot assure whether we are still in the same regime, although the abnormal behaviour at that temperature suggests that the promoted mechanism is described by equation (6.3). The measured activation energy, however, is lower than in the case of network of SnO_2 (0.35 eV) and the reported value (0.74 eV) in [24].

The results presented are consistent with a similar work, where the response of a single tin dioxide nanowire was analysed towards ammonia [25]. The response was found to be maximum at temperatures between 210 and 250 °C, similarly to the results presented in this work. The activation energy in that study (0.5 eV) was higher than the one obtained here.

6.3.3 Response towards NO_2

The sensing behaviour of individual nanowire towards nitrogen dioxide diulet in air has also been studied. The exposure towards NO_2 strongly increases the resistance of the single NW, as represented in Figure 6.12 a). Different temperatures have been used during the sensing experiments towards nitrogen dioxide. The response is obtained according to the following:

$$Response(\%) = \frac{R_{NO_2} - R_{air}}{R_{air}} \quad (6.9)$$

The measured response as a function of the NO_2 concentration is shown in Figure 6.12 b). The relative change towards 250 ppb of NO_2 is notably high, reaching a value of 300%. On the other hand, the response is maximized at 300°C for all the concentrations, as represented in Figure 6.12 b). This temperature is in agreement with [26], which observed the same temperature at which the response is promoted. On the other hand, in other sensors employing single SnO_2 NW contacted by FIB, a temperature of 200 °C was observed [27].

The shortest response time is reached during the pulses with the maximum NO_2 concentration, 2000 ppb, acquiring a value of 3 minutes at 400°C. Response time of approximately 7 minutes are obtained at a temperature of 300 °C.

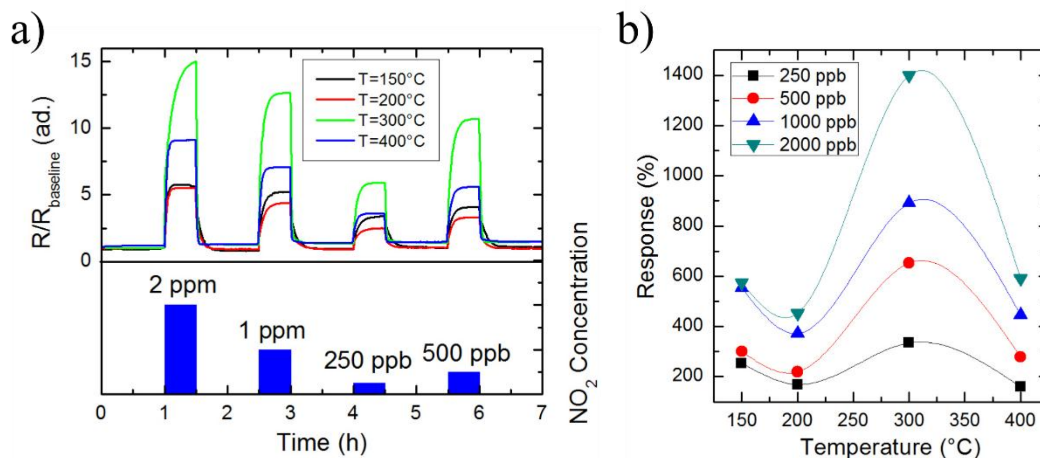

Figure 6.12 Resistance evolution of individual tin dioxide nanowire, contacted by EBL, towards different NO_2 exposures in synthetic air at 4 different temperatures; b) Response of individual as a function of the temperature, for the different concentrations of NO_2.

Comparing to the mesh of SnO_2 NWs, summarized in Chapter 4, the response of the network reaches the 30% as maximum towards 5 ppm, i.e., shows a response two orders of magnitude below than the single NW. Furthermore, the response time is longer in the case of the mesh of NWs. Therefore, the response against NO_2 is consistent with the results obtained in the study towards ammonia, demonstrating a higher response and shorter response time for the individual NW-based sensor. As mentioned previously, the easier diffusion provides a shorter response time.

6.4 Conclusions

Individual SnO_2 nanowires have been contacted by Electron Beam Lithography on top of microhotplates and micromembranes. A changing thickness of the resist has been observed, due to the roughness of the surface of the micromembrane. Thus, an optimum set of experimental parameters has been obtained from the preliminary studies: spin-coating conditions of the PMMA resist (4000 rpm), of the exposure dose (600 $\mu C/cm^3$) and the metal thickness (100 nm), which are valid for contacting NWs with diameters up to 80 nm.

The fabricated nanodevices have been studied as gas sensors at different temperatures and towards both oxidizing and reducing gases, showing a stable response towards ammonia and nitrogen dioxide in air. The sensing mechanism towards NH_3 is consistent with the results obtained with multiple tin dioxide nanowires. The ammonia

oxidation towards nitric oxide specie is promoted at 400 °C, a temperature slightly lower than the exhibited by network of NWs. Single NW devices have shown faster response than their mesh counterpart, in ammonia and nitrogen dioxide studies, attributed to the easier diffusion of the gas.

6.5 References

[1] S. Barth, F. Hernandez-Ramirez, J.D. Holmes, A. Romano-Rodriguez, Synthesis and applications of one-dimensional semiconductors, Prog. Mater. Sci. 55 (2010) 563–627. doi:10.1016/j.pmatsci.2010.02.001.

[2] J.D. Prades, R. Jimenez-Diaz, F. Hernandez-Ramirez, S. Barth, A. Cirera, A. Romano-Rodriguez, et al., Ultralow power consumption gas sensors based on self-heated individual nanowires, Appl. Phys. Lett. 93 (2008) 123110. doi:10.1063/1.2988265.

[3] J.D. Prades, R. Jimenez-Diaz, F. Hernandez-Ramirez, S. Barth, A. Cirera, A. Romano-Rodriguez, et al., Ultralow power consumption gas sensors based on self-heated individual nanowires, Appl. Phys. Lett. 93 (2008). doi:10.1063/1.2988265.

[4] F. Hernández-Ramírez, A. Tarancón, O. Casals, J. Rodríguez, A. Romano-Rodríguez, J.R. Morante, et al., Fabrication and electrical characterization of circuits based on individual tin oxide nanowires., Nanotechnology. 17 (2006) 5577–5583. doi:10.1088/0957-4484/17/22/009.

[5] Y. Chen, Nanofabrication by electron beam lithography and its applications: A review, Microelectron. Eng. 135 (2015) 57–72. doi:http://dx.doi.org/10.1016/j.mee.2015.02.042.

[6] P. Durina, A. Bencurova, A. Konecnikova, I. Kostic, K. Vutova, E. Koleva, et al., Patterning of structures by e-beam lithography and ion etching for gas sensor applications, J. Phys. Conf. Ser. 514 (2014) 12037. http://stacks.iop.org/1742-6596/514/i=1/a=012037.

[7] P. Candeloro, A. Carpentiero, S. Cabrini, E. Di Fabrizio, E. Comini, C. Baratto, et al., SnO2 sub-micron wires for gas sensors, Microelectron. Eng. 78–79 (2005) 178–184. doi:http://dx.doi.org/10.1016/j.mee.2004.12.024.

[8] K.J. Jeon, J.M. Lee, E. Lee, W. Lee, Individual Pd nanowire hydrogen sensors fabricated by electron-beam lithography, Nanotechnology. 20 (2009) 135502. http://stacks.iop.org/0957-4484/20/i=13/a=135502.

[9] † Michael S. Arnold, † Phaedon Avouris *, ‡ Zheng Wei Pan, and Zhong L. Wang‡, Field-Effect Transistors Based on Single Semiconducting Oxide Nanobelts, J. Phys. Chem. B. 107 (2003) 659–663. doi:10.1021/jp0271054.

[10] D. Kälblein, R.T. Weitz, H.J. Böttcher, F. Ante, U. Zschieschang, K. Kern, et al., Top-Gate ZnO Nanowire Transistors and Integrated Circuits with Ultrathin Self-Assembled Monolayer Gate Dielectric, Nano Lett. 11 (2011) 5309–5315. doi:10.1021/nl202767h.

[11] § Xiaocheng Jiang †, § Qihua Xiong †, ‡ Sungwoo Nam, † Fang Qian, † Yat Li, ‡ and Charles M. Lieber* †, InAs/InP Radial Nanowire Heterostructures as High Electron Mobility Devices, Nano Lett. 7 (2007) 3214–3218. doi:10.1021/nl072024a.

[12] S.N. Das, J.P. Kar, J.-H. Choi, T. Il Lee, K.-J. Moon, J.-M. Myoung, Fabrication and Characterization of ZnO Single Nanowire-Based Hydrogen Sensor, J. Phys. Chem. C. 114 (2010) 1689–1693. doi:10.1021/jp910515b.

[13] A. Köck, L. Chitu, S. Defregger, E. Kraker, G. Maier, S. Steinhauer, et al., Metal Oxide Nanowires for Gas Sensor Applications, BHM Berg- Und H{ü}ttenm{ä}nnische Monatshefte. 159 (2014) 385–389. doi:10.1007/s00501-014-0286-5.

[14] L. Liao, Z. Zheng, B. Yan, J.X. Zhang, H. Gong, J.C. Li, et al., Morphology Controllable Synthesis of α-Fe2O3 1D Nanostructures: Growth Mechanism and Nanodevice Based on Single Nanowire, J. Phys. Chem. C. 112 (2008) 10784–10788. doi:10.1021/jp802968a.

[15] P. T. Moseley, Solid state gas sensors, 223 (1997).

[16] S. Mathur, S. Barth, H. Shen, J.-C. Pyun, U. Werner, Size-Dependent Photoconductance in SnO2 Nanowires, Small. 1 (2005) 713–717. doi:10.1002/smll.200400168.

[17] M.A. Mohammad, M. Muhammad, S.K. Dew, M. Stpanova, Nanofabrication, Techniques and principles. Chapter 2: Fundamentals of Electron Beam Exposure and Development, Springer-Verlag/Wien, 2012. doi:10.1007/978-3-7091-0424-8.

[18] H. Elhouichet, A. Moadhen, M. Oueslati, S. Romdhane, J.A. Roger, H. Bouchriha, Structural, optical and electrical properties of porous silicon impregnated with SnO2:Sb, Phys. Status Solidi. 2 (2005) 3349–3353. doi:10.1002/pssc.200461165.

[19] S.M. Sze, Physics of Semiconductor Devices, 3rd Editio, John Wiley & Sons, 2006.

[20] F. Hernandez-Ramirez, a. Tarancon, O. Casals, E. Pellicer, J. Rodriguez, a. Romano-Rodriguez, et al., Electrical properties of individual tin oxide nanowires contacted to platinum electrodes, Phys. Rev. B. 76 (2007) 85429. doi:10.1103/PhysRevB.76.085429.

[21] Y. Cheng, R. Yang, J.P. Zheng, Z.L. Wang, P. Xiong, Characterizing individual SnO 2 nanobelt field-effect transistors and their intrinsic responses to hydrogen and ambient gases, Mater. Chem. Phys. 137 (2012) 372–380. doi:10.1016/j.matchemphys.2012.09.037.

[22] I. Jiménez, M.A. Centeno, R. Scotti, F. Morazzoni, J. Arbiol, A. Cornet, et al., NH3 interaction with chromium-doped WO3 nanocrystalline powders for gas sensing applications, J. Mater. Chem. 14 (2004) 2412. doi:10.1039/b400872c.

[23] I. Jiménez, M. a. Centeno, R. Scotti, F. Morazzoni, A. Cornet, J.R. Morante, NH3 Interaction with Catalytically Modified Nano-WO3 Powders for Gas Sensing Applications, J. Electrochem. Soc. 150 (2003) H72. doi:10.1149/1.1556055.

[24] N.I. Il'chenko, Catalytic Oxidation of Ammonia, Russ. Chem. Rev. 45 (1976) 1119–1134. doi:10.1070/RC1976v045n12ABEH002765.

[25] F. Shao, M.W.G. Hoffmann, J.D. Prades, J.R. Morante, N. López, F. Hernández-Ramírez, Interaction mechanisms of ammonia and Tin oxide: A combined analysis using single nanowire devices and DFT calculations, J. Phys. Chem. C. 117 (2013) 3520–3526. doi:10.1021/jp3085342.

[26] M. Tonezzer, N. V. Hieu, Size-dependent response of single-nanowire gas sensors, Sensors Actuators, B Chem. 163 (2012) 146–152. doi:10.1016/j.snb.2012.01.022.

[27] J.D. Prades, R. Jimenez-Diaz, F. Hernandez-Ramirez, S. Barth, A. Cirera, A. Romano-Rodriguez, et al., Ultralow power consumption gas sensors based on self-heated individual nanowires, Appl. Phys. Lett. 93 (2008). doi:http://dx.doi.org/10.1063/1.2988265.

7. CONCLUSIONS AND FUTURE PERSPECTIVES

7.1. General Conclusions

Different objectives were proposed at the starting of this thesis. Part of them were related to the process fabrication and integration of NWs, and others were focused on the study and analysis of the sensing mechanisms, and thus, on the optimization of the fabricated devices.

All the sensors have been fabricated on top of microhotplates or micromembranes, which allows to heat them to the appropriate operative temperature range for gas sensing, requiring supply power between few mW and up to tens of mW, depending on the employed substrate. Thus, low power devices have been successfully fabricated, fulfilling one of the main actual requirements for gas sensors.

7.1.1. On the fabrication process

Two different configurations of active layers of gas sensors based on nanowires have been fabricated: meshes of NWs and individual NW.

1. CMOS compatible growth of meshes of NWs has been carried out on top of microhotplates and micromembranes. The growth is a simple, scalable and cost effective strategy, which gives rise to a localized and site-specific growth of NWs on the sensing part of the electronic platform, i.e., confined in the heated area. Ge and SnO_2 nanowires have been grown using this methodology. The locally grown nanostructures have shown to be single-crystalline, being equivalent to the nanowires grown by a standard CVD method.

   The growth is a mask-less process, and involves a severe reduction of the power consumption (few to tens of mW) and of the growth time compared to a standard CVD process. The innovative approach is a first step towards the fabrication of single crystalline nanowire-based gas sensors devices.

2. Gas sensors based on individual SnO_2 nanowires have been developed, by fabricating metal contacts to them through an Electron Beam Lithography procedure on top of microhotplates and micromembranes.

   The microhotplates and micromembranes, presenting an important roughness at the surface, have been characterized in order to solve the specific problems

derived from this fact, that would conduct to an incomplete resist exposure due to the changing thickness of the resist.

The fabrication procedure has been demonstrated as a successful approach for contacting individual NWs with a diameter below 80 nm. Metal contacts with low resistance have been fabricated, a clear advantage compared to the contacts fabricated by FIB, which is the reference technology of the research group. Additionally, the here presented approach represents an important reduction of the fabrication time compared to FIB methodology.

7.1.2. On the sensing performance

The fabricated devices based on NWs have been characterized as gas sensors, and the sensing mechanisms have been analysed. The following conclusions have been obtained from the gas sensing measurements:

Network of SnO_2 NWs

1. The sensing mechanisms towards ammonia, when diluted in dry and humid air, have been elucidated. The analysis of the sensor kinetic response has been performed in the range between 150 and 450 ºC, with the maximum response being obtained at 300 ºC.

   In dry conditions, the promotion of NO byproduct reduces the response of the sensor at temperatures above or equal to 450 ºC. When operating in humid conditions, the response towards ammonia diminishes due to the behaviour of water vapour and ammonia competing for the same adsorption sites. The activation energy of ammonia oxidation is lowered in humid conditions, which is attributed to the reaction of O_2 and OH adsorbed groups, facilitating the oxygen dissociation.

2. The response towards NO_2, CO and oxygen has been studied. The response towards this gases, has been demonstrated to be lower than ammonia, and when operating at 400 °C, the maximum response is enhanced against ammonia in dry conditions.

Single SnO_2 nanowire

1. The fabricated devices have been characterized towards ammonia, showing the same sensing mechanisms as the meshes of tin dioxide NWs, but at lower temperatures. In these sensors, the NO byproduct is promoted at 400ºC, and the optimum response is obtained at 300ºC.
2. The single NW-based sensors have shown faster response than their mesh counterpart towards NO_2 and NH_3. This is attributed to the easier diffusion of the gas in these devices due to the fact that all the surface is exposed to the gas.
3. The sensors show are more ohmic behaviour at lower temperature that their FIB-fabricated counterparts and their resistance lies in an interesting range for combining the devices with low-cost low-power portable electronic boards.

Network of Ge NWs

1. For the first time, Ge NWs have been studied as gas sensor. The p-type behaviour of the NWs has been experimentally observed.
2. The GeO_x shell around the Ge core plays a key role in the sensing mechanisms, providing the reaction sites for the charge transfer with the gas species, and at the same time, allowing the charge transfer from the semiconductor.
3. The pre-adsorption of oxygen has been demonstrated to be necessary for the sensing of CO, determining the sensing behaviour as a p-type metal oxide sensor.
4. The operating temperature needs to be kept equal or below 100 ºC to ensure a stable Ge oxide shell and, thus, a stable gas sensing device. This stability is supported by the TEM investigation that confirms that the GeO_x shell is stable up to one week at 100 ºC in air.
5. The sensing of water vapour differs form that of metal oxides and takes place by a physisorption process of the water dipoles, but in an unusual configuration, with the hydrogen atoms pointing towards the wire and the oxygen atom moving away from the nanowire. The physisorption is attributed to the low temperature employed on the gas sensing, induced by the presence of phenyl groups at the surface. No competing mechanism nor interaction of water vapour with oxygen has been observed.

7.2. Future work

In the following, some routes are proposed to continue and further extend the innovative and promising processes developed in the thesis.

Extending the site-specific growth of NWs

The localized growth of NWs can be extended to the synthesis of other metal oxide materials. The versatility of the technique allows to grow different materials using the integrated process on the same chip, just by flowing different precursors in different stages, and heating micromembranes or microhotplates at each stage to the optimum growth temperature, calibrated using a standard CVD furnace.

Thus, the fabrication of NW-based meshes of different materials on the same chip allows to fabricate an integrated electronic nose. The different materials will show a specific response towards each gas mixture, which leads to an improvement of the specificity, one of the main challenges of the gas sensors, by creating a nano-e-nose (nano electronic nose).

Localized growth of a single NW

The fabrication of nanosized patterns by EBL on top of micromembranes can be combined with the localized growth procedure to induce the growth of nanowires on specific areas of the hotplate, determined by the predefined pattern. Fabricating small patterns made of Au, as a catalyst for the growth, of few tens of nanometers, the growth of individual nanowires might be carried out.

The application of a local electric field during the growth, using for instance, two electrodes on microhotplates containing four electrodes, may allow the addressing of the growth of a single NW from one contact to the other, and thus, grow locally one individual nanostructure eliminating several complicated steps as the transferring, and post-contacting.

Germanium NWs

More research efforts must be carried out in order to obtain a better understanding of the sensing mechanisms of Ge NWs. The presence of phenyl groups at the surface has been proposed to induce the adsorption of water dipoles; however, no experimental evidence has been obtained. The direct experimental observation through XPS, for

instance, or by FTIR measurements in transmission mode can contribute to provide their deeper comprehension.

Furthermore, the study of n-type Ge NWs as gas sensor may add clarity to the understanding of the sensing mechanisms. As pointed in Chapter 5, the n-type Ge nanowires were reported to be more easily oxidized than p-type NWs; therefore, new studies on maintaining a stable GeO_x layer would be required. On the other hand, the NWs may exhibit different properties, since n-type gas sensors show generally higher response than p-type semiconducting sensors. The comparison of both nanowires, additionally, could provide a better understanding on this concept, since few semiconductors that act as a gas sensor can be doped to provide both conductive behaviours.

EBL procedure

The deposition and alignment of NWs by means of dielectrophoretic forces, by applying an alternating field on a microhotplate, allows the deposition of single or multiple NW between the electrodes. Thus, the final step consisting in the fabrication of the metal contacts, in order to ensure a successful conduction path with the electrodes, can be carried out easily with the EBL procedure, which may be almost automatized.

RESUM EN CATALÀ

Introducció

La qualitat de l'aire és actualment, una preocupació per a les institucions governamentals [1]. La presència de pol·lució i de gasos perjudicials per a la salut és la primera causa mediambiental de mort prematura a la Unió Europea [2]. Així doncs, la detecció en temps real de gasos tòxics, i partícules en suspensió a ambients exteriors i interiors, és necessari per tal d'activar les mesures de seguretat corresponents en cas de superar el llindar màxim d'exposició referent al gas perjudicial.

Els sensors de gas són emprats en diferents àmbits, com per exemple, en la monitorització de la qualitat de l'aire o en aparcaments subterranis, on els sensors encenen els sistemes de ventilació que extreuen CO acumulat a l'interior. Altres aplicacions es poden trobar en els tubs d'escapament dels automòbils, o en fàbriques on es manipulin productes químics, el risc de fuga dels quals suposa una amenaça per a la salut dels treballadors [3].

En aquest sentit, actualment es poden trobar diverses tecnologies emprades per a la fabricació de sensors de gas. Una de les més importants es basa en òxids metàl·lics, materials semiconductors de banda prohibida ampla, d'entre 2 i 4 eV [4]. Aquesta tecnologia ofereix baix cost, comparat amb altres metodologies com els sensors òptics o cromatògrafs. Els avantatges d'aquests sensors radiquen en la simplicitat de la transducció de la quantitat química i la possibilitat d'integració en la tecnologia CMOS [5].

Els sensors resistius basats en òxids metàl·lics es fonamenten en un canvi en la conductivitat, o conseqüentment, de la resistència del sensor degut a la presència d'un gas que és adsorbit a la seva superfície. La interacció entre el gas adsorbit i el semiconductor involucra un intercanvi de càrrega que requereix, generalment, d'una temperatura superior a l'ambient per tal promoure-la [6]. La càrrega provinent del semiconductor indueix un canvi en la conductivitat superficial del material, que podrà ser detectada com a canvi en la resistència del material en la mesura que l'efecte superficial contribueix al volum del material [7]. Per tant, una gran relació superfície-volum del material aportarà una gran sensitivitat al sensor .

Així doncs, degut a la seva alta relació superfície volum, les nanoestructures són, unes candidates òptimes per a ser emprades com a sensors de gas. Entre elles, destaquen els nanofils d'òxids metàl·lics [8], que van ser utilitzats per primera vegada amb aquesta finalitat fa més d'una dècada [9], i des d'aleshores, s'han realitzat importants esforços a nivell de recerca per tal, per una banda, millorar la comprensió dels mecanismes de sensat involucrats, i per l'altra, aprofundir en els processos de síntesi, fet que ha portat al desenvolupament de noves rutes de síntesi, i una millora en el control de la forma, diàmetre i ràtio diàmetre/longitud dels nanofils [10].

Un dels principals desafiaments per a la comercialització de sensors de gas basats en nanofils és la integració d'aquests en dispositius electrònics de forma que sigui un procés repetible i escalable, en el que el temps i els costos de fabricació siguin moderats [11].

Objectius de la tesi

Aquesta tesi s'emmarca en la utilització de nanofils d'òxids metàl·lics per a fabricar sensors de gas de baix consum. El principal objectiu d'aquesta tesi és la millora i

optimització d'aquests sensors, sota un dels punts fonamentals, la integració senzilla dels nanofils en dispositius de baix consum. A més, els sensors han estat caracteritzats per tal d'analitzar els mecanismes físics i químics de sensat, i en conseqüència, aconseguir l'optimització dels mateixos dispositius.

Els principals objectius es poden resumir de forma breu en els següents punts:

1. Creixement localitzat de nanofils sobre microplataformes calefactores. El mètode es basa en la integració de la síntesis dels nanofils realitzada de forma directa a l'àrea definida entre els elèctrodes per mitjà de deposició química de vapor (*Chemical Vapour Deposition),* de forma localitzada, obtenint com a resultat una xarxa de nanofils. Immediatament després del creixement, els nanofils poden ésser mesurats i emprats com a sensor de gas, sense requerir un post-procés.

   Nanofils de SnO_2 i de Ge han estat crescut a través d'aquest procés innovador. Els sensors fabricats a través d'aquesta ruta han estat analitzats envers diferents gasos. Els nanofils de Germani han estat estudiats per primera vegada, segons el nostre coneixement, com a sensor de gas.

2. Utilització de microdispositius de baix consum. La fabricació dels sensors de gas es realitza sobre microplataformes calefactores o micromembranes, corresponents a sistemes microelectromecànics (*MEMS* per les seves sigles en anglès).

3. Nova metodologia per a la fabricació de sensors basats en nanofils individuals sobre microplataformes calefactores. Un nou procediment ha estat desenvolupat basat en la litografia per feix d'electrons (*EBL* per les seves sigles en anglès).

Resultats i discussió

Creixement localitzat de nanofils de SnO_2 i Ge

El mètode localitzat de síntesi dels nanofils es basa en un mecanisme Vapor-Líquid-Sòlid, en una àrea localitzada en micromembranes i microplaques calefactores. Les microplaques calefactores i micromembranes contenen uns microcalefactors que permeten escalfar la superfície de la membrana fins a 450 i 750 °C respectivament. En aquest procediment, una capa prima i discontínua d'or (de gruix entre 1-3 nm,). Aquesta capa, quan és escalfada a la temperatura de descomposició del precursor actua com a catalitzador i com a suport per la nucleació del creixement. Els xips són muntats en suports tipus TO-8 en una cambra de quars, en el que flueix el precursor per a la posterior termòlisis localitzada del mateix, que dóna lloc al creixement de nanofils.

Els nanofils de SnO_2 són sintetitzats a partir del precursor sòlid $Sn(OtBu)_4$, el qual sublima en les condicions de buit emprades. Els nanofils de Ge són sintetitzats a partir del precursor líquid $H_2Ge(C_6H_5)_2$. Les temperatures de creixement són 400-420 °C pels nanofils de Ge, i 700-750 °C per els nanofils de SnO_2. La pressió mantinguda durant el creixement es troba en un buit relativament baix, al voltant de $4 \cdot 10^{-2}$ mbar.

Els nanofils de SnO_2 han estat caracteritzats a través de microscòpia electrònica d'electrons, mostrant una estructura monocristal·lina tetragonal (rutil), amb una direcció de creixement [101]. Els nanofils de Ge són monocristal·lins amb una fase cristal·lina cúbica, i un creixement predominant al llarg de la direcció [111].

Creixement localitzat de nanofils de SnO_2 per sensat d'amoníac en aire humit

Les xarxes de nanofils de SnO_2 han estat emprades per estudiar els mecanismes de sensat de gas envers NH_3 diluït en aire sec i humit, envers concentracions d'entre 10 i 40 ppm d'aquest gas, una valors concentracions entre els que es troba l'exposició màxima recomanada per l'Organització Mundial per la Salut [2].

Els mecanismes de sensat han estat analitzats a diferents temperatures en aire sec i aire humit. La cinètica de la resposta ha estat estudiada, i parametritzada segons l'equació d'Arrhenius, observant així diferents règims en temperatura dels mecanismes. Aquests es troben relacionats amb la oxidació dels elements amb contingut de nitrogen provinents de la anomenada oxidació d'amoníac per part del diòxid d'estany. La presència de vapor d'aigua en el sensat d'amoníac fa disminuir la resposta de l'últim, ja que ambdós competeixen per els mateixos llocs d'absorció. A més, la pressió parcial de vapor d'aigua és 3 ordres de magnitud major que la d'amoníac, motiu pel qual l'adsorció es veu afavorida.

La resposta del sensor és estable i reversible, i mostra uns temps de resposta al voltant de 2 min. A més, el sensor ha estat caracteritzat envers NO_2, CO a diferents temperatures, observant una resposta superior envers NH_3 mantenint una temperatura de 400 °C.

Sensors de baixa temperatura basats en nanofils de Ge

Els nanofils de Ge han estat caracteritzats per primera vegada, com a sensor de gas envers espècies oxidants i reductores en aire sintètic.

Els nanofils de Ge han estat elèctricament estudiats, sota una configuració de transistor d'efecte camp, emprant les mateixes microplaques calefactores sobre les que s'han sintetitzat els nanofils. S'ha observat que els nanofils crescuts són semiconductors tipus p, atribuït a la incorporació del catalitzador de Au a l'estructura del nanofils, els quals creen nivells acceptadors a la banda prohibida del Ge [12].

A través de microscòpia de transmissió d'electrons, ha estat observat una capa amorfa d'òxid de Ge (GeO_x) a la superfície del nanofils, amb un gruix d'aproximadament 1 nm. Aquesta capa ha estat caracteritzada després d'escalfar els nanofils durant una setmana a 100°C en aire, després del qual l'òxid de germani ha mantingut el gruix. L'obtenció d'un gruix estable de l'òxid de Ge és de rellevant importància, doncs com a material dielèctric pot influir decisivament en la transferència de càrrega entre els gasos i el semiconductor.

Així doncs, els dispositius han estat estudiats com a sensor de gas a una temperatura de 100 °C, observant una resposta envers O_2, CO, NO_2 i H_2O. Els sensors de Ge mostren una clara resposta envers CO diluït en aire, mentre que aquesta és quasi nul·la quan el gas reductor es troba diluït en nitrogen. Per tant, l'intercanvi de càrrega requereix la pre-adsorció d'oxigen a la superfície. Aquest tipus de resposta és consistent amb el model de sensor de gas semiconductor tipus p.

La resposta envers vapor d'aigua, ha estat estudiada a la mateixa temperatura, donant lloc a la mateixa resposta quan aquesta és diluïda en nitrogen o en aire sintètic. Aquest fenomen és atribuït a la fisisorció dels dipols formats per la molècula de vapor d'aigua, que dóna lloc a la resposta més important d'entre les estudiades.

Nanofils individuals de SnO_2 contactats per litografia per feix d'electrons

Una nova metodologia basada en l'ús de litografia per feix d'electrons per a la fabricació de contactes per a nanofils individuals en microplaques calefactores suspeses o micromembranes ha estat desenvolupat.

Els nanofils individuals, donat que tenen una geometria ben definida i coneguda, permeten l'estudi de les interaccions del material amb els gasos adsorbits a través d'una configuració més senzilla. A més a més, si els nanofils son monocristal·lins, permeten la conducció dels electrons sense la presència de barreres intergranulars.

El procés de contactat dels nanofils es divideix en diferents passos, un cop els nanofils ja són dipositats sobre les membranes, resumits en:

i) Recobriment per rotació (*spin-coating*) de la resina PMMA sobre els dispositius.

ii) Exposició via feix d'electrons dels contactes predissenyats sobre les membranes, amb conseqüent revelat de la resina.

iii) Dipòsit de les pel·lícules metàl·liques (Ti/Pt) i posterior *lift-off* de la resina.

El perfil i rugositat superficial de la membrana ha estat estudiat mitjançant microscòpia confocal, mostrant un desnivell de fins a 220 nm, degut a la presència del microcalefactor enterrat a la capa de Si_3N_4 [13]. El perfil de la resina després del *spin-coating* ha estat caracteritzat, observant importants diferències en el gruix causat pel mateix motiu. Així doncs, el procés de fabricació dels nano-contactes ha estat optimitzat i adaptat fins a trobar els paràmetres de fabricació que han permès fabricar sensors de gas basats en nanofils individuals de SnO_2. La fabricació té diferents avantatges si es compara amb la metodologia de feix d'ions focalitzat (*FIB*), la tècnica de referència per

a la fabricació d'aquests dispositius desenvolupada en el departament, en el que es fabriquen contactes de Pt/C altament resistius.

Els sensors han estats caracteritzats elèctricament, mostrant un comportament no òhmic de forma inesperada, doncs les juncions metall/semiconductor com Ti/SnO_2 no donen lloc a una barrera Schottky. El comportament no lineal és atribuït a restes orgàniques presents al nanofil, degut a restes de la resina o de productes emprats del revelat.

Els sensors han estat caracteritzats com a sensor de gas, mostrant un comportament envers amoníac en aire sintètic que és consistent amb el comportament mostrat per xarxes de nanofils de SnO_2 mostrats en el capítol 4 de la present tesi.

Conclusions

Vers els processos de fabricació

1. En aquesta tesi ha estat realitzat per primer cop, el creixement localitzat de xarxes de nanofils de SnO_2 i Ge via un procés de dipòsit via *CVD* a sobre de microdispositius, mitjançant un procés escalable i que va un pas més enllà en la integració de dispositius basats en nanofils. Els nanofils crescuts són monocristal·lins, i són cristal·linament idèntics a les estructures crescudes amb processos estàndards de creixement.
2. La fabricació de sensors de gas basats en nanofils individuals de SnO_2 sobre microplaques calefactores ha estat implementat mitjançant litografia per feix d'electrons. Els substrats litografiats han mostrat important rugositats, que han estat caracteritzades per tal d'adaptar-hi el procés .

3. El procés de fabricació ha demostrat ser exitós per a nanofils amb diàmetre menor de 80 nm. Els contactes fabricats són de baixa resistència, que proporcionen una clara avantatge respecte la metodologia de fabricació per FIB.

Vers els mecanismes de sensat de gas

Xarxes de nanofils de SnO_2

4. La resposta de les xarxes de nanofils SnO_2 respecte la presència de NH_3 han estat estudiats en un rang de temperatures entre 150 i 450 ºC , mostrant la promoció de NO com a producte a temperatures superiors a 450 ºC. Aquest fet redueix la resposta del sensor.
5. En condicions humides, la resposta es veu reduïda, degut a la competició entre les molècules de vapor d'aigua i amoníac pels mateixos llocs d'adsorció. L'energia d'activació de l'oxidació d'amoníac es veu disminuïda en condicions humides, fet atribuït a la reacció de l'oxigen amb els grups hidroxils adsorbits, facilitant la dissociació del primer.

Xarxes de nanofils de Ge

6. Els nanofils de Ge han estat mesurats com a tipus p a través de mesures d'efecte de camp realitzades emprar la microplaca calefactora com a transistor.
7. El mecanisme de sensat de gas dels nanofils de Ge ha estat identificat com el d'un sensor semiconductor (òxid metàl·lic) de tipus p.
8. L'òxid de Ge present a la superfície dels nanofils juga un paper clau en el sensat de gas. Els dispositius s'han mantingut a una temperatura de 100 ºC per tal de mantenir un gruix estable de l'òxid.
9. L'adsorció dels dipols formats per les molècules de vapor d'aigua a l'esmentada temperatura és atribuïda a un procés de fisisorció, en el que l'hidrogen queda

orientat en direcció a la superfície del nanofil. Aquest procés és possible mercè a la presència de grups metils a la superfície del nanofil provinent del procés de creixement.

Nanofils individuals

10. Els nanofils de SnO_2 individuals fabricats per litografia per feix d'electrons, segueixen el mateix comportament que les xarxes de nanofils en el mecanisme de reacció respecte l'amoníac. La promoció d'òxid nítric com a producte és promogut a 400ºC.
11. Els sensors basats en nanofils individuals mostren una resposta més ràpida i superior en valor relatiu que les xarxes de nanofils vers NO_2 i NH_3. El fenomen s'atribueix a la difusió del gas, que es veu facilitada en els sensors de gas individuals.

Referències

[1] World Health Organization, WHO Air quality guidelines for particulate matter, ozone, nitrogen dioxide and sulfur dioxide: global update 2005: summary of risk assessment, Geneva World Health. Organ. (2006) 1–22. http://whqlibdoc.who.int/hq/2006/WHO_SDE_PHE_OEH_06.02_eng.pdf?ua=1.

[2] M.A. Danzon, R. Van Leeuwen, M. Krzyzanowski, Air Quality Guidelines for Europe, World Health Organization, 2nd ed., Copenhagen, 2000.

[3] R. Moos, K. Sahner, M. Fleischer, U. Guth, N. Barsan, U. Weimar, Solid State Gas Sensor Research in Germany – a Status Report, Sensors. 9 (2009) 4323. doi:10.3390/s90604323.

[4] P.T. Moseley, Solid state gas sensors, Meas. Sci. Technol. 8 (1997) 223–237. http://stacks.iop.org/0957-0233/8/i=3/a=003.

[5] N. Yamazoe, Toward innovations of gas sensor technology, Sensors Actuators, B Chem. 108 (2005) 2–14. doi:10.1016/j.snb.2004.12.075.

[6] N. Barsan, U. Weimar, Conduction model of metal oxide gas sensors, J. Electroceramics. 7 (2001) 143–167. doi:10.1023/A:1014405811371.

[7] A. Köck, L. Chitu, S. Defregger, E. Kraker, G. Maier, S. Steinhauer, et al., Metal Oxide Nanowires for Gas Sensor Applications, BHM Berg- Und H{ü}ttenm{ä}nnische Monatshefte. 159 (2014) 385–389. doi:10.1007/s00501-014-0286-5.

[8] S. Barth, F. Hernandez-Ramirez, J.D. Holmes, A. Romano-Rodriguez, Synthesis and applications of one-dimensional semiconductors, Prog. Mater. Sci. 55 (2010) 563–627. doi:10.1016/j.pmatsci.2010.02.001.

[9] E. Comini, G. Sberveglieri, Metal oxide nanowires as chemical sensors, Mater. Today. 13 (2010) 36–44. doi:http://dx.doi.org/10.1016/S1369-7021(10)70126-7.

[10] X. Chen, C.K.Y. Wong, C.A. Yuan, G. Zhang, Nanowire-based gas sensors, Sensors Actuators B Chem. 177 (2013) 178–195. doi:http://dx.doi.org/10.1016/j.snb.2012.10.134.

[11] M. Fleischer, M. Lehmann, Solid state gas sensors - Industrial applications. The power of nanomaterial approaches in gas sensors, Springer-Verlag Berlin Heidelberg, 2012.

[12] W.C. Dunlap, Gold as an Acceptor in Germanium, Phys. Rev. 97 (1955) 614–629. doi:10.1103/PhysRev.97.614.

[13] J. Puigcorbé, D. Vogel, B. Michel, A. Vilà, I. Gràcia, C. Cané, et al., Thermal and mechanical analysis of micromachined gas sensors, J. Micromechanics Microengineering. 13 (2003) 548–556. doi:10.1088/0960-1317/13/5/304.